# Experimental observation of elastic wave demultiplexer in phononic slab waveguides

Mohd Syafiq Faiz Bin Nor Ashikin

**THÈSE DE DOCTORAT**

**DE L'ÉTABLISSEMENT UNIVERSITÉ BOURGOGNE FRANCHE-COMTÉ**

**PRÉPARÉE À L'UNIVERSITÉ DE FRANCHE-COMTÉ**

École doctorale n°37

Sciences Pour l'Ingénieur et Microtechniques

Doctorat de sciences pour l'ingenieur

par

MOHD SYAFIQ FAIZ B. NOR ASHIKIN

# Experimental observation of elastic wave demultiplexer in phononic slab waveguides

## Observation expérimentale d'un démultiplexeur à ondes élastiques dans des guides phononiques

Thèse présentée et soutenue à Besançon, le 17 December 2020

Composition du Jury :

| | | |
|---|---|---|
| ABDUL HALIM SHAARI | Rapporteur | Professeur des Universités, Universiti Putra Malaisie |
| MOHD HANIF YAACOB | Rapporteur | Professeur des Universités, Universiti Putra Malaisie |
| ABANG ANNUAR EHSAN | Examinateur | Chargé de Recherché, IMEN, UKM, Malaisie |
| SIOW KIM SHYONG | Examinateur | Maitre de conférence, IMEN, UKM, Malaisie |
| MAHMOUD ADDOUCHE | Coéncadrant | Maitre de conférence,Université de Franche-Comté |
| AHMAD RIFQI MD ZAIN | Codirecteur | Professeur des Universités, IMEN, UKM, Malaisie |
| ABDELKRIM KHELIF | Directeur | Directeur de Recherche, CNRS, Institut FEMTO-ST France |

N° | 0 | 5 | D | U | 7 | R | 0 | 1 | U | 7 | 5 |

# ACKNOWLEDGEMENTS

Finally, the long-awaited stage which signifies the end of the journey of my doctoral thesis. I would like to thank those who have helped me during the four years of my professional experience as a young researcher in both institutes, FEMTO-ST from Université de Franche-Comté, Besançon France and Institute of Microengineering and Nanoelectronics (IMEN), from National University of Malaysia (UKM) to complete this thesis. This thesis is the result of collective teamwork, particularly from FEMTO-ST, where I spent most of my research years in the institute.

I would like to express my gratitude to the people who have contributed directly or indirectly to this work, through their scientific and human contributions. Firstly, I would like to express my gratitude to God for my life and for all the blessings I've received so far (Alhamdulillah). Secondly, I want to thank Prof. Abdelkrim Khelif for agreeing to supervise this research work under unusual conditions. I am very grateful for the trust he has placed in me to finish this thesis. I am also thankful for his immense scientific knowledge and skills, which makes him a supervisor whom anyone would hope to have. Thirdly, I want to thank Dr. Mahmoud Addouche, who is much more than a thesis co-supervisor for me. During this period, he was the reference of my work and I owe him a lot, especially for his invaluable help in setting up digital tools and solving problems relating to the programming languages that I had to learn. His insight, by putting me back on the right path whenever I was bewildered with my work, and his guidance will be etched and remembered in my mind for a very long time.

I also want to address my gratitude to all the members of my family who supported me during the various stages of my studies, particularly to my father in-law, Prof. Abdelkader Hassein-Bey. In addition, a special thanks to my wife, Asmaa Leila Sabeha Hassein-Bey, who will soon earn her Doctor of Philosophy. I was particularly touched by the trust she placed in me. Regardless of all the unfortunate situations which surrounded her, she consistently offered her mind, energy and time to help me to complete my thesis. Thanks to my little family in Malaysia who supported me indirectly throughout the thesis. All the members of my family were deeply touched by the accomplishment of this work for they are my witnesses to all the challenges that the journey inevitably brought during my doctoral work.

I will also not forget to thank Franck Lardet, the engineer who did a remarkable job of helping me; his permanent presence and enriching advice enabled me to complete my

experimental work. During this period we spent 10 months along with my co-supervisor to figure out the best measurement setup for my device. I would like to thank Mr. Florent Deux, the Head Department of Optical Measurement System at Polytec France, who consistently responded to my emails to set up the experimental work in Polytec Paris.

I also want to thank all the members of our department team in FEMTO-ST, particularly Dr. Sarah Bechabane for her critical opinion about my work to improve the outcomes. Thanks as well to IMEN director Prof. Azrul Azlan Hamzah and co-director Dr. Mohd Ambri Mohamed for their help and encouragement.

To my close friends, Aymen Jalouli, Farhanulhakim Razip Wee, Amar Chalagne, Ali Yassin Elayouch, and Youssef Tedja, thank you very much for being my sounding board in hearing all of my research-related problems.

Thanks to my supervisors in Malaysia, particularly my thesis director, Dr. Rifqi Md. Zain for supporting me to pursue my research. Thanks also to my co-supervisor, Dr. Kim Siow Shyong, for constantlyupdating me on my research progress. I thank him for his availability, and his swift responsiveness to my questions and requests. His insight and encouragement during my research period are particularly appreciated.

Finally, I would like to thank the director of the FEMTO-ST Institute, Laurent Larger, and the director of the MN2S department, Wilfrid Boireau, for welcoming me to this research entity. Likewise, I would like to express my thanks to the director of the ED SPIM doctoral school, Therése Leblois, as well as to Alika Rossetti who constantly ensured the smooth running of the thesis. I also warmly thank Sandrine Pyon, Ayoko Afanou, and Joelle Berthelot, who have always responded positively and with sympathy to my administrative and logistical requests. To my thesis examiners, Prof. Dr Abdul Halim Shaari and Prof. Hanif Halim, thank you for the valuable time in examining my thesis.

I will end this part by thanking the French embassy, particularly Dr. Maxime Ferraile and Dr. Philippe Arnaud, for the special French government scholarship program, which allowed me to further my PhD in France. Thank you for your presence, your support and your kind attentions which I will never forget. This thesis would never have been successful without the involvement of each of these people named. Thank you.

# CONTENTS

# 1

# INTRODUCTION

Inside the natural crystal, atoms randomly moving around their equilibrium position and occupying a very precise position. This gives rise to a perfect order and high level of symmetry in the crystal structure. Scientists have long assumed that it is impossible to control this random motion, which led to the invention of man-made (or artificial) periodic structures where such control is possible. The word 'artificial' is used to differentiate this novel material from the natural crystal. By means of artificial, the periodicity of the crystal has a lattice constant, $a$ which is much larger than inter-atomic distances in natural crystals. The term artificial also means that the periodic system of the material was made by using a technology or hand crafting [1]. The term periodic structure may refer to several definitions either periodic in a sense of material constituents, boundary conditions or the geometry.

In the late 1980, the emerging study known as photonic crystal, PtC was proposed to influence the propagation of electromagnetic waves in the same way crystalline atomic lattice in semiconductor technology controls the electric currents. However, the PtC study was later inspired a new field study to control the propagation of acoustic or elastic waves. This new field study, which is generally known as phononic crystal, PnC (sometimes known as sonic crystal) is an artificial periodic structure that can change the propagation of acoustic or elastic waves. The term PnC and sonic crystal are used interchangeably but for clarity, the term phononic crystal (PnC) will be used throughout this dissertation instead of sonic crystal.

One of the importants application for PnC (which is the focused topic of this dissertation) is the waveguiding or wave confinement/localization by using defect engineering [2–5]. In 1998, Sigalas et al., [3] showed the first setup for a linear waveguide by introducing a defect in a perfect crystal. Other studies have subsequently exploited the elastic waves confinement with a point, linear or angled defect [6–10]. The objective of this thesis is to demonstrate a compact PnC-demultiplexing based structure consisting of multiple waveguides channels for frequency filtering purposes. Thus, the introduction provides a general background of the research objectives, the motivations, applications and a

background literature of the subject. The introduction will highlight some overviews on other research approaches to achieve the same objectives in order to appreciate the novelty proposed in the dissertation.

## 1.1/ PROBLEM STATEMENT

From the lists of the earliest existing studies since the PnC demultiplexing was introduced by Khelif et al., (2003), many approaches have been used by many researchers. To date, most of the proposed PnC-based structures have been achieved via the liquid-liquid structures or solid inclusions inside the liquid substrate. The studies vary from modifying the liquid constituent of hollow-cylinder defects such as mercury or by introducing the temperature variation to the liquid to change its acoustic properties. The downside of such methods is the challenge to selectively choose the suitable liquid content to meet a certain filtering frequency. Consequently, this can force some application to select a liquid source from unwanted hazardous materials. Thus, the choice of materials which are environmentally friendly and pose no health-risk issues is fairly small for this reason. Secondly, in principle, the temperature can influence the resonance frequency in PnCs. Accordingly, in a 1D Phononic crystal, Nagaty et al., (2018) [11] investigated the effect of temperature on the resonance point. The findings showed that the resonance rate can be changed by the temperature rising and decreasing. However, a major drawback based on temperature tuning or material constituent lies within their inherent limitivity, which is typically fixed for a given design and given temperature/material constituent. Similarly, most researchers have limited findings in the narrow pass-band. Even though, in terms of selectivity, the narrow pass-band demonstrates better frequency target at the desired frequency, this can indirectly limit its filtering capability as well. In this case, a wide range filtering frequency is more advantageous compared to narrow selectivity. A freedom of frequency selection can be easily available in wide frequency ranges. Furthermore, in terms of wave confinement and filtering, a waveguide that exhibits wide range frequency transmission does not show any lesser selectivity capability compared to a narrow pass-band transmission. Thus, it is the current thesis of interest to focus on the theoretical and experimental aspect for a PnC demultiplexing application with a wide frequency filtering capability.

## 1.2/ RESEARCH OBJECTIVES

The thesis proposes that a pillar-based phononic crystal slab consists of multiples waveguides channels for wide-spectrum frequencies demultiplexing application.

- The first step is to theoretically demonstrate the existence of several pass-bands within the complete band gap to produce multiple-frequency filtering for demultiplexing application in kHz frequency ranges.
- The second step is to fabricate the demultiplexer model using 3D metal machine based on Direct Metal Laser Sintering (DMLS) technology.
- The third steps are to (a) measure of transmission coefficient for wave propagation within the multiple channels of waveguides systems (b) displacement measurement to demonstrate transmission and blocking of the demultiplexing system.

## 1.3/ THESIS ORGANIZATION

In the second chapter, a brief history on the origin of the phononic crystal, which is derived from photonic research, is explained. A subtle theory on the phononic crystal lattice, the concept of the brillouin zone, and the fundamental equations on the propagation of elastic waves are also given. The summary of the state of the art of phononic crystal waveguides and demultiplexing researches as well as the method of simulations, fabrications and measurement are also included.

In the third chapter, simulation processes for the band gap structure, waveguiding passing band, their respective transmission coefficients, and displacement propagation behavior were calculated by using Finite Element Method (FEM). The objective of this chapter is to theoretically demonstrate the frequency filtering transmission that is capable of transmitting continuous and wide frequency ranges for a better demultiplexing function as stated in the problem statement.

In the fourth chapter, the fabrication and measurement study to verify the simulation study are reported. Two approaches were considered to understand the behavior of the demultiplexing device for a. measurement of filtering transmission and b. cartography measurement.

Finally, in the conclusion, a summary of the research findings and future perspectives for future works are mentioned.

# 2

# LITERATURE REVIEW

## 2.1/ INTRODUCTION

In the early 1990s, research was focused on demonstrating the properties of acoustic waves propagation inside a periodic phononic structure. The interesting physics behind the wave motion in such composite materials has attracted researchers for its important phenomenon known as ”forbidden bands”. This chapter describes the emerging phononic crystal, PnC and their fundamental concepts, such as the creation of band gaps. A comprehensive review about the current development of acoustic or elastic waveguiding and demultiplexing are also discussed. In the penultimate part of the chapter, the state of art for simulation and measurement methods have been highlighted.

## 2.2/ HISTORY AND CONCEPT OF PHONONIC AND PHOTONIC CRYSTALS

Historically, the use of periodic structures to control the wave propagation can be traced back to the 19th century with the work of Lord Rayleigh in 1887 [12]. He highlighted the existence of stopping bands for electromagnetic waves in a unidirectional periodic dielectric medium. Indeed, in 1887 Lord Rayleigh founded the first theoretical work on 1D photonic crystal, PtC: a multi-layered film of different refractive indices alternating from one layer to another to influence the behavior of electromagnetic waves [13]. This structure is also known as a one-dimensional PtC due to its alternation of two distinct dielectric media in a single direction of space [14]. Developed by William Lawrence Bragg, the Bragg mirror in Fig. 2.1 is a perfect example of this one-dimensional phenomenon. Since then, the physics of wave propagation in a periodic medium has been studied in all fields, such as phonons in a crystal, electromagnetic waves in solid or quantum waves in semiconductors. Rayleigh has shown that even the simplest one-dimensional PtC can have surprising properties to hinder the propagation of certain electromagnetic waves.

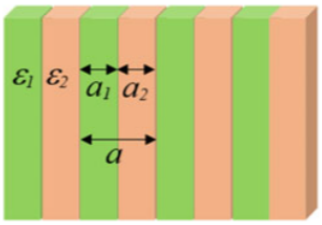


Figure 2.1: Bragg mirror with thicknesses $a_1$ and $a_2$ of different permittivities $\varepsilon_1$ and $\varepsilon_2$ [15]

The concept of the Photonic Band Gap (PtBg) started to gain attention in the late 1980s. It was discovered simultaneously by Eli Yablonovitch's teams [16] of Bell Laboratories in New Jersey (United States) and by John Sajeev [17] of Princeton University in 1987. Their work suggested the possibility to obtain one system prohibiting the propagation of electromagnetic waves in a certain frequency range, regardless of the direction of the incident wave. Due to his 1987 reports, Eli Yablonovitch was popularly referred to as the founder of PtC.

The photonic study later inspired a new field study known as PnC, which controls the propagation of acoustic or elastic waves. The year 1988 saw the work of Tamura et al., [18] which theoretically showed the total reflection of the acoustic wave by a 1D network designed with a succession of two materials. In 1993, Kushwaha et al., [19], Economou and Sigalas [20] provided the theoretical ground work on the elastic waves propagation in two- or three-dimensional, which incited the growing interest for PnC. Since then, many theoretical works on PnC have progressed over the past two decades, dealing with novel systems by using a multitude of numerical simulation methods.

Throughout history, both photonics and phononics have adopted the same theoretical approach as electronic studies in solid-state-physics, such as Finite-difference-time-domain method (FDTD). Since the origin of their theoretical development is rooted from the same physics background, both research areas share many similar researches objectives, computation methods, fundamental concepts, as well as applications. For instance, the objectives for both photonics and phononics research have been focused on seeking the band energy for optical (or acoustic band gap) which displays the optical (or acoustic) energy versus the wave vectors. Other examples are the introduction of defects inside the perfect PtC or PnC (either linear or point defects) for energy confinement. By using this method (basically analogous to electronic dopant), the energy can be guided and confined in a sharp corner.

## 2.3/ DEFINITION OF A PHONONIC CRYSTAL

Phononic crystals, PnC are the periodic structures which consist of composite materials with different elastic properties. These non-homogeneous elastic materials are able to manipulate the flow of sound in air, the acoustic waves in fluids or the elastic waves in solids. Fig. 2.2 shows some examples of one-dimensional (1D), two-dimensional (2D) and three-dimensional (3D) PnC systems which have been the focus of most studies over the last 20 years.

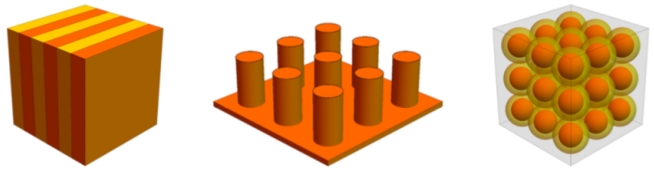

(a) 1D (b) 2D (c) 3D

Figure 2.2: Phononic materials with periodicity in multiple dimensions (a) one-dimensional (1D) (b) two dimensional (2D) (c) three dimensional (3D) [21]

Historically, the year 1988 saw the works of Tamura et al., [18] who were the first to have studied the propagation of phonons in a one-dimensionally structure. Among the three systems as illustrated in Fig. 2.2, the two-dimensional (2D) structure is the mostly extensive arrangements to be studied. In 1993, Sigalas, Economou, Kushwaha [19, 20], were the first to study a 2D PnC structures which are periodic in $X$ and $Y$ directions with an infinitely long inclusion in the $Z$ direction. M.S. Kushwaha et al., used a 2D arrangement of nickel cylinders incorporated in an aluminum matrix. Meanwhile, Economou and Sigalas studied the propagation of elastic waves in structures made up of gold, Au cylinders embedded in a Beryllium, Be host to exhibiting the narrow pass band [22]. Since then, many studies have dealt with the same type of PnC composing of different environments and cornering, for example, solid inclusions in a solid matrix or solid inclusions in a fluid matrix.

### 2.3.1/ MECHANISM OF PHONONIC BAND GAP

The most significant feature that periodic phononic crystal structures reveal is band gaps. They are regarded as the most fundamental PnC property that makes other potential properties, such as the mechanism of local resonance. Historically, the band gap in crystal structures have been rigorously studied in many different types of waves, such as electrons in semiconductor, or electromagnetic waves in PtC. In solid state physics, the band diagram represents a fundamental basis for the classification of materials into metals, semi-conductors and insulators. Many different aspects of crystals, such as why solids behave as metal, insulator and semiconductor, are explicable through the picture of

band theory. In PnC, the interaction between the periodic structures with acoustic waves have been known to create a band gap (BnG) that prohibits the propagation of certain acoustic or elastic waves.

Croënne et al [23] have studied the processes surrounding the creation of band gaps in PnCs (2011). Three distinct mechanisms for phononic band gaps have been established according to their research, namely Bragg, hybridization, and weak effect elastic coupling. Among these three factors, Bragg interference is the most apparent explanation that can lead to band gaps and it is also traditionally, the first physical process to invoke the band gap phenomena.

Bragg gaps are prevalent characteristics caused by the destructive interference of waves dispersed from the inclusions. Depending on the frequency of the waves, the property of periodicity in PnCs contributes to constructive or destructive interference that result in Bragg reflections of acoustic or elastic waves. Waves are strongly distributed and scattered within PnCs and secondary waves are created between them at each interface. The secondary waves are reflected backwards and constructively/destructively interfere with each other. This creates frequency ranges where the waves are either allowed to propagate (pass bands) or blocked in one direction (stop bands) or blocked in any direction (complete band gaps). The band gaps of PnCs are therefore closely related to the geometry of the waves and their frequency. Consequently, in the field of PnCs, band gap architecture is of important interest. The topological shape of a phononic crystal's periodic lattice provides a very useful means for regulating and manipulating acoustic and elastic waves as a consequence of band gaps. Thus, the Bragg band gap occurs when the wavelength of incoming waves is equal to the periodicity of the crystal lattice size.

On the other hand, the local resonance band gap is primarily influenced by the inclusions' resonating properties. The band gap central frequency and size are determined by many factors, such as density, elastic constant, the geometry, periodicity and the size of the periodicity of lattice. The property of the band diagram that indicates the relationship between energy with wave number, $k$ along many directions, can demonstrate the dispersion relation that describes the behavior of wave propagation in an elastic medium and the existence of the band gap. Figure 2.3 shows an example of the dispersion curves of a phononic crystal with resonators [24] to identify the position of the forbidden bands (frequency ranges where any propagation is prohibited). In Figure 2.3, notice the band gap region where no wave energy is allowed to travel within 114 to 143 kHz.

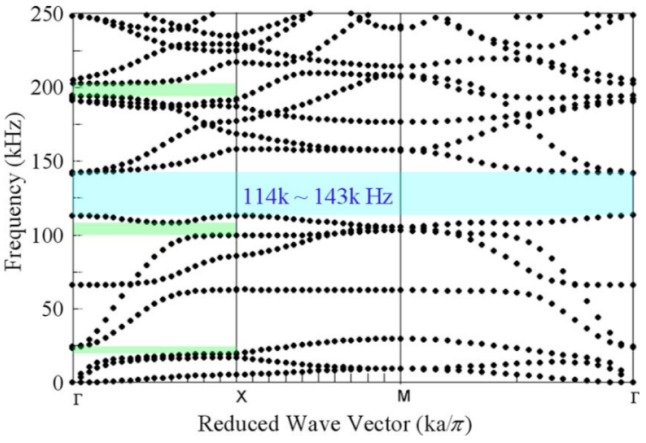


Figure 2.3: Dispersion curves representing the propagation of elastic waves in a periodic unit cell structure with resonance inclusion. The shaded area illustrates the band gap where no mode is allowed to propagate [24]

## 2.4/ WAVE PROPAGATION IN A PERIODIC STRUCTURE

### 2.4.1/ CRYSTALLOGRAPHY

The Brillouin zone is defined by the periodicity of PnC that in turn determine the wave vector, $k$ needed to plot the dispersion curve. The region of the band gap occurs at symmetry points of reciprocal space and also along the direction of the Brillouin zone. Figure 2.4 shows the irreducible Brillouin zone for the square lattice considered in the current thesis. The wave vectors $k$, will be plotted along the paths determined by the points $\Gamma$ - 'X'- M' - $\Gamma$ for the dispersion curve.

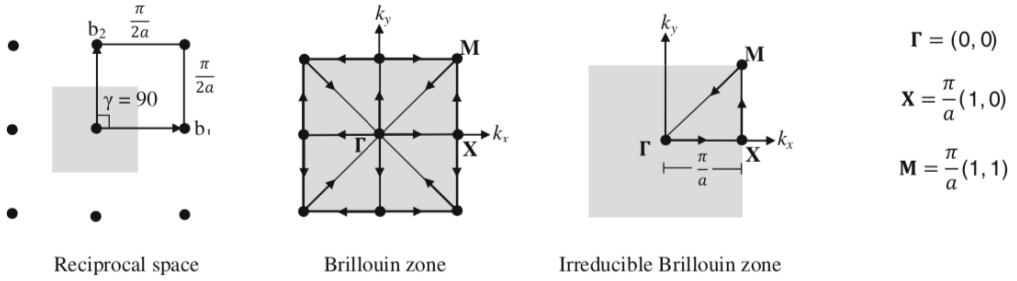


Figure 2.4: The irreducible Brillouin zones for square lattice unit cells in reciprocal space [25]

In 1883, Floquet first proposed the analysis of wave propagation in periodic media in one dimension. Bloch applied Floquet's work to three dimensions known as the Bloch theorem, which fits the propagation of mechanical waves in current PnCs research. In 1D PnCs, elastic waves can propagate independently as longitudinal Bloch waves or as transverse Bloch waves as the displacement vector components $u_x$, $u_y$, and $u_z$ are

independent. For 2D PnCs, elastic waves travel as in-plane elastic Bloch waves and out-of-plane elastic Bloch waves (transverse waves) due to the coupled-displacement axis regulating the displacement wave vector in one periodicity direction and another wave vector for the second periodicity direction. While in 3D PnCs, elastic waves are neither transverse nor longitudinal since the components of the displacement vector $u_x$, $u_y$, and $u_z$ are usually coupled to each other.

### 2.4.2/ DISPERSION CURVE DERIVATION

The following derivation for dispersion relation and the Brillouin zone is based on the Kittel (1953) book, "Introduction to Solid State Physics". Consider an elastic vibration occurring in a primitive cell with one atom. When the wave propagates in [1 0 0] direction, atoms will vibrate in phase to the direction of the wave vector. This includes for both parallel or perpendicular directions of the wave vector. Let us denote the displacement from an equilibrium position of plane x as $u_x$. For conciseness, only the interaction of the closest neighbor, s ± 1 is considered. The total force is given by :

$$F_s = C(u_{s+1} - u_s) + C(u_{s-1} - u_s) \tag{2.1}$$

where $c$ is the force constant between closest planes and for brevity, $c$ can be regarded as one atom of the plane. Thus, a force for one atom in plane $s$ :

$$\frac{d^2u}{dt^2} = C(u_{s+1} - u_{s-1} - 2u_s) \tag{2.2}$$

From 2.2, then

$$-M\omega^2 u_s = C(u_{s+1} - u_{s-1} - 2u_s) \tag{2.3}$$

where $M$ is a mass of an atom. The displacement $u$, has a solution as :

$$u_{s+1} = uexp[iska]i\omega exp[\pm ika] \tag{2.4}$$

where $u_s = u$ exp$[iska]$ and $u_{s+1} = u$ exp $i[s+1]ka$, thus $u_{s+1} = u$ exp $[iska]i\omega exp[\pm ika]$. where $a$ is the space between planes and $k$ is a wave vector. From (2.4) substitute into (2.3). With identity $2cos(ka)$=exp$(ika)$+exp$(-ika)$ then the dispersion relation $\omega$ k is given by

$$\omega^2 = \frac{2c}{m}[1 - cos(ka)] \tag{2.5}$$

by a trigonometric identity, 1-cos(x)=2$sin^2(x/2)$ then

$$\omega = \frac{4c}{M}^{\frac{1}{2}} [sin(\frac{ka}{2})] \tag{2.6}$$

the boundary for the first Brillouin zone is given by $k = \pm \pi$ a, and from (2.6), the graph of $\omega$ versus $k$ is given by Fig. 2.5:

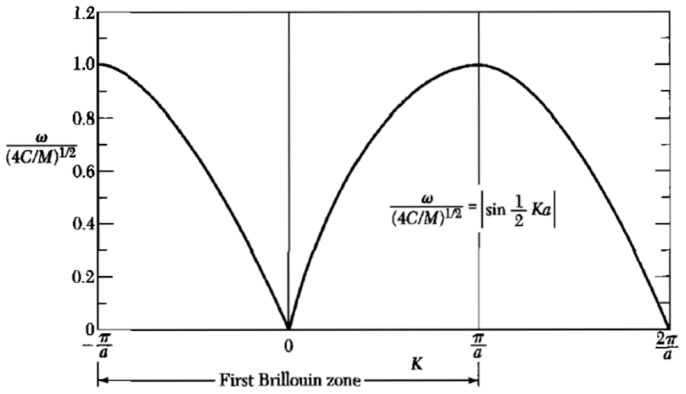


Figure 2.5: Plot of $\omega$ versus $k$, where the first Brillouin zone, $k$ is the only zone that physically significant for elastic waves [26]

From 2.4, the ratio of displacement for 2 planes $u_{s+1}$ and $u_s$ is given by:

$$\frac{u_{s+1}}{u_s} = \frac{uexp[i(s+1)ka]}{uexp[iska]} exp(ika) \tag{2.7}$$

where -$\pi$ <ka> $\pi$ or -$\pi/a$<ka>$\pi$/a and this is the first Brillouin zone for the linear lattice with its maximum value of is $k_{max} = \pm \pi/a$. The first Brillouin zone at limit ($\pm \pi$)/$a$ is enough to describe a lattice motion outside this limit. The value beyond -$\pi$/a <ka> $\pi$/a can be treated by subtracting the multiple of 2$\pi$/ that will give a wave vector within the limit of 2$\pi$a. For instance, given a $k$ is beyond the first zone and $k$' lies within the first zone, then $k$' is defined as $k$'=$k$-2$\pi$ $n/a$ and $k$=$k$' + 2$\pi$ $n/a$. From 2.7

$$\frac{u_{s+1}}{u_s} = exp[i(ka - 2\pi n)] exp(i2\pi n) \tag{2.8}$$

Since from Euler formula exp($i$2$\pi$n)=1, then

$$exp(ika) = exp[i(ka - 2\pi n)] \equiv exp(ik'a) \tag{2.9}$$

from (2.9) the lattice motion can be described by a wave vector of the first Brillouin zone. Noted that 2$\pi n/a$ is a reciprocal lattice vector and by subtracting the reciprocal lattice vector from $k$, a wave vector is equivalent to the first zone.

## 2.5/ POTENTIAL APPLICATIONS OF PHONONIC CRYSTALS

The control and manipulation of acoustic or elastic waves is a fundamental problem with many potential applications. The fields are varied from the field of information and communication technologies to seismic waves. Phononic crystals are used to achieve these goals and were proposed to achieve others. This section provides a brief overview of phononic crystal waveguides which is the ultimate principle behind the demultiplexing application. The section provides the studies about the PnC waveguides in different substrates, i.e., semi-infinite and finite medium. Both the theoretical and experimental aspects are discussed with specific reference to previous research studies.

### 2.5.1/ THEORETICAL AND EXPERIMENTAL OBSERVATION ON WAVEGUIDING EFFECT BASED ON SEMI-INFINITE SUBSTRATE

Addouche et al., [27] theoretically studied the waveguiding effect on a semi-infinite medium. The system consisted of a 2D system of a pillar-based phononic crystal with the ability to confine the wave when the locally resonant defect was introduced. It was observed that, the position of the guided mode within the band gap region was adjustable according to the height of the locally resonant defect. Fig. 2.6(a) represents the band gap of wave propagation in a perfect crystal structure along the $\Gamma$X direction. When the defect was introduced by increasing the height of locally resonant in one row, two guided modes appeared in the band gap region as depicted by $M_1$ and $M_2$ in Fig. 2.6(b). The red dotted line, as appeared in Fig. 2.6(b) is the band diagram for the perfect crystal while the blue dotted line represents the band diagram for the guided modes. At the same time, by increasing the defect height to 0.70x$a$, Addouche et al., [27] reported that it was possible to guide the wave outside the localised modes inside the band gap region. This later produced two guided waves marked with $M_3$ and $M_4$ as depicted in Fig. 2.6(c) and can interact with surface waves. To illustrate the facts, Fig. 2.6(c) shows the displacement field for the guided modes which represents the $M_3$ and $M_4$. It can be clearly observed that the wave can be confined within the defect rows.

Taleb et al., [28] demonstrated the guiding effect based on a hollow cylinder to promote a narrow pass band within the band gap. The phenomena can be attributed to the allowed number of resonance frequency that has been reduced in the hollow cylinder due to the reduction of its radius, hence its spatial confinement. With the help of acoustoelectric interaction of a piezoelectric material, the elastic properties of the PZT can be modulated by changing its conductivity via UV illumination, which subsequently affects the guiding modes of the waveguide. Other reports studied a reconfigurable SAW device by other means, such as magnetic manipulation by using multiferroic substrate and magnetically controlled nonreciprocal SAWs by magnetoelastic and interfacial Dzyaloshinskii-Moriya

interactions. Due to its intrinsic properties, such as a high piezoelectric coefficient, low cost deposition on a non-PZT such as silicon, Si and possible integration with electronic circuits, the ZnO material was considered by Taleb et al. Fig. 2.7 (a)-(b) illustrates the band diagram for a linear defect for radius $r_d$ = 85 nm compared to a perfect cell which consists of radius, $r$ = 65 nm and their displacement field at $f_{d2}$ and $f_{d1}$. As expected, with the presence of a defect structure in the perfect crystal, a wave confinement can be localised inside the defect structure. However, it was shown that with the increase of the waveguide radius it inevitably causes more dispersive waveguide bands.

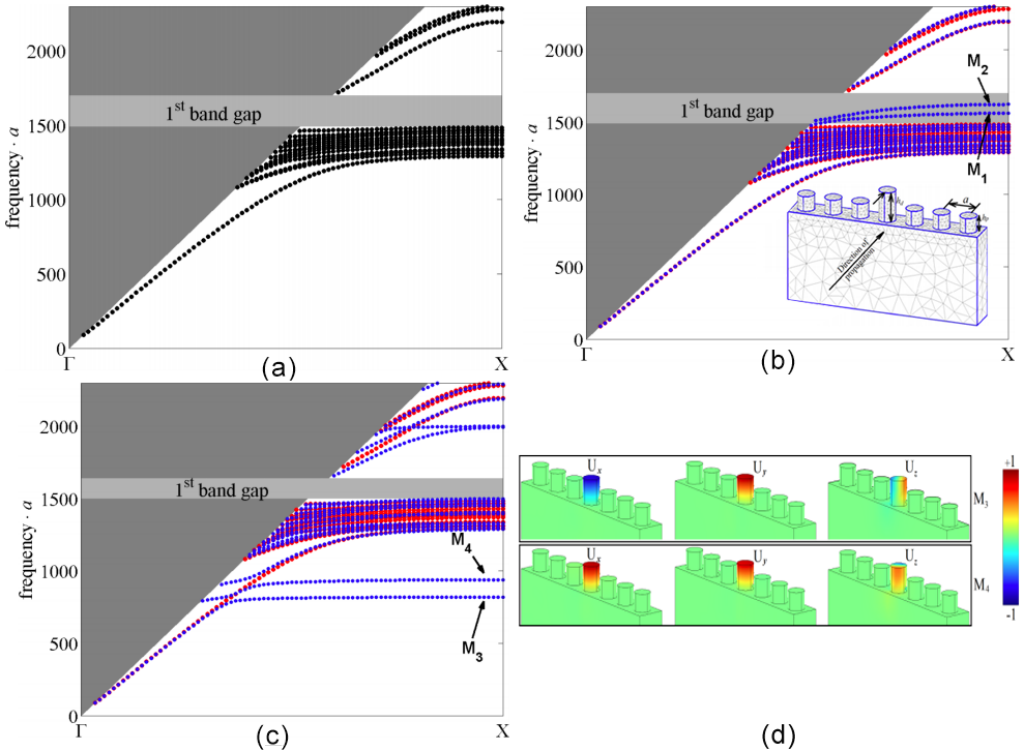


Figure 2.6: (a) Band diagram of a perfect crystal along the ΓX directions (b) band diagram of defect row with a locally resonant equivalent to 0.45x$a$ along the ΓX directions. The inlet shows the supercell model with the locally-resonant modes in the middle of a perfect crystal (c)the guided modes $M_3$ and $M_4$ that exist beyond the band gap region (d)and the displacement field $U_x$, $U_y$ and $U_z$ for the guided modes $M_3$ and $M_4$ in (c)[27]

In order to obtain a defect mode inside the band gap, a hollow cylinder defect waveguide as Fig. 2.7 (c) should be considered. As noted from Fig. 2.7 (d), with the introduction of a hollow pillar, the defect mode has better confinement and shows flat-band phenomena. It is a simple approach without additional complications or fabrication steps to the proposed system.

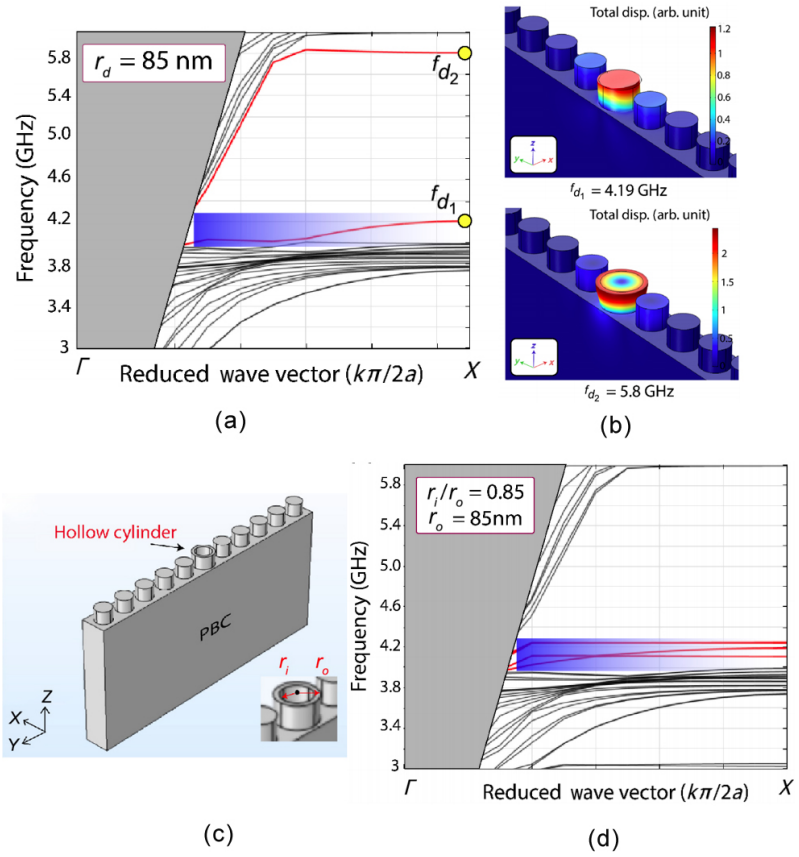


Figure 2.7: (a) Band diagram of linear defect along the ΓX directions for $r_d$ = 85 nm (perfect crystal has radius, r = 65 nm) (b) displacement field at $f_{d2}$ and $f_{d1}$ (c) linear hollow cylinder defect with $r_i$ as the inner radius and $r_o$ as the outer radius, and (d) band diagram for hollow cylinder $r_i/r_o$=0.85 [28]

### 2.5.2/ THEORETICAL OBSERVATION ON WAVEGUIDING EFFECT BASED ON FINITE SUBSTRATE

The behaviors of band gap and waveguide for the finite plate were studied by Wang et al., [29] and consists of a 2D square structure or ”unique”, ”X”, ”+”, ”T” and ”I” structures on top of the plate (refer Fig. 2.8). The stub and plate were made by rubber ($E_A$ = 1.1175 MPa; the Poisson's ratio, $\nu_A$ = 0.47;the density, $\rho_A$ = 1300 kg/$m^3$) and tungsten (the elastic modulus, $E_B$ = 360 GPa; the Poisson's ratio, $\nu_B$ = 0.27; and the density, $\rho_B$ = 17800 kg/$m^3$) respectively. Fig. 2.8 illustrates the band gap's evolution based on the different configuration used for the stub geometry. For the ”unique” stub in Fig. 2.8(a) two observable band gaps can be noted, followed by ”X”, ”+”, ”T” and ”I” structures with 5, 3, 4 and 4 band gaps respectively in Fig. 2.8 (b), (c), (d),(e). Noticeably, the number of band gap increases and the position of the band gap varies with multiple ”unique” stubs at a different geometry. Therefore, the evolution of band gap is sensitive according to the stub structure. The perfect ”X” stub was then considered and ”+”, ”T” and ”I” line defects were introduced. For the sake of clarity, only two (+ and T ) out of 3 (”+”, ”T” and ”I”) defects are

stated in the original reports. Fig. 2.8(f) and (g) illustrate the results. The band gaps can be observed to be unchanged and the localised transmission can be tuned according to the defect shape lines.

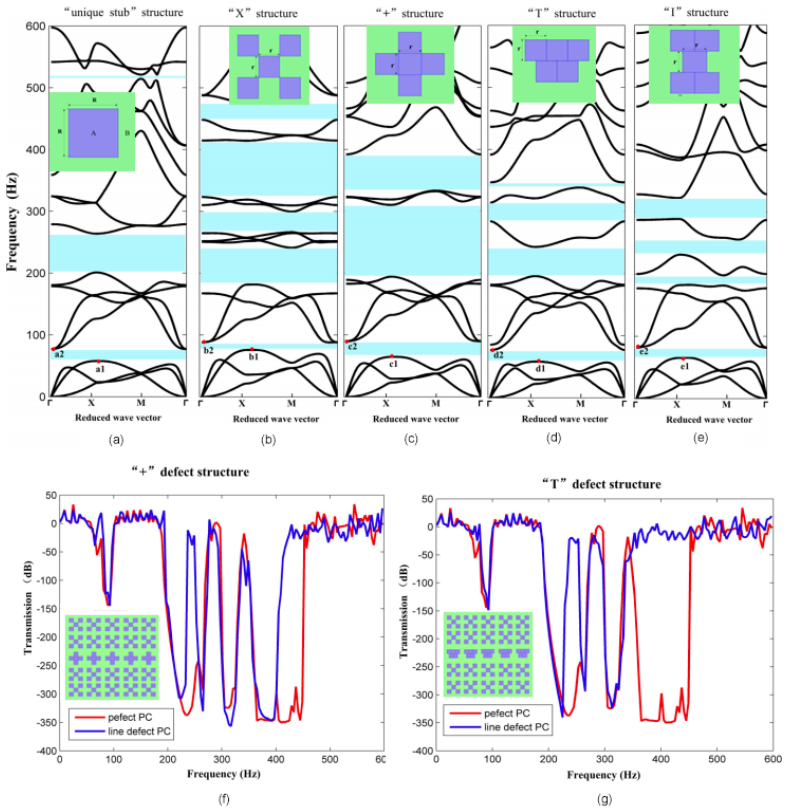


Figure 2.8: (a)Square structure, (b) multi square to form "X" layout, (c) multi square for "+." layout, (d) multi square for 'T', (e) multi square for 'I' with their respective band gaps, (f)perfect 'X' crystal with '+' defect and (g) perfect 'X' crystal with 'T' defect and their respective transmission coefficient [29]

### 2.5.3/ EXPERIMENTAL OBSERVATION ON WAVEGUIDING EFFECT BASED ON FINITE SUBSTRATE

Based on the 2D SiC-air PnC fabricated with snowflake-shaped inclusions using a hexagonal lattice, Ghasemi et al., [30] were able to block and guide an acoustic waves in the frequency range between 665 — 693 Mhz with approximately —4.1% gap-to-mid-gap ratio (refer Fig 2.9). The periodic structure was made by etching the snowflake-shaped inclusions into the SiC plate. According to Ghasemi et al., [30], the choice of snowflake-shaped inclusion was due to the additional parameters it has, such as the radius and width of its inclusions that can boost the width of the band gap. Plus, as compared to other configurations, a snowflake-shaped inclusion is capable to achieve a Giga Hertz range of frequency gap [31]. A defect was then introduced to produce the waveguiding

frequency at 680 MHz and compared with simulation analysis. The waveguiding was observed to transmit 39 % of the energy with 8.2 dB loss, due to the insertion loss factor. If the factor of insertion was eliminated, the transmission ability can be increased with 63 % success, with energy loss as low as 0.17dB/period.

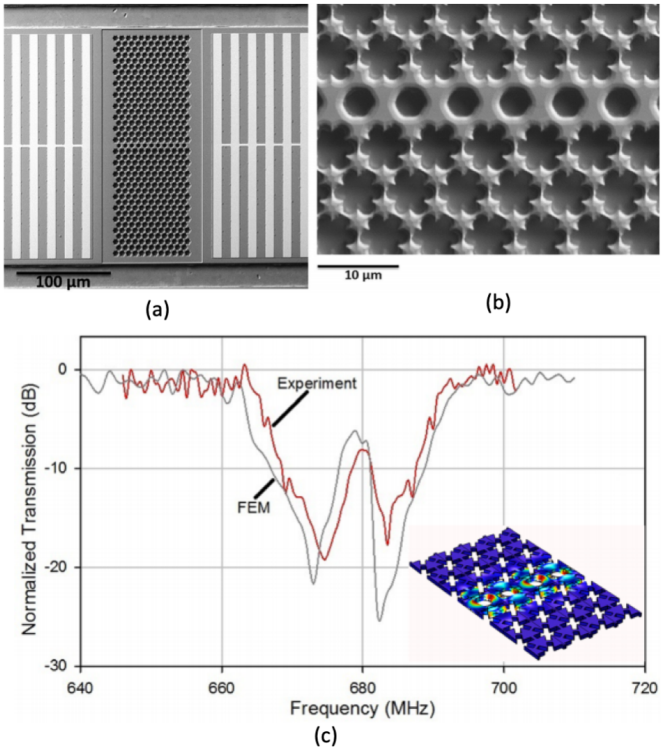


Figure 2.9: (a) SEM for micro waveguides consists of IDT made from aluminium, Al separated by 2D SiC-air PnC fabricated with snowflake-shaped inclusions on a hexagonal lattice, (b) SEM view from the top, (c) comparison between the experimental and simulated transmission of the waveguide. The sub diagram also indicates the simulated displacement field for wave trapping in the waveguide at frequency 679 MHz [30]

Pourabolghasem et al., [32] designed a PnC based on the triangular-lattice that consists of Nickel, Ni inclusion on a trilayer substrate made of AlN, Mo, and Si. The structure supports the BnG at GHz range frequency at around 1100 MHz. The defect introduced into the structure can produce a mono-filtering frequency at 1050 MHz. The frequency, however, can be shifted according to the width defect and three parameter defects were chosen, as illustrated in Fig. 2.10. It was noted that the guide width with $w = 0.8 \times a\sqrt{3}$ demonstrates a mono-mode guide. On the experimental side, the focused IDT was considered to characterise the waveguide at f=1067 MHz, as illustrated in Fig. 2.10(b) and (d). By measuring $S_{21}$ based on a HP 8753D network analyzer in the 1000–1150 MHz frequency range, the device registered a frequency shift of about 2.5% with 1040–1060 MHz.

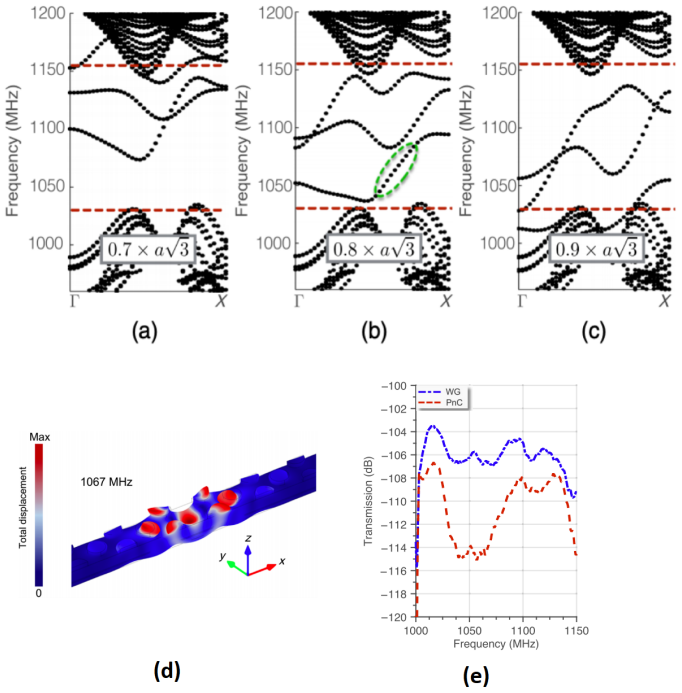


Figure 2.10: Three waveguides' widths with their respective dispersion diagrams (a) $0.7 \times a\sqrt{3}$, (b) $0.8 \times a\sqrt{3}$, (c) $0.9 \times a\sqrt{3}$, (d) simulated displacement for $w = 0.8 \times a\sqrt{3}$ at frequency 1050 MHz, and (e) experimental result for transmission coefficient between band gap in perfect crystal (red-dotted) and waveguide (blue-dotted) [32]

Zhao et al., [33] demonstrated experimentally the quadrupolar resonance of waveguides consisting of hollow pillars made of steel and glued by epoxy on the aluminium plate cornering at a sharp angle of $90^o$. Two mechanisms of excitation were used, (a) air-coupled transducer (ACT) and (b) polypropylene (PP) piezoelectric film. As for the case of wave detection, laser ultrasonic technique based on laser Doppler vibrometer (LDV, Polytec vibrometer OFV 2570) was used to measure the out-of-plane displacement. Fig. 2.11 (a) shows the straight hollowed-pillar waveguide with diameter, d=2.7 mm, and height 2.5 mm. The heights of hollowed pillars are half shorter than the heights of their neighboring solid (without inner radius) perfect pillars. The calculated and measured transmission are compared side by side and shown in Fig 2.11 (c) and (d). The former straight waveguides are then combined to form a continuous z-shaped path and the displacement field for the wave travelling within the route is illustrated in Fig 2.11 (f). The calculated transmission for P1 and P7 are illustrated in Fig 2.11 (g) and (h). Eventually, the three cornerings at a sharp angle of $90^o$ were formed and are $\pi$-shaped, as shown in Fig. 2.11 (i). Their displacement fields, calculated and measured transmission at P11, P7 and P11 are illustrated in Fig. 2.11 (j), (k) and (l) respectively. The displacement field in Fig. 2.11 (a),(e) and (i) clearly illustrates the ability of the defect region to control and confine the direction of the wave propagation along its designed trajectory.

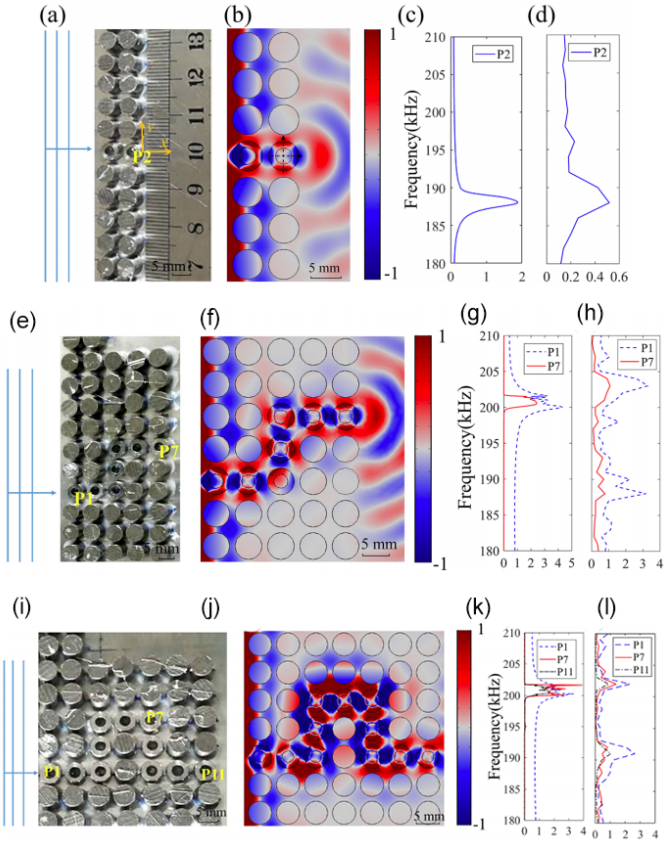


Figure 2.11: (a) Top view of straight waveguide with width, w=2.7 mm (b) numerical displacemnet field of straight waveguide at 189 kHz (c) calculated average z component (d) measured average z component (e) Z-shaped waveguide with width, w=2.56 mm (f) numerical displacemnet field of straight waveguide at 201 kHz (c) calculated (g) and (h) measured average z component at P1 and P7 (i) $\pi$-shaped waveguide with width 2.56 mm (j) simulated displacement distribution at 2 kHz (k) calculated (l) and measured for Z-component, where P1, P7 and P11 are represented in blue, red and black) [33]

Another experimental demonstration for an elastic waveguide with $90^o$ cornering was demonstrated by Baboly as illustrated in Fig. 2.12 [34]. Their system consisted of a 2D PnC made of circular air holes in an aluminum plate. The experimental demonstration observed a high transmission coefficient equivalent to -1 db for the straight waveguide. However, in the case of cornering waveguides, the transmission coefficient suffered a loss equivalent to 2.3 db, or 70 % transmission. The experimental setup consisted of a function generator, to supply a sinusoidal voltage to one of the two piezoelectric mounted on one side of the phononic crystal device. The wave detection used a similar transducer located on the opposite side of the emitter transducer. To filter the noise, a 4th order Butterworth filter was placed between the receiving transducer and the oscilloscope. A reference signal was recorded by using the same aluminium slab as the PnC device to normalise the transmission coefficient for all of the measured PnC devices.

Two measurements were conducted, one with the perfect crystal, as shown in Fig. 2.12(a)

and the other one with the waveguide path with distance, (b)$\alpha$=0.01, (c) 0.1 and (d) 0.5. It is noted in Fig. 2.12 that the $\alpha$=0.1 in Fig. 2.12((c) has a single confined mode (distinguished with red lines) that is suitable for better confinement. Fig. 2.12 (e) shows the displacement field and the transmission coefficient of the perfect PnC and waveguide bent at $90^o$ based on the waveguide $\alpha$=0.1. It is shown in the left displacement field in Fig. 2.12(e) that at the BnG between 0.25-0.287, the wave travelling in the waveguide suffered a leaky wave, and even reflected back towards the input source. However, at the BnG equivalent to 0.32, the wave can travel efficiently in the first straight waveguide and is able to couple effectively with the second straight waveguide at the $90^o$ cornering.

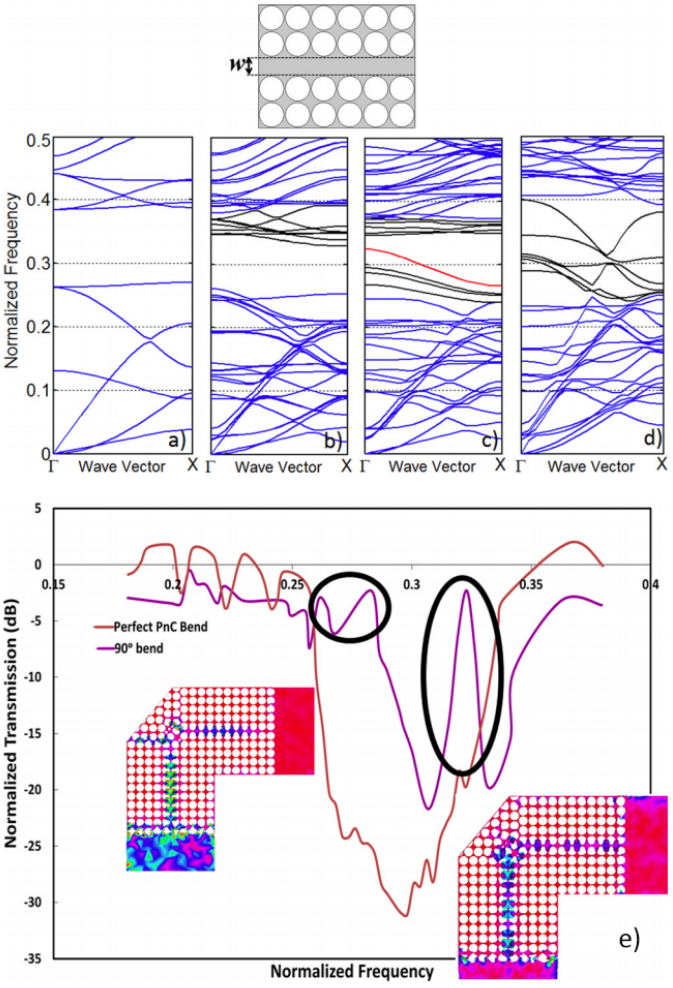


Figure 2.12: Dispersion curve for (a) perfect waveguide, and defect at (b) $\alpha$=0.01, (c) $\alpha$=0.1 and (d) $\alpha$=0.5, and (e) measured transmission between the bending waveguide and the perfect crystal. Two displacement felds were shown on the left for BnG between 0.25-0.287 and on the right for BnG at 0.32.) [34]

The PnC with tuneable waveguide properties can be achieved by using piezoelectric connected to an external circuit. Hu et al., [35] designed a tuneable waveguide based on the square PZT rod embedded in epoxy, which was connected to an external inductor

circuit to manipulate its properties. By appropriately modulating the external circuit for the piezoelectric PnC, the pass band can be introduced inside the band gap region to realise a waveguide. The square rod as arrayed in a square lattice was poled along the z-direction, while the two electrodes were connected to an inductor with inductance, L faced perpendicularly to the z-direction. Fig. 2.13(b) shows the band gap extended between 80 kHz to 185 kHz under the open-condition.

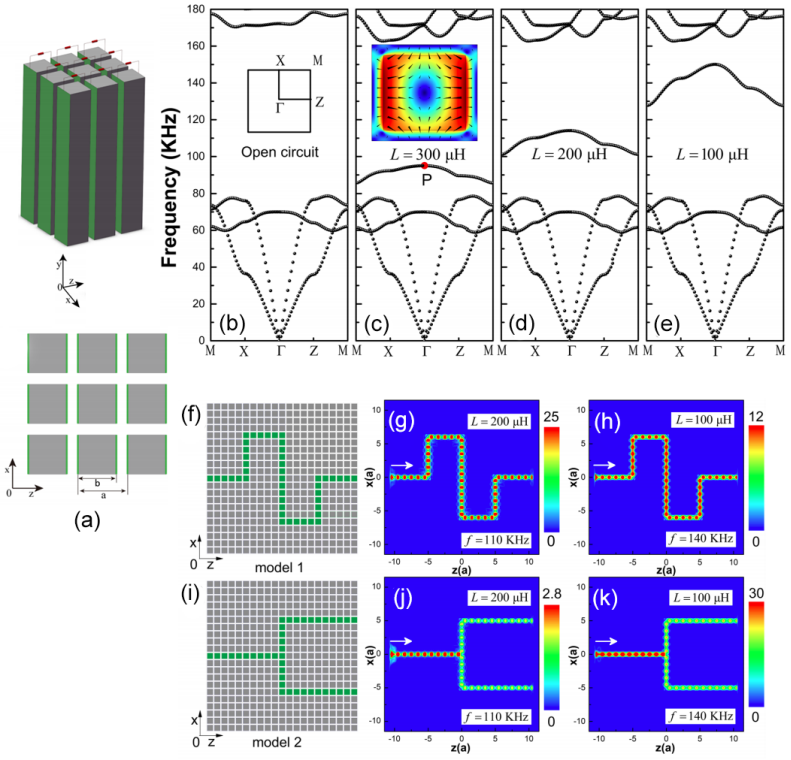


Figure 2.13: (a) (a) Piezoelectric PnC with external inductor circuit poled in z-direction. The green surface indicates the electrodes. The diagram above illustrates the structure in 2D in the $x$ and $y$ directions of (b)-(e) dispersion curves which corresponds to the open circuit, $L$=300$\mu$H, $L$=200$\mu$H, $L$=100$\mu$H. Inset of (b)-(c) respectively illustrates the first brillouin zone and the eigenstate at P point (f) -(h) model 1 with their respective power flux distribution for different inductance i.e., L=200 $\mu$H and L=100 $\mu$H at frequencies f=110 KHz and f=140 KHz and (i)-(k)model 2 with their respective power flux distribution for different inductance and frequencies) [35]

The results for the closed circuit with $L$=300 $\mu$H, $L$=200 $\mu$H, $L$=100 $\mu$H are demonstrated in 2.13(c)-(e). In Fig. 2.13(c) the displacement profile for p-points indicates the quadrupolar resonance that signifies the local resonance for the pass bands. It can be observed in Fig. 2.13 that with lower inductance, the passing band shifted towards the upper region within the band gap and covered larger frequency ranges. Later, Hu et al., [35] proposed a new approach besides conventional methods to create a waveguide, by changing the circuit condition of the designed PnC. Fig. 2.13 (g)-(i) shows the finite waveguide that follows a certain route, waveguide with $L$=200$\mu$H at frequency, $f$=110 kHz and waveguide

with $L$=100$\mu$H at frequency, $f$=140 kHz. With this ability, it is possible to create a split waveguide, as depicted in Fig. 2.13(i). In the next figure, (j) and (k) notice the splitting waveguides in action for the case $L$=200$\mu$H and $L$=100$\mu$H.

### 2.5.4/ THEORETICAL AND EXPERIMENTAL OBSERVATION ON WAVEGUIDING DEMULTIPLEXER

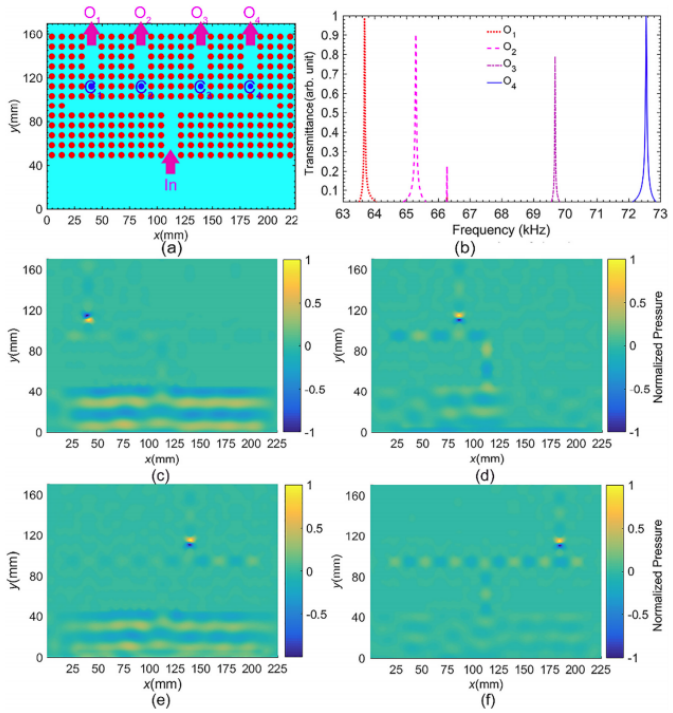


Figure 2.14: (a) Schematic of the fork-shaped demultiplexer from the top view, (b) four transmission narrow passing bands for four channel fork-shaped demultiplexer and (c) - (f) pressure distribution for the demultiplexer with cavity $C_1$, $C_2$, $C_3$, and $C_4$) [36]

Dogolsara et al., [36] in Fig. 2.14 numerically studied the acoustic demultiplexer based on the fork-shaped PnC consisting of four output channels, $O_1$, $O_2$, $O_3$, $O_4$. The PnC system consists of water cylinders arranged in a square lattice embedded in a mercury matrix. To create a stable device for the fluid-fluid-based design, the water environment was separated from mercury matrix by using ultra-thin elastic solid shells that have acoustic properties close to mercury. In the entrance route towards the output, four cavities filled with methyl nonafluorobutyl ether (MNE) with different radii, $C_1$, $C_2$, $C_3$, and $C_4$, were set up to carry the demultiplexing function over broadband acoustic signals, as shown in Fig. 2.14(a). The registered transmission at output $O_1$, $O_2$, $O_3$, $O_4$ are illustrated in Fig. 2.14(b) where four narrow pass-bands represented by $C_1$ (dashed-red) , $C_2$ (dashed-pink), $C_3$ (dashed-purple), and $C_4$ (dashed-blue) can be seen filtering the frequencies between 60–75 kHz. Their respective displacement distribution can be observed in (c)-

(e), where the acoustic propagation clearly ”choose” to propagate into one output per time signifying the demultiplexing function in action.

Jin et al., [37] studied the tuneable waveguide based on the square lattice hollow cylinder to exhibit the whispering-gallery modes (WGMs). It was found that the quality factor can be improved by introducing a thin layer of solid cylinder to separate the hollow cylinder from interacting with the slab background. In this case, the whispering modes will be confined within the upper hollow cylinder. The narrow pass band can be tuned according to the inner radius of the cylinder and consequently can be used to develop a system for wavelength multiplexers. A 5 by 5 supercell with Perfectly matched layer (PML) in the direction of the incoming wave was implemented. Two waveguides, $a$ and $b$, with different inner radius, $r_i^{(a)}$/a=0.145 and $r_i^{(b)}$/a=0.160 were designed on the same plate structure and separated by one row of solid cylinders. They were able to produce two narrow pass bands at normalized frequencies $f^a$ = 0.543 and $f^b$ = 0.581, as shown in Fig. 2.15(a). As can be noted in Fig. 2.15(b), the wave displacement shows two separate routes for wave propagation at two different normalized frequencies 0.543, and 0.581, as illustrated in Fig. 2.15(a). This approach can be exploited further to form a different wavelength into a single compact row, as shown in Fig. 2.15(c). Two inner radii were considered, $r_i^{(c)}$/a=0.145 and $r_i^{(d)}$/a=0.140 that produce two narrow pass bands at normalized frequencies $f^c$=0.571 and $f^c$=0.590. Fig. 2.15(d) clearly shows the displacement of the system at two different frequencies at $f^c$ and $f^d$.

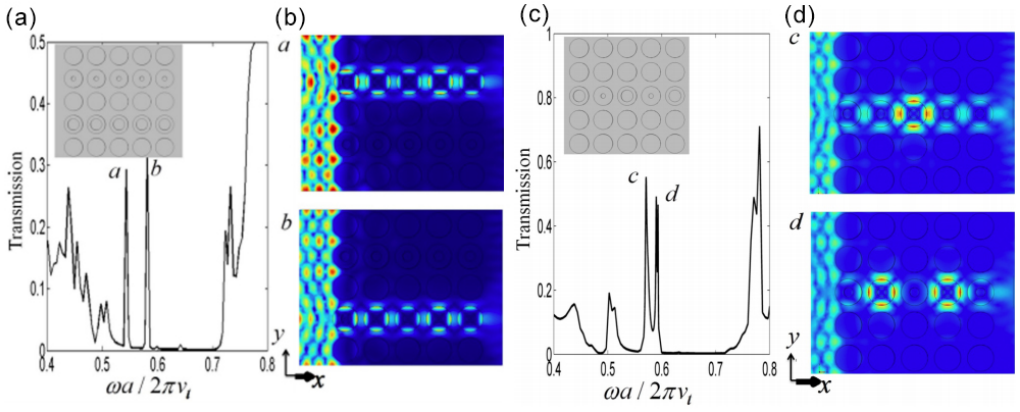


Figure 2.15: (a) (inset) top view for the schematic of multichannel wavelength demultiplexer (graph) transmission spectrum for waveguide with $r_i^{(a)}/a = 0.145$ and $r_i^{(b)}/a = 0.160$ at normalized frequencies $f^a$ = 0.543 and $f^a = 0.581$ (b) displacement field for frequency $f^a$ and $f^b$, (c) (inset) top view for the schematic of single channel demultiplexer (graph) displacement field for frequency $f^c$ and $f^d$ for $r_i^{(c)}$/a = 0.145 and $r_i^{(d)}/a = 0.140$ [37]

In another study, Jin et al., [38] showed the effect of liquid filling in the hollow cylinder with the demultiplexer capability depending on the physical properties and height of the fluid. With the presence of fluid, it was possible for the structure to support compression modes within the height of the cylinder to which the fluid filled.

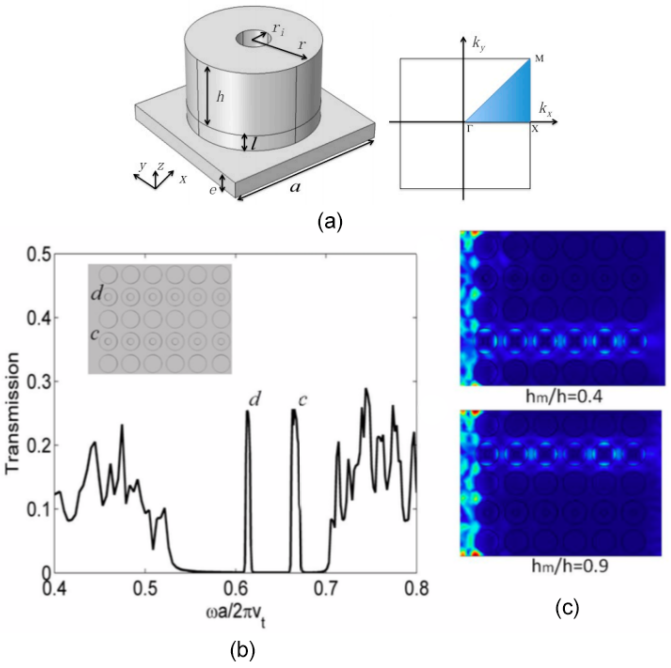


Figure 2.16: (a) Unit cell schematic where $r_i$ is the inner radius, $h$ is the height of hollow pillar, $l$ is the height of solid pillar, $e$ is slab thickness (b) (inset) top view schematics of the demultiplexer consists of two waveguides, $c$ and $d$ made up of two rows of hollow cylinders with similar inner radius, $r_i$ but difference height of fluid filling (graph) transmission coefficient for 2 waveguides, $c$ and $d$ (c) displacement distribution for (upper) waveguide $c$ and (lower) $d$) [38]

Fig. 2.16 shows the top view of the schematic multiplexer consisting of two waveguides, $c$ and $d$, made up of hollow cylinders with $h_m^c$/h= 0.4, $h_m^d$/h= 0.9, and a solid pillar with height, $l$/a = 0.2 to separate the hollow pillar from the cylinder. Both hollow cylinders for waveguides $c$ and $d$ have the inner radius, $r_i$/a= 0.11. The graph, demonstrated the transmission for waveguides $c$ and $d$, which are directly influenced by the height of the fluid. The higher the height of the pillar, $h_m$, the lower the transmission frequency. In this case, since the height of waveguide $d$ is equivalent to $h_m^d$/h= 0.9, which is higher than waveguide $c$ with $h_m^c$/h = 0.4, thus the transmission frequency for waveguide $d$ is lower than $c$, i.e., equivalent to 0.61. Their displacement distribution are represented in Fig. 2.16 (c).

In another research, Feng et al., [39] introduced the concept of rainbow guiding by using the Lamb modes, which consists of hollow and solid steel pillars glued by epoxy on the top of the aluminium plate. The rainbow guiding is popularly referred to in optics and is known as ”rainbow trapping” to signify the stopping frequency at different ranges and positions. In PnC, several approaches were introduced among others by using graded structures [40, 41] , Mie resonance-based [42] and space-coiling metamaterials [43]. To generate the incoming wave experimentally, the unfocused air-coupled transducer (ACT)

with central frequency 200 kHz was used. The detection was based on the laser ultra sonic laser Doppler vibrometer (LDV, Polytec vibrometer OFV 2570). Two models were fabricated based on the Symetric structure (SS) which consists of hollow pillars between the solid pillars located in the upper row - refer Fig. 2.17(a) and the antisymetric structure (AS), which consists of hollow pillars on the upper row alone - refer Fig. 2.17(b).

The measurement for the SS structure were shown in Fig. 2.17(c) where, the average transmission, T, was measured for the upper and lower hollow pillars at the horizontal position marked with the yellow lines 1, 2, 3 and 4. The results show that for the solid pillar (marked with a black solid line), no transmission was observed. However, with the hollow pillar diameter, d=2.9 mm at 1 and 2, two peaks with solid and dotted red lines at centered frequencies, f = 160 or 158 kHz can be observed. Similarly, for the hollow pillar diameter, d=2.7 mm at 3 and 4, two peaks with solid and dotted blue lines at centered frequency, f = 177 kHz can be observed. Regarding the AS structure, a clear distinction between the two peaks that represent hollow pillars d=2.9 mm (red lines) and 2.7 mm (blue lines) can be observed.

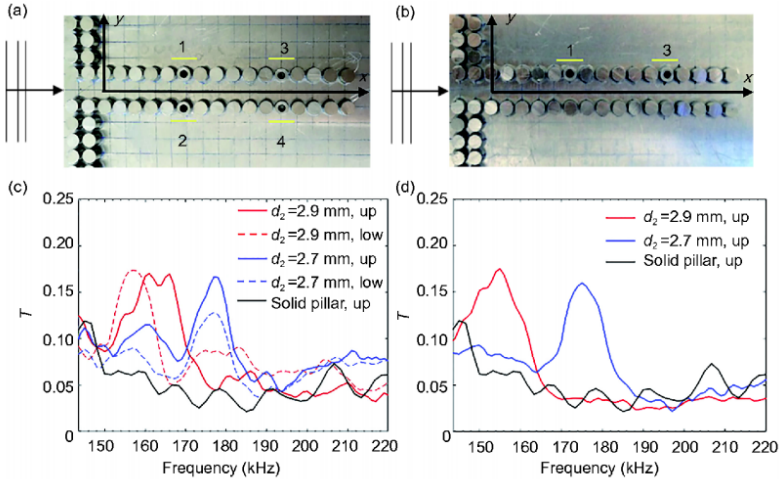


Figure 2.17: Top view for fabricated (a) SS (b) AS, transmission coefficient versus frequency for (c) SS and (d) AS.) [39]

Ali et al., [44] presented an empirical demonstration of a phononic demultiplexer with a single resonator. The demultiplexer is a waveguide in Y-form with an input row and two lines of output. Each output line contains a single resonator, which was grafted away from the input line at a given position. The analytical expressions for the selective transfer of a single propagation mode through one line are created by holding the other line unimpacted. Fig. 2.18 shows the first output line contains one height d1 resonator inserted at site 2 at a distance d2 from input 1. Similarly, the demultiplexer's second output line contains one height d3 resonator inserted at site 3 at a distance of d4 from input 1.

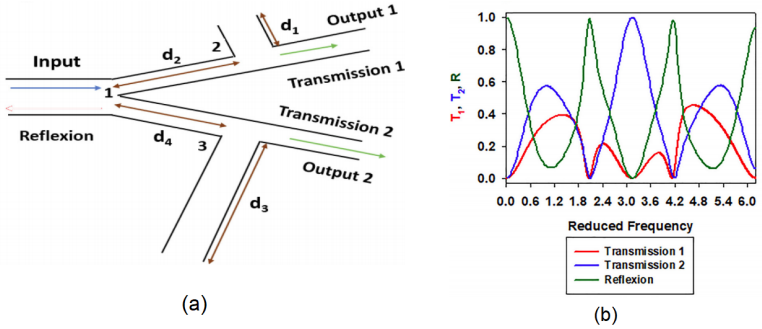


Figure 2.18: (a) Schematic diagram of a Y-shaped demultiplexer with one input line and two output lines. (b) Variation of transmitted signal amplitude in output 1 (red line), output 2 (blue line), and reflected signal (green line) of demultiplexer [44]

### 2.5.5/ PHONONIC CRYSTAL DEMULTIPLEXING LITERATURE (2003-2020)

The following tables 2.1, describes all of the related papers concerning the demultiplexer application using phononic crystal to understand the research gap that this thesis would like to achieve. The table's objective is to collect, analyze, categorise, and summarize the details related to the demultiplexing of phononic crystals to date.

It must be noted that the following lists are delimited to the passive control of elastic/ acoustic wave demultiplexing, which is the relevant focus of the current thesis study. The literature that concerns with active control for acoustic/elastic demultiplexers that manipulate electronic active gates or electrically switchable properties to filter the wave are excluded. Example of such study can be found for instance, in Li et al., [45].

Another important point is that a clear distinction should be made between merely splitting the wave and the demultiplexer. In this case, all demultiplexing capabilities have the potential to split the wave but not all splitting studies involve the demultiplexing application. A clear distinction can be made as a demultiplexer can separate waves according to different wavelengths, but wave splitting can involve routing the wave into two waveguide outputs (for Y-shaped) with similar wavelengths. An example of demultiplexing can be referred to in the study by Pennec etc al., or Abdelkrim et al., where distinct frequencies transmissions are transmitted into different outputs, signifying the demultiplexing in action. On the other hand, a study by Wang et al. showed that even if it involves splitting the wave into two output channels, the transmitted frequencies between the two involve a similar range, thus signifying mere splitting with no demultiplexing in action, as shown in Fig. 2.19b [46]

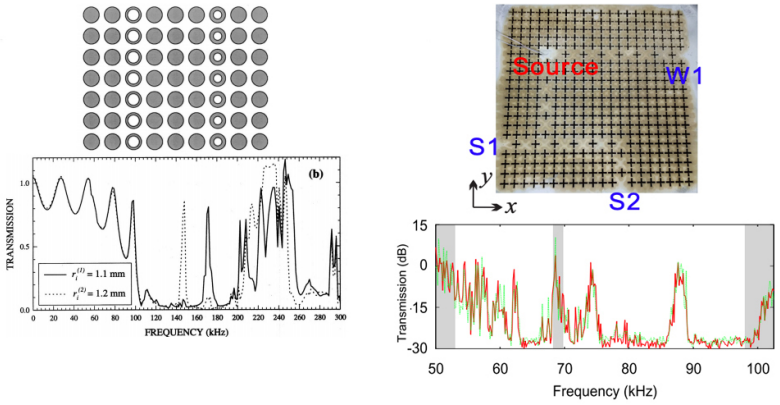


(a) (b)

Figure 2.19: (a) theoretical study of demultiplexing by Khelif et al., 2003 with two channel defects of radius $r_1$=1.1 mm and $r_2$=1.2 mm to produce two distinct narrow pass band frequency filters, and (b) experimental wave splitting by Wang et al., (2008) with two output channels, S1 and S2 that give no frequency transmission distinction between the two as highlighted by the green and red lines, signifying mere splitting wave with no demultiplexing in action

Table 2.1: List of publications on PnC demultiplexing based on different configurations and setups since 2003-2020

| Objective and Findings | Reference |
|---|---|
| Theoretical study on Finite Difference Time Domain (FDTD) for narrow pass bands demultiplexer via modification of inner radii size of two hollow steel cylinders embedded in water. By regulating the inner radii of the tubular steel inclusions, the frequency at which the pass band occurs can be tuned at 148 kHz and 170 kHz. | Khelif et al., 2003 |
| Theoretical study on Finite Difference Time Domain (FDTD) for narrow pass band in Y-shaped demultiplexer via inner radii size or fluid properties inside cylinders. The frequency of the waveguide could be chosen by modifying the inner radii of the void cylinders or by altering the composition of the fluid that fills them. Waves at two different frequencies (154 kHz and 139 kHz) can be transported by a waveguide made up of two hollow cylinders of different inner radii. The transmission of waves at one or both of these frequencies are possible by selectively filling the cylinders with water or mercury. | Pennec et al., 2004 |
| Theoretical study on narrow pass-band demultiplexer via coherent 1D and 2D mass-spring networks. By altering the mass and stiffness coefficients of the waveguide components, the frequency of the waveguides can be selected. | Aly et al., 2016 |

| Objective and Findings | Reference |
|---|---|
| Theoretical study on Finite Element Methods (FEM) for PnC made of silicon which consists of a hollow cylinder on top of a thin slab structure. The narrow pass band at reduced frequencies 0.543 and 0.581 inside the Bragg band gap can be tuned by adjusting the inner radius of the hollow cylinder. | Yabin et al., 2016 |
| In a phononic crystal structure, when one linear waveguide is close enough to another, the coupling effect between the two waveguides is so strong that they are connected as a single system. Zou et al., theoretically studied on FEM by decoupling 2 PnC waveguides acoustic demultiplexers in narrow 168 kHz and 159 kHz frequency ranges by adjusting the number of pillars in one waveguide. The PnC structure consisted of a solid/solid structure of steel cylinder on top of epoxy. | Zou et al., 2017 |
| Theoretical study on plane wave expansion (PWE) method for fork-shaped demultiplexer consisting of four cylindrical cavities ($O_{1-4}$) of different radii ($r_{1-4}$) filled with methyl nonafluorobutyl ether (MNE) at the throat output. The system is consisted of a square lattice of cylindrical water inclusions in a mercury matrix, separated by ultra thin solid shells. Each cavity can serve as a wave demultiplexing, selecting from the input signal a narrow band to which the frequency correlates with the cavity's eigenmode. The frequencies of filtering between 60–75 kHz can also be adjusted by the temperature adjustment. | Dogolsara et al., 2019 |
| Theoretical study on FEM for narrow-pass band GHz-ranged demultiplexer consisting of 3-outputs channels with three different rods' radii ($r_{1-3}$). Each of the three radii can filter a frequency range of 1 to 1.2 GHz. A square series of infinitely long Tungsten rods embedded in the PMMA matrix with lattice constant a equivalent to 500 nm forms the PnC demultiplexing system. | Moradi et al., 2019 |
| Theoretical study on FEM for Y-shaped thermal switching solid-fluid consists of a periodic arrangement of ethanol rods embedded in a square Quartz. To achieve MHz-ranged demultiplexing frequencies, the lattice constant $a$ equivalent to 880 µm was considered. The behavior of band gaps and defect modes depend on the temperature that can tune the frequency position and the radii of defective rods at $r_1$=0.79*r and $r_2$=0.88*r. | Mehran et al., 2019 |

| Objective and Findings | Reference |
|---|---|
| Theoretical study on FEM for narrow pass band of eight channel demultiplexer. The basic structure was created by a square arrangement of tungsten background holes filled with water. The proposed structure consists of nine types of lines defects made up for input and output channels. Each output waveguide, hollow cylinders have different inner radii that can transmit various narrow frequency passbands between 166.6 kHz and 168.1 kHz. | Motaei et al., 2020 |
| Theoretical study for three heterostructure demultiplexers containing circular tungsten cylinders on top of polycrystalline silicon substrate based on the ring resonators of solid-solid PnC. The heterostructure consists of three distinct sections, each section comprising a bus waveguide and an output waveguide linked to each other through a ring resonator. The results of the simulation that show different frequencies are emitted in 3 GHz range frequencies at 5.8401, 5.7703 and 5.7201 GHz from the heterostructure demultiplexer outputs. | Babaki et al., 2020 |
| Theoretical study on Y-shaped PnC demultiplexer based on Acoustic Induced Transparency (AIT) that depends on the length of waveguide resonators. The demultiplexer has an input line and two output lines of Y-shaped waveguide. Each output line contains a single resonator grafted away from the input line at an output path that decides the reflection and transmitting frequencies. | Kadmiri et al., 2020 |
| Theoretical study on kHz narrow band width of Y-shaped demultiplexer based on Fano and AIT. Two resonance stubs with different lengths are grafted at two output lines located far from the input line that can provide a selective transfer through one line while silencing the other line. | Mouadili et al., 2020 |

From the state of art listed in Table 2.1, the following are the summaries of their methods to achieve the demultiplexing.

- The current research used inner-radius defect, fluid/ material properties, Acoustic Induced Transparency (AIT), ring resonance, and thermal influence to deliver the demultiplexing functions. Depending on the dimension, the transmitting frequencies vary from kHz to GHz ranges. The smaller the dimension of the demultiplexer, the higher the transmitting frequencies for the given demultiplexing system. However, all of the reported studies produced limited and narrow pass-band transmission that resulted in a tight and slender filtering ability from the input frequency to output.

- Several studies used a non-definitive demultiplexing technique that depends on the property of the fluid and the thermal effect, whereby both were subjected to the surrounding factor. To preserve the filtering capacity in such a system, a pristine environment is required. The thesis aims to produce a straightforward approach of PnC demultiplexing system that has a definitive behavior that does not subject to environment changes as compared to previous studies.

- • From the earliest report on PnC demultiplexing in 2003 to the latest report in 2020, the wide and continuous frequencies of the PnC demultiplexer have never before demonstrated both the simulation and experimental studies. Thus, this is the aim of the current research.

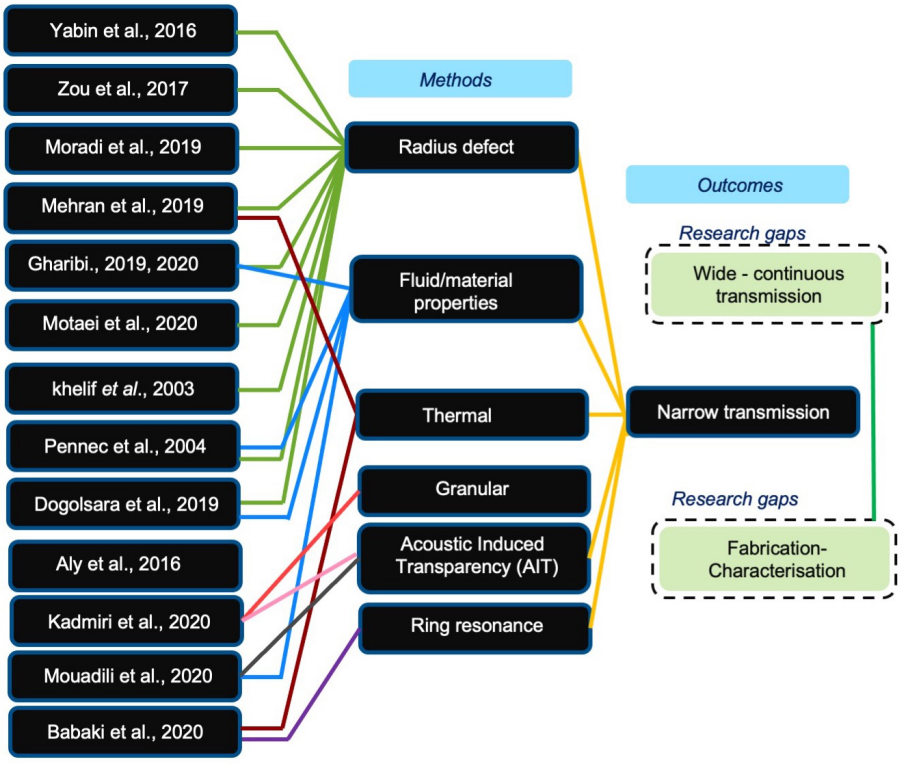


Figure 2.20: Schematic diagram for state of art PnC demultiplexing from 2003-2020

## 2.6/ SIMULATION METHODS FOR ELASTIC WAVE PROPAGATION

### 2.6.1/ FINITE ELEMENT METHODS (FEM)

The finite element method, known as FEM, is widely used in numerical simulation for solving equations in partial derivatives to describe the physical phenomena. The FEM is suitable for solving almost all types of partial differential equations (PDEs) that govern

any physical problem, in particular the equations for the propagation of elastic waves. The origin of FEM can be traced back to structural analysis before its method was expanded to another problem, such as electromagnetic waves in 1968. Historically, its first application and uses were mainly focused on the problems related to mechanical structures for stress and deformation solutions in elastic media. Due to its versatility, FEM can also find its path towards phononic research and is also applicable to the case of acoustic / elastic waves of the propagation in phonon media. Indeed, the method is capable for solving the eigenvalues problem, thus allowing the computation of the bands structure.

Among its applications in phononics, for instance the works of Khelif et al. [47], who used it to calculate the dispersion curves of a two-dimensional phononic crystals consisting of cylindrical inclusions in a plate. A similar study for band gap opening that includes the guidance of elastic waves was also studied, for instance by Pennec et al., [48] using the finite element method. Another research team, T. Chen and T-T. Wu [49] also used similar approaches to study phononic crystals consisting of cylinders periodically deposited on an aluminum plate. In all of these studies, the FEM method has shown its efficiency in terms of convergence and computation time, as compared to the other computational methods, such as PWE. Basically, the FEM for any type of problem involves four steps: a) discretization of the problem region into subdivisions or finite number of elements, b) identifying the governing equations for a problem of interest in a typical element, c) assembling all the finite elements in the region and d) solving the system equation.

### 2.6.2/ DISCRETIZATION OF THE DOMAIN

In finite element analysis (FEA), the domain of interest is discretized into small elements connected at the nodal points. The solution for the problem is approximated at an individual finite element from one nodal point to another until a full model solution is analysed to form a complete model.

This method is similar to the finite difference method in which the solution regions are represented in a series of an array of grid points. However, its application becomes inconvenient for irregularly shaped geometry because of the regular rectangular grids that they use. Regular rectangular grids are not only inconvenient for curved boundaries or interfaces, they are also not a suitable solution for problems with very steep variation of fields. Due to this issue, the FEM is more preferable compared to its finite difference method counterpart. An unadorned form of function is used in FEM to estimate the field for each element. Consequently, the possible errors for the solution are reduced as the finite number increases.

In previous approaches, the solution does not involve any discretization or subdivision process for domain problems. Instead, the system is modeled based on analytical

functions for the whole domain and is usually only applicable for simple geometry. Due to this fact, the FEM is applicable to solve any complex domain and its usage can be traced from electromagnetic wave problems, heat treatment, acoustic/elastics waves, etc.

## 2.7/ METHOD OF FABRICATIONS

### 2.7.1/ ADDITIVE MANUFACTURING FOR PHONONIC CRYSTAL MANUFACTURING

The additive manufacturing can be used to fabricate a phononic crystal that operates in the range of 100 kHz to 1 MHz [50] which suits with our operating frequency of 247 kHz to 370 kHz. In the background literature, it was found that many researchers and academics generally implement the AM technologies based on their functional framework such as the material categories, AM technologies, AM material, layer formation technique, etc. Most of the current reports for AM were used to fabricate a 3D PnC [51–55]. While there are several types of machines in development, they are all similar in that they create three-dimensional shapes by combining a number of two-dimensional slices. For instance, Wormser et al., [55] used the selective electron beam melting (SEBM) to develop cellular auxetic structures based on Ti-6Al-4V with a particle size between 45 $\mu$m and 105 $\mu$m, as illustrated in Fig. 2.21. The final product has a negligible porosity percentage below 0.5 $\%$ and the transmission measurement shows a reasonable agreement with the numerically obtained PnBG. In addition, the PnBG was already experimentally verified in two others reports by the same author [52, 54]. Lucklum et al., [51] fabricated 800 $\mu m$ holes for a 15x15x15 cubic crystal with a 1 mm lattice constant, as illustrated in Fig. 2.22, based on a stereolithography printer and using a high-temperature acrylic polymer. Experimental results for devices up to 100 $\mu m$ in feature sizes successfully indicate the PnBg behavior needed for applications such as sensor and microsystem structures. D'Alessandro et al., [53] has developed the prototype of the finite crystal structure based on polyamide with the assistance of additive production technology. They successfully demonstrated the phononic band structure that displays a 132 $\%$ gap-mid gap ratio, which is the highest complete 3D bandgap in literature for any phononic crystals. The spectra of measured and numerical transmission are in good alignment and current attenuation of up to 75 dB for a three layer crystal. Tol et al., [56] fabricated of a 3D-printed Gradient-Index Phononic Crystal Lens (GRIN-PCL) based on thermoplastic PA2200 bonded on an Al metallic host structure. The PA2200 was fabricated by using 3D printed selective laser sintering technique. By applying a thin layer of epoxy between the 3D printed layer and aluminum, the manufactured 3D printed lens layer was further bonded to the Al plate with a vacuum bonding procedure, allowing it to cure under vacuum for 12 hours. Due to its high shear strength (27.58 MPa when bonded to the aluminum), 3 M ScotchWeldTM DP460 two-part epoxy was chosen for bonding layer.

Despite some difficulties discussed by the researcher about the AM process on Aluminium alloy, the result shows a good agreement between the simulated transmission with the experimental measurement. For instance, Sercombe et al. [57] highlighted how aluminum laser melting poses several challenges which includes oxide layer stability, poor flowability, high reflectivity, and high thermal conductivity. One of the key problems faced when processing Al by AM has to do with difficulties in spreading the powder bed due to poor powder flowability [58]. In addition, because of the high reflectivity of the powder and the high thermal conductivity of the solidified material [59], the AM process of aluminum alloys generally requires high laser power. The chemical composition of the powders is another important element. They often have a high degree of contamination, due to their high surface area per unit volume, which can be caused by moisture, adsorbed gases and oxide films present on the particle surface [60–62]. As a result, the contaminant can also undermine the physical properties of the consolidated products. In addition, all of the above mentioned difficulties will provide a real challenge as in simulation these difficulties are not considered and are assumed under perfect conditions.

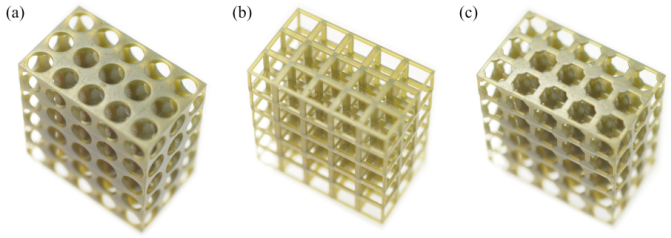


Figure 2.21: 3D model for simple cubic phononic crystals with a constant 3 mm lattice consisting of (a) three cylindrical holes (b) rectangular scaffolds, and (c) angular balls bound by cylindrical beams [63]

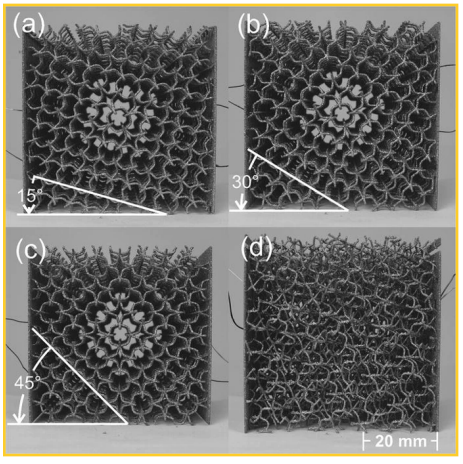


Figure 2.22: Fabrication samples with (a) rotation of 15 axis, (b) 30 axis and (c) 45 axis along the sample length axis. [54]

## 2.8/ METHOD OF MEASUREMENTS

### 2.8.1/ MICRO SYSTEM ANALYZER (MSA) METHOD

Laser Doppler vibrometry (LDV) is currently the best non-contact velocity and displacement measurement tool which is used in many fundamental science fields, such as for the analysis of high frequency domain, for finite element method verification and updating, acoustic and noise source location, and small-fault detection in structure. Light, as a sensor does not impact the sample, keeping it non-invasive and therefore allowing measurements on extremely small and extremely lightweight structures. With its ”remote” measurement technique, the LDV method can be used to measure a measurand at a large distance beyond 30 m and with a 1-2.5 % RMS accuracy. With this capability, LDV methods not only can measure a surface vibration over MEMS size in small scale, but also over a large civil structure [64]. Some advantages of the LDV over other equivalent measuring devices are the ability to be directed to targets that can be too small or too hot to attach by a physical transducer. With regard to the traditional vibration sensors such as accelerometers, the LDV methods have extended the measurement capabilities with its non-intrusive single point laser vibrometer, such as high spatial resolution measurements with little time, higher frequency band width up to 24 MHz, and higher resolution for a velocity detections as small as 0.5 $\mu$m/s and ± 30 m/s for displacement.

The LDV operates based on the Doppler phenomenon that occurs when the laser light from a vibrating surface disperses. The surface's velocity is then converted as a Doppler frequency shift of the laser light which can be extracted through interference between the object and the reference beams. A laser beam with wavelength, $\lambda$ is projected onto an object moving at velocity, $V$ in a single-beam LDV. The changed frequency, $f_d$ of the reflected laser beam is proportional to the object's velocity due to the Doppler effect, and can be expressed as [65] :

$$f_d(t) = \frac{\mathbf{V}(t) \cdot \mathbf{S}}{\lambda} \tag{2.10}$$

where $\mathbf{S} = e_i - e_o$ is the sensitivity vector and $e_i$, $e_o$ are illumination and observation unit vectors, respectively [65]. The laser doppler vibrometer operates on the principles of optical interference (the difference in length of the path between the two beams), when two main coherent light beams with light intensities $l_1$ and $l_2$ are needed to overlap.

The cumulative strength of both beams is not only the number of the respective intensities, but is also modulated by the following formula :

$$I = I_1 + I_2 + 2\sqrt{(I_1 + I_2)cos}\left[\frac{2\pi(r_1 + r_2)}{\lambda}\right] \tag{2.11}$$

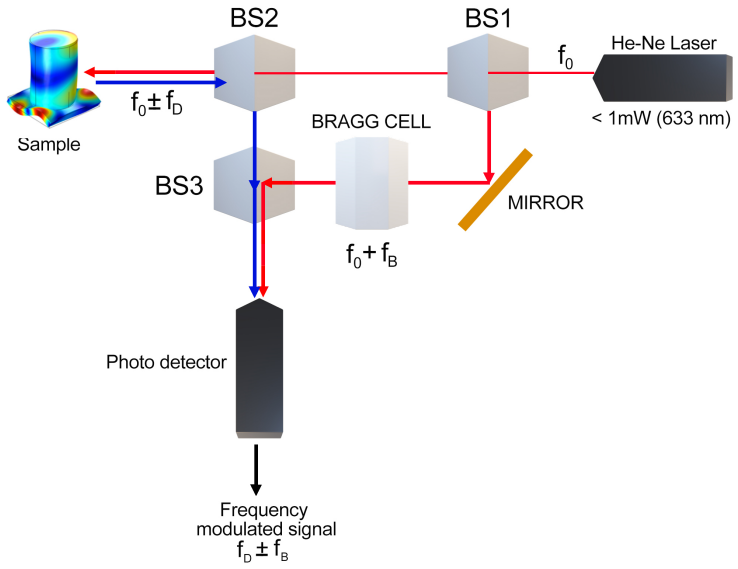


Figure 2.23: Working principle of Micro System Analyser

Details of the phenomena is described as follows and illustrated in Fig. 2.23. A laser beam is divided into a reference beam and a measurement beam by a beam splitter (BS 1). The helium – neon laser is the most common type of laser in an LDV, while laser diodes, fiber lasers, and lasers with Nd: YAG are also used. After passing through a second beam splitter (BS 2), the measurement beam is directed onto the sample surface, which then reflects it. This reflected beam is then deflected downwards by BS 3 (see figure), and then combined onto the detector with the reference beam. As the reference beam's optical path is constant over time, a surface movement on the sample will produce a light / dark pattern on the detector which represents an object displacement which is equivalent to half of the wavelength of the light source used.

The following Table 2.2 summarises the MSA instruments used in the thesis:

Table 2.2: MSA-500 for standards (1 MHz) out-of-plane configuration systems components and characteristics

| System component | Components | Characteristics |
|---|---|---|
| MSA-500 Optics | Light source | 525 nm wavelength |
| | Beam diameter | 0.9 $\mu$m |
| Junction Box | Input signals | ± 200 mv |
| | Excitation booster | 10 V / 50 mA peak amplitude |
| System | Computer | Intel i7 Quad-Core CPU, 16 GB RAM |

### 2.8.2/ Scanning Laser Doppler Vibrometry (SLDV) method

A Polytec Scanning Vibrometer (PSV) is another useful instrument, other than the Micro System Analyser (MSA), that operates based on the Laser Doppler Vibrometer approach. Both are non-contact instruments for measuring surface vibrations and are very useful for an FEM validation study or to study structure dynamics/vibration. By sending a laser on an oscillating surface, the PSV measures the amplitude and the frequency of the vibrations of the surface. The oscillations of the sample surface cause a change in the optical path of the measurement beam over time, thus introducing a frequency ”shift” to the beam by the Doppler effect. This results in the creation of interference fringes at the level of the detector. The displacement profile that was executed to study the dynamics of our device was carried out with the collaboration of Mr. Florent Deux's group from Polytec Paris.

## 2.9/ Conclusion

The second chapter gives a general overview of phononic and photonic history and their inherent similarities. Several important concepts, such as the geometry of the crystal lattice resulting from the phenomena of the band gap, were also mentioned. The chapter also addressed the previous method of PnC demultiplexing and their disadvantages was summarized in more detail. Particularly, the inherent narrow pass-band transmission was the key source of filtering disadvantages of previous filtering approaches that restricted their filtering function. The other drawbacks were also the lack of experimental work on the current phononic demultiplexing reports. The chapter also presented the numerical and calculation components used in the current dissertation. The fundamental aspects of finite element-based simulation methods to research various PnC phenomena and the experimental methods, such as the method of wave generation and detection, were also discussed.

# 3

# PHONONIC SIMULATION FOR DEMULTIPLEXING APPLICATION

## 3.1/ INTRODUCTIONS

In the field of wave propagation, numerical study has long been applied in electromagnetism to solve the Maxwell's equations. In this case, photonic crystals have been the subject of intensive studies that use many numerical techniques for their wide applications, for instance, Plane Wave Expansion (PWE), The Transfer Matrix Method (TMM), Multiple Scattering Theory (MST) and more recently, wavelet decomposition. Other algorithms based on other computational approaches have also been used, such as Finite Difference Time Domain (FDTD) and Finite Elements Method (FEM) which operate based on the defined mesh of the domain. During the last two decades, some of these methods, in this case the PWE, MST, and FDTD, have been used to simulate an elastic or acoustic waves in phononic crystals and have become essential tools for simulating the mechanical behavior of PnC for their dispersion curves and transmission coefficients. Each of these numerical methods have different formulations and therefore, they have their own advantages and disadvantages when it comes to study one system to another. In this chapter, the main interest is to focus on theoretical aspects on various properties of PnC using FEM methods based on Comsol Multiphysics software. Details of the different stages of simulation concerning the calculation of the band structures, the displacement fields, and the transmission coefficient to develop a fully functional PnC demultiplexing system are discussed.

## 3.2/ SIMULATION STAGES FLOW

The following flow-chart in Fig. 3.1 summarises three simulation objectives described in this chapter. In the first step of simulation, a complete band gap for frequency versus

wave vector, $k$ in a three-direction of Brillouin zone was calculated. To achieve this, a unit cell structure consisting of a pillar embedded on a slab structure was considered. The second objective is to simulate different waveguiding structures for multiple-filtering frequencies using a supercell technique. The third objective is to simulate transmission coefficient for both complete band gap and frequencies filtering by using a finite structure equipped with a perfectly matched layer (PML), excitation and detection source of elastic waves propagation.

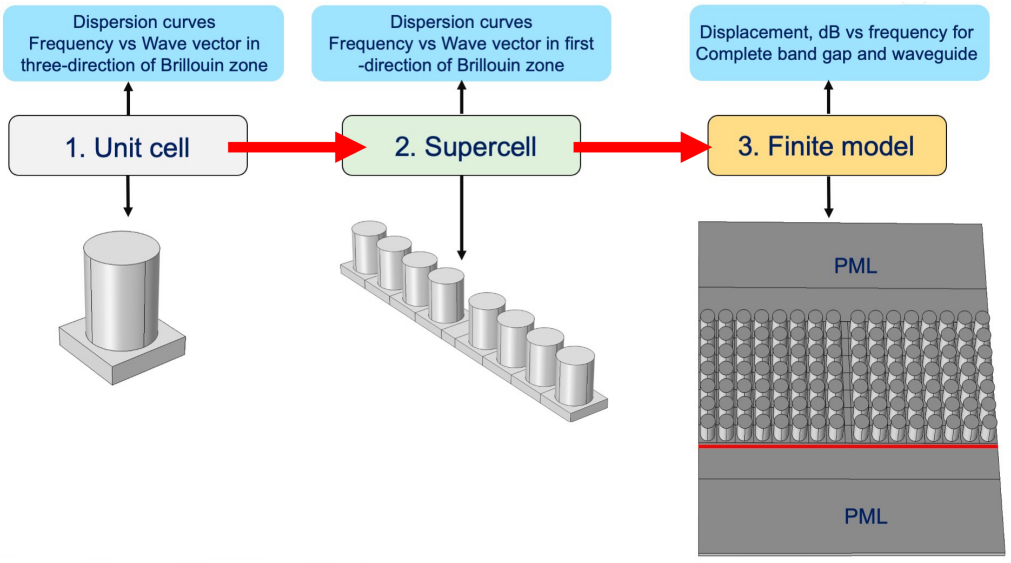


Figure 3.1: Stage of simulation process

## 3.3/ UNIT CELL AND METHODS OF CALCULATION

The basic model studied in this thesis is represented by a two-dimensional periodic structure of cylinder pillars on top of a slab structure made of aluminium alloy, $AlSi_7Mg0_6$. The cylinders are chosen to form resonators, which activate local resonance at very low frequencies within the host environment. Fig. 3.2 shows the structure in the three-dimensional space with the direction Z is parallel to the axes of the cylinders. The periodicity of the unit cell structure, the height and the radius of the pillar will be denoted as $a$, $h_p$ and $r$ respectively. In practise, as the structure will be fabricated via a 3D metal printer, the substrate should numerically not be less than 1 mm. This is to ensure the device's durability to stand the residual stress due to expansion and contraction, which are the heating and cooling effects during the printing process. Should the substrate be very thin, the substrate might not be able to stand the residual stress and defects such as warpage of the base or even cracking might occur.

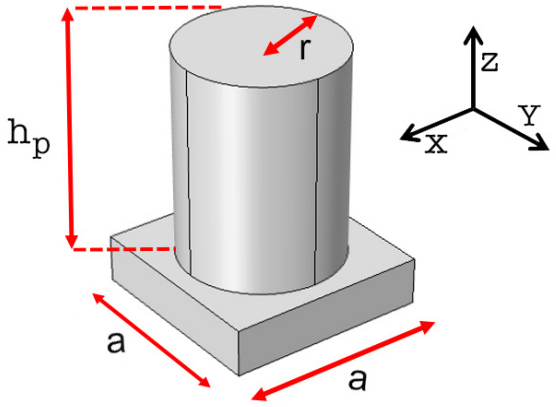


Figure 3.2: PnC unit cell with pillar deposited on a slab substrate

### 3.3.1/ Finite Element Modeling with Comsol Multiphysics

### 3.3.2/ Implementing equations

This section discusses about the equations of motion to study the propagation of stress through an elastic solid. Considering a small velocity and displacement and ignoring the body force (such as gravitational force), the $2nd$ law of Newton writes :

$$\rho\frac{\partial^2 u}{\partial t^2} = \frac{\partial x_x}{\partial x} + \frac{\partial x_y}{\partial y} + \frac{\partial z_z}{\partial z} \tag{3.1}$$

where $\rho$ is density. From stress-strain relation,

$$x_x = \lambda\Delta + 2\mu e_{xx} \quad ; \quad x_y = 2\mu e_{xy} \quad ; \quad x_z = 2\mu e_{xz} \tag{3.2}$$

substitute relation (3.2) into (3.1), the displacement component for $u$ is:

$$\rho\frac{\partial^2 u}{\partial t^2} = (\lambda+\mu)\frac{\partial \Delta}{\partial x} + \mu\nabla^2 u \tag{3.3}$$

to describe the propagation of wave in a homogeneous, isotropic and elastic material for displacement u:(u, v, w), we come to the $Navier - Cauchy$ equation:

$$\rho\frac{\partial^2 u}{\partial t^2} = (\lambda+\mu)\nabla\Delta + \mu\nabla^2 u \tag{3.4}$$

Alternatively, to describe the harmonic wave propagation motion in an isotropic medium, the following equation should be considered:

$$F = -\rho\omega^2 u_i = \partial T_{ij} \partial X_j \tag{3.5}$$

Where $\rho$ is the density, $\omega$ is the angular frequency, $u_i$ is the displacement field, $T_{ij}$ is the stress tensor and $X_j$ is the coordinate vector in the cartesian coordinate system. The stress tensor $T_{ij}$ can be related to the strain tensor $S_{kl}$ by the following Hooke law :

$$T_{ij} = C_{ijkl} \times S_{kl} \tag{3.6}$$

where $C_{ijkl}$ is the tensor of elasticity. By applying Einstein's law for the repetition of indices, the stresses and deformations for the Hooke's law can be rewritten with the coefficients $\alpha, \beta$ in the form:

$$T_\alpha = C_{\alpha\beta} \times S_\beta \tag{3.7}$$

For an isotropic material, the elasticity tensor for $C_{\alpha\beta}$ is equal to:

$$C_{\alpha\beta} = \begin{vmatrix} C_{11} & C_{12} & C_{12} & 0 & 0 & 0 \\ C_{12} & C_{11} & C_{12} & 0 & 0 & 0 \\ C_{12} & C_{12} & C_{11} & 0 & 0 & 0 \\ 0 & 0 & 0 & C_{44} & 0 & 0 \\ 0 & 0 & 0 & 0 & C_{44} & 0 \\ 0 & 0 & 0 & 0 & 0 & C_{44} \end{vmatrix} \tag{3.8}$$

From (3.1) then

$$\begin{cases} -\rho\omega^2 u_x = \frac{\partial}{\partial x}\left(C_{11}\frac{\partial u_x}{\partial x} + C_{12}\frac{\partial u_y}{\partial x} + C_{12}\frac{\partial u_z}{\partial z}\right) + \frac{\partial}{\partial y}\left(C_{44}\frac{\partial u_x}{\partial y} + C_{44}\frac{\partial u_y}{\partial x}\right) + \frac{\partial}{\partial z}\left(C_{44}\frac{\partial u_x}{\partial z} + C_{44}\frac{\partial u_z}{\partial x}\right) \\ -\rho\omega^2 u_y = \frac{\partial}{\partial x}\left(C_{44}\frac{\partial u_x}{\partial y} + C_{44}\frac{\partial u_y}{\partial x}\right) + \frac{\partial}{\partial y}\left(C_{12}\frac{\partial u_x}{\partial x} + C_{11}\frac{\partial u_y}{\partial y} + C_{12}\frac{\partial u_z}{\partial z}\right) + \frac{\partial}{\partial z}\left(C_{44}\frac{\partial u_y}{\partial z} + C_{44}\frac{\partial u_z}{\partial y}\right) \\ -\rho\omega^2 u_z = \frac{\partial}{\partial x}\left(C_{44}\frac{\partial u_x}{\partial z} + C_{44}\frac{\partial u_z}{\partial x}\right) + \frac{\partial}{\partial y}\left(C_{44}\frac{\partial u_y}{\partial z} + C_{44}\frac{\partial u_z}{\partial y}\right) + \frac{\partial}{\partial z}\left(C_{12}\frac{\partial u_x}{\partial x} + C_{12}\frac{\partial u_y}{\partial y} + C_{11}\frac{\partial u_z}{\partial z}\right) \end{cases} \tag{3.9}$$

Each vibration mode $\omega$ is associated with a displacement field u ($u_x$, $u_y$, $u_z$) defined on the whole unitary cell. The elastic constants $C - ij$ are dependent on the position of the space coordinate of the periodic structure. These equations are implemented in the Comsol software by specifying the values of the elastic constants in each subdomain. The equations are rewritten as follows:

$$\left\{\begin{array}{l}
\nabla\cdot\left[\begin{pmatrix}C_{11}&0&0\\0&C_{44}&0\\0&0&C_{44}\end{pmatrix}\cdot\nabla u_x+\begin{pmatrix}0&C_{12}&0\\C_{44}&0&0\\0&0&0\end{pmatrix}\cdot\nabla u_y+\begin{pmatrix}0&0&C_{12}\\0&0&0\\C_{44}&0&0\end{pmatrix}\cdot\nabla u_z\right]\\
\nabla\cdot\left[\begin{pmatrix}0&C_{44}&0\\C_{12}&0&0\\0&0&0\end{pmatrix}\cdot\nabla u_x+\begin{pmatrix}C_{44}&0&0\\0&C_{11}&0\\0&0&C_{44}\end{pmatrix}\cdot\nabla u_y+\begin{pmatrix}0&0&0\\0&0&C_{12}\\0&C_{44}&0\end{pmatrix}\cdot\nabla u_z\right]\\
\nabla\cdot\left[\begin{pmatrix}C_{11}&0&0\\0&C_{44}&0\\0&0&C_{44}\end{pmatrix}\cdot\nabla u_x+\begin{pmatrix}0&C_{12}&0\\C_{44}&0&0\\0&0&0\end{pmatrix}\cdot\nabla u_y+\begin{pmatrix}0&0&C_{12}\\0&0&0\\C_{44}&0&0\end{pmatrix}\cdot\nabla u_z\right]
\end{array}\right\} \tag{3.10}$$

$$=-\rho\omega^2\begin{pmatrix}1&0&0\\0&1&0\\0&0&1\end{pmatrix}\cdot\begin{pmatrix}u_x\\u_y\\u_z\end{pmatrix}$$

### 3.3.3/ BOUNDARY CONDITIONS

Once the equations of motion were implemented, the Bloch Floquet boundary conditions (or straightforwardly, Floquet theory) to reflects the unbounded periodicity of the unit cell along the $X$ and $Y$ directions that were imposed on the two axes. By implementing the boundless surface condition, only certain wave modes can physically spread within the structure because of the heterogeneity of the featured geometric. The behavior of wave propagation can be illustrated by the dispersion curves as they summarise all of the system's oscillatory phenomena. Since the structure is assumed to be infinite in the $X$, $Y$ plane, the wave vector $\vec{k}$ will be such that: $\vec{k}$=($k_x$, $k_y$, 0). The mechanical displacements can thus be deduced for all the nodes situated at the limits of the cell with the Bloch-Floquet theorem equations:

$$\begin{aligned}
\vec{u}_{destination_1}(x+a,y,z)&=\vec{u}_{source_1}(x,y,z)e^{i(a,k_x)}\\
\vec{u}_{destination_2}(x,y+a,z)&=\vec{u}_{source_2}(x,y,z)e^{i(a,k_y)}
\end{aligned} \tag{3.11}$$

Where source surfaces and destinations are defined in Fig. 3.3

The rest of the free surfaces are set as free boundary conditions and translated according to the Cauchy postulate as follows:

$$\bar{\bar{T}}\cdot\vec{n}=\vec{0} \tag{3.12}$$

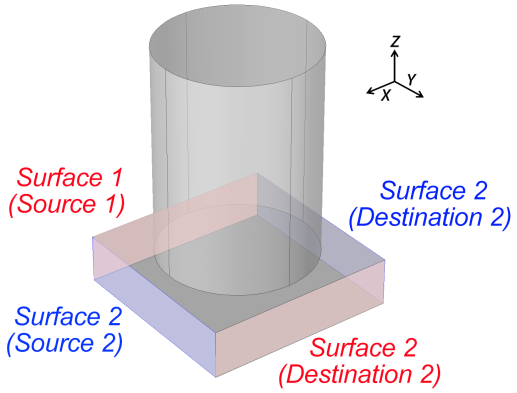


Figure 3.3: Periodic boundary conditions using Bloch Floquet theorem applied to the four lateral faces of the unit cell. Surface 1 and 2 (red surfaces) repeat the unit cell in Y-directions while surface 3 and 4 (blue surfaces) repeat the cell in X-directions.

where $\bar{\bar{T}}$ is the stress tensor and $\vec{n}$ $(n_x,\ n_y,\ n_z)$ is the vector normal to the area which results in:

$$\nabla \cdot \left[ \begin{pmatrix} C_{11} & 0 & 0 \\ 0 & C_{44} & 0 \\ 0 & 0 & C_{44} \end{pmatrix} \cdot \nabla u_x + \begin{pmatrix} 0 & C_{12} & 0 \\ C_{44} & 0 & 0 \\ 0 & 0 & 0 \end{pmatrix} \cdot \nabla u_y + \begin{pmatrix} 0 & 0 & C_{12} \\ 0 & 0 & 0 \\ C_{44} & 0 & 0 \end{pmatrix} \cdot \nabla u_z \right] \cdot \begin{pmatrix} n_x \\ n_y \\ n_z \end{pmatrix} = 0$$

$$\nabla \cdot \left[ \begin{pmatrix} 0 & C_{44} & 0 \\ C_{12} & 0 & 0 \\ 0 & 0 & 0 \end{pmatrix} \cdot \nabla u_x + \begin{pmatrix} C_{44} & 0 & 0 \\ 0 & C_{11} & 0 \\ 0 & 0 & C_{44} \end{pmatrix} \cdot \nabla u_y + \begin{pmatrix} 0 & 0 & 0 \\ 0 & 0 & C_{12} \\ 0 & C_{44} & 0 \end{pmatrix} \cdot \nabla u_z \right] \cdot \begin{pmatrix} n_x \\ n_y \\ n_z \end{pmatrix} = 0 \quad (3.13)$$

$$\nabla \cdot \left[ \begin{pmatrix} C_{11} & 0 & 0 \\ 0 & C_{44} & 0 \\ 0 & 0 & C_{44} \end{pmatrix} \cdot \nabla u_x + \begin{pmatrix} 0 & C_{12} & 0 \\ C_{44} & 0 & 0 \\ 0 & 0 & 0 \end{pmatrix} \cdot \nabla u_y + \begin{pmatrix} 0 & 0 & C_{12} \\ 0 & 0 & 0 \\ C_{44} & 0 & 0 \end{pmatrix} \cdot \nabla u_z \right] \cdot \begin{pmatrix} n_x \\ n_y \\ n_z \end{pmatrix} = 0$$

### 3.3.4/ MESHING AND CONVERGENCE

In the finite element method, the mesh is a geometrical discretization of the continuous domain into small subdomain elements connected at the nodal points. The solution for the problem is approximated at the individual finite element from one nodal point to another until a full model solution is analysed. In a COMSOL meshing setting, there are several preferences which can be selected, from the coarsest to the finest meshing. In this case,

the unit cells model was meshed by using a normal setting, which seems best adapted to the current structures. In general, the convergence of finite element calculations depends on the mesh adopted. With finer mesh control, the shape functions are more defined and there is a better approximation of the solution function. In order to ensure calculation accuracy for different cases, the size of the meshing should consider the character of the constituent material of the structure. For instance, if the elastic behavior of the cylinder is very soft as compared to the substrate, the variations in the displacement field are greater at the cylinder and a finer mesh must be imposed to the cylinder. However, a mesh which is too refined, if not optimised with computer capacity, will consume a lot of computational time to solve since meshing is the most memory-intensive step. The limits of the computer memory can quickly be consumed with more refine meshing. Considering this, a suitable choice of meshing size is important to reduce the computer memory requirements to interpolate the sought solution. In the current model, since a 3D metal printing technique is the aim for an end fabrication, both the cylinder and substrate are made from similar material: hence, there is no difference of elastic behavior for both domains and similar meshing dimension can be adopted for both pillars and substrate. In this study, a ratio of approximately 4 is chosen between the number of tetrahedral elements in the cylinder and substrate, as shown in Fig. 3.4.

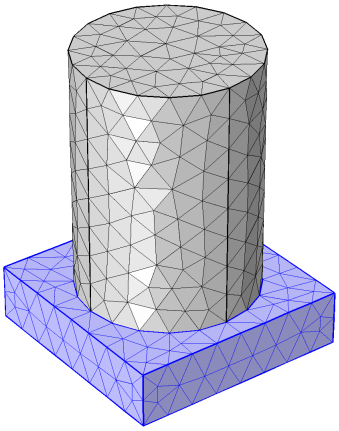

Figure 3.4: Unit cell under meshing stage

## 3.4/ SUPERCELL TECHNIQUES FOR WAVEGUIDE SYSTEM

In the previous discussion, the focus was given on the opening of prohibited bands gap for locally resonant PnC in slab configurations. With regard from a previous study, this section will discuss about the possibility to guide an elastic wave through the insertion of structural defects. When it comes to studying the waveguiding effect of a PnC structure, it is impossible to study the wave propagation in a defect area by using a unit cell. This is due to the Bloch theorem that assumes a perfect periodicity of a unit cell. To solve

this issue, the *supercell* technique can be used. The technique of "*supercell*" is used to study the periodic systems containing structural defects both in phononic and photonic crystals, such as cavities or waveguides. Different distance of linear guides will be studied by disturbing the crystal lattice, $a$ among the perfect row of pillars. Similar researches can be found in the literature review as described in chapter 3. For example the theoretical and experimental works by Khelif et al [66] and Wu et al [67] who have shown the possibility of guiding the elastic waves in a PnC through crystal defect. Inspired by numerous works on the guidance and the confinement of waves mentioned in previous chapter, the interest in this section is to demonstrate theoretically the guidance of elastic waveguiding via triple configurations of "*supercell*" to achieve demultiplexing functionality.

The creation of a waveguide in a PnC can generally be done by removing one or more rows of perfect inclusion which is normally equivalent to one lattice size (in the case of a single pillar removed) or several lattice sizes (in the case of several pillars removed). In this study, the waveguide will be constructed by a spacing denoted with $W_g$ between two neighboring rows of resonators, as illustrated in Fig. 3.5, with a size lesser than a crystal lattice, $a$. With the effect of a locally resonant PnC, the waveguide corridor can confine an incoming elastic waves with bigger wavelengths. To achieve the demultiplexing functionalities, three waveguides, $W_1$, $W_2$ and $W_3$, will be considered. By introducing the Bloch periodic conditions, the structure keeps its periodicity in the $X$ direction i.e., direction of the guide (refer to surface 1 and surface 2) while it becomes non-periodic in the $Y$ direction (refer to surface 3 and surface 4). The structure consists of defects to eliminate the periodicity of the PnC structure and gives the possibility for wave confinement. It also consists of several elementary cells on either side of the defect region (Figure 3.5).

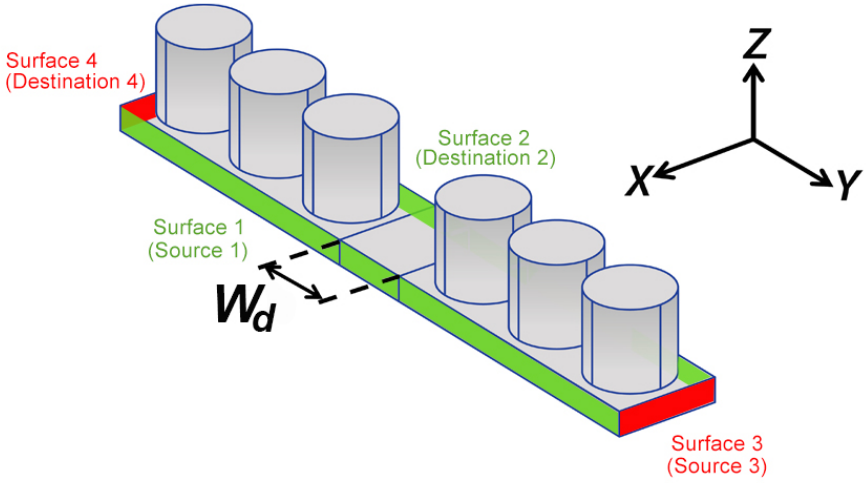


Figure 3.5: Supercell technique to calculate the dispersion curve for the waveguide structure

## 3.5/ CALCULATION OF TRANSMISSION SPECTRA

Dispersion curves make it possible to determine the conditions for the existence of band gaps. It allows us to specify the position, the width and the existing dispersion branches, regardless of their symmetry or polarization. It is therefore important to estimate the transmission of elastic waves through a finite structure as the next step of the study. Previously, an infinite periodicity for a two-dimensional square lattice unit cell along the directions $X$ and $Y$ has been considered. By assuming infinite periodicity, it is possible to plot the dispersion curves of the frequencies against the wave vector for a given incident wave according to Bloch-Floquet conditions. However, what about the finite structure with a limited number of unit cell periods? This section shall discuss the calculation of transmission coefficients to corroborate the existence and the accuracy of the dispersion curve. To better understand the effects of bandgaps and to closely study the qualitative behavior of transmission in bandwidths, the finite element method is used to calculate the transmission. The transmission model will be composed of a limited number of periods in a given direction of wave propagation and is vital for experimental comparison and validation in later parts of this study.

In the field of mechanical waves, transmission is the ability of the acoustic/elastic wave to pass through a periodic structure at a given frequency. The principle of calculation is to set up a source that generates acoustic/elastic waves at wide frequency bands and record the values of displacement fields as a function of time. The responses in reflection, as in transmission of structures, make it possible to provide additional information on the propagation of waves in a periodic structure. In fact, a complete extinction of the signal within the limits of the forbidden bands is expected. It should be noted that the calculation of coefficients of transmission through periodic finite dimensional structures requires the use of Perfectly Matched Layers (PML) to avoid any reflections on the edges of the simulation domain. The next section will describe this approach in detail.

### 3.5.1/ METHOD USING ABSORBING DOMAINS PML (PERFECTLY MATCHED LAYER)

When the structures to be calculated are not periodic but finished in one or two directions, it is necessary to define another kind of boundary conditions to avoid any reflections from the edges that will disrupt the structure. Several methods have been proposed to solve the reflection problem. The first approach is to modify the components of the fields at the edge of the zone at zero value and not apply the algorithm. However, a non-physical reflection then appears on the edges of the simulation domain and comes back to strongly disturb the structure. One of the most commonly used methods is the adapted absorbent layers known as PML (Perfectly Matched Layers).

The concept was proposed in 1994 by Bérenger [68] in order to alleviate the reflections of incident waves on structures. A perfectly matched layer is a medium that all incident propagation waves are transmitted and damped in the PML layer without any reflection to whatever angle or polarization of the incident wave. This method is used to study both homogeneous and heterogeneous viscoelastic and poroelastic media to limit the computational domain. For the structure considered in this thesis, the space is delimited into three zones: two homogeneous zones representing the PML layers are separated by the periodic structure and two free surfaces for the incident wave and wave detection medium. The first PML zone is located before the phononic crystal structure and free surface area that represents the source of wave excitation from which the wave emanates, as illustrated in Fig. 3.6.

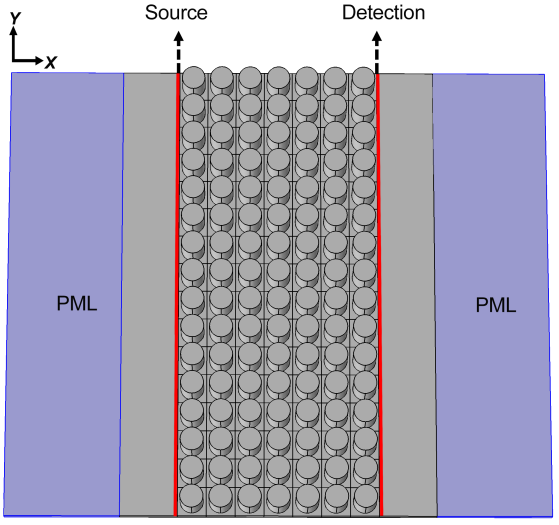


Figure 3.6: Finite dimension for the calculation of perfect PnC transmission coefficient

The second PML zone is located after the phononic periodic structure and free surface of a detection zone where the displacement fields are recorded as a function of time. Displacement fields obtained as a function of time and collected at the detector are converted into frequencies using Fourier transformations. The normalization of these transmission curves with the incident wave makes it possible to obtain the transmission coefficient as a function of frequency. The governing equation of a PML is given by :

$$\frac{1}{\gamma_j r} \cdot \frac{\partial T_{ij}}{\partial x_{(}j)} = \rho\omega^2 u_i \tag{3.14}$$

Where $\rho$ is the density, $\omega$ is the angular frequency, $T_{ij}$ is the stress tensor, $u_i$ is the displacement field, $x_j$ ($x_1$ = x, $x_2$ = y and $x_3$ = z) are the Cartesian coordinates and $\gamma_j(r)$ is the artificial damping function along the $x_j$ axes in a given position $r$ within the PML layer. There are different ways to apply PML. In particular, the stretching the coordinate system is considered in our calculation. For example if a PML is designed to absorb

waves propagating in the X direction, the following transformation is included in the wave equation. Anywhere a derivative x appears in the wave equation, it is replaced by :

$$\partial\bar{x} = \frac{i\omega}{i\omega + d_x}\partial x = \frac{1}{S_x}\partial x$$
$$S_x = \frac{i\omega + d_x}{i\omega} = 1 + \frac{dx}{i\omega} \tag{3.15}$$

With the damping profile:

$d_x$=0 ; for outside the PML and
$d_x$ >0 ; for 0 Inside the PML

## 3.6/ RESULT AND DISCUSSION

### 3.6.1/ UNIT CELL COMPLETE BAND GAP

In this section, the result for complete band gap based on the unit cell as mentioned earlier, will be presented. The model allows under certain conditions, the opening of kHz frequencies gap. In this case no explicit external source is required, but Floquet's conditions will assume the existence of incident plane wave as represented by the wave vector, $k$. Since the structure is based on the 2D square lattice periodic arrangement, the computation of dispersion curve can be minimised to a unit cell. The calculation of the dispersion curve can be delimited to the main axes of symmetry of the first irreducible Brillouin zone as shown in Fig. 3.7.

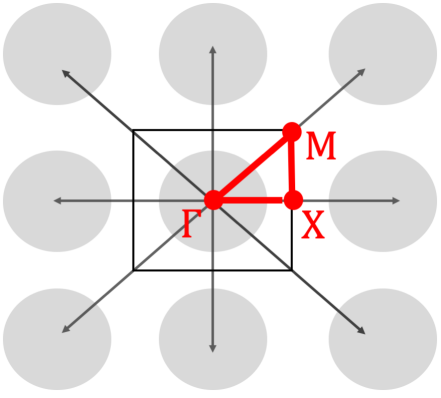


Figure 3.7: Brillouin zones and irreducible Brillouin zone for a square lattice considered in simulation

Due to the high symmetry of the first Brillouin zone it is sufficient to calculate only the first irreducible Brillouin zone (triangle ΓXM) to obtain the band of frequencies corresponding

to waves propagating in all directions, which is the triangle of Figure 3.7. This limit can cover the directions of displacement s of the waves of $\theta \in (0^o, 45^o)$; $\theta$ is the angle formed $\Gamma$X and $\Gamma$M [69]. The frequency shift of the system is obtained by solving the eigenfrequencies at different values of Bloch wave vector $k$ expressed in the form ($k_x$, $k_y$). The wave vector represents the reciprocal space, the vibration and the different directions of incident wave propagation. For example, $k_x$ varies between (0, $\pi$/a) in the direction $\Gamma$X ($k_y$ = 0); $k_y$ varies between (0, $\pi$/a) in the direction XM ($k_x$ = $\pi$/a) and both $k_x$, $k_y$ varies between ($\pi$ / a, 0) in the direction M$\Gamma$.

Considering the three directions of the irreducible Brillouin zone as depicted in Fig. 3.7, Fig. 3.8 illustrates the results for dispersion curve. For the unit cell geometry described before, two partial band gap at frequency between 382 to 405 kHz and 472 to 485 kHz can be observed, while the complete band gap exists at frequency between 272 kHz to 347 kHz as shown in Fig. 3.8. The blue colored zone corresponds to an absolute forbidden band with relative widths of 30 $\%$ (knowing that the relative width of a forbidden band is equal to the ratio of the width of the band to the mean or central frequency of the band ($\Delta f$ / $f_m$).) where no wave propagation is possible. In other words, whatever the direction of propagation in the plane, the modes of vibration $U_x$ or $U_y$, $U_z$ cannot propagate within the region.

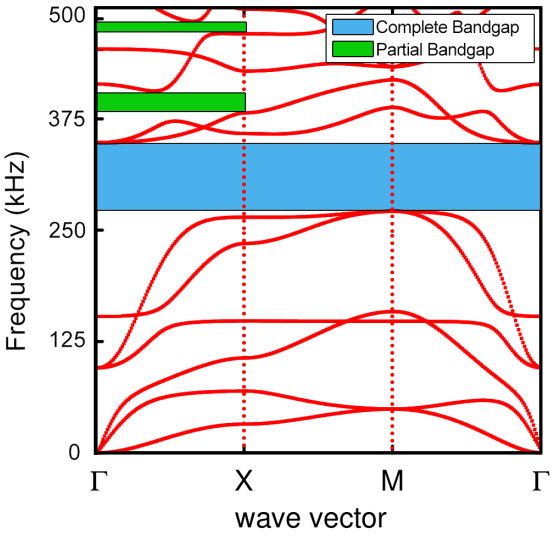


Figure 3.8: Dispersion curves frequency against the wave vector, $k$ with two partial band gap at frequency between 382 to 405 kHz and 472 to 485 kHz while the complete band gap exists at frequency between 272 kHz to 347 kHz

In the vicinity of the point $\Gamma$X of the Brillouin zone, the dispersion curve in the direction $\Gamma$X presents three branches which are identified as antisymmetric (A0), shear horizontal (SH) and symmetric (S0) to represent the Lamb mode. The mode is very sensitive to the parameters of slab thickness, $h$ and pillar height, $h_p$. The study of these branches of responsive behavior according to the height $h_p$ of the pillar or the thickness of the slab, $h$

makes it possible to choose the right set of parameters ($h$, $h_p$) which controls the formation of the gap frequency.

As illustrated in Fig. 3.9(a), an increase in the thickness $h$ causes a general shift of all the dispersion branches towards the high frequencies and closes the gap. Depending on the isotropic or anisotropic constituent of unit cell, the effect of the geometric parameter however is varied. In one study, the band gap opening of a piezoelectric inclusion on top of epoxy matrix is depending on the slab thickness. In addition, the pillar high has a contrast effect to close the band gap instead of opening it. As can be observed in Fig. 3.9(b), a greater height $h_p$ of the pillar moves all the branches towards the low frequencies due to effect of local resonance. With the higher mass of pillar, the effect of local resonance is more obvious and thus lower the frequency gap. This low-frequency resonance can be interpreted as an oscillation, in which the heavy mass is given by the pillar and the soft spring is provided by the slab thickness. Thus, from the observation, the parameters $h$ and $h_p$ are the two key parameters that dictates the opening or closing of the band gap. To obtain the widest possible band gap, every case is unique and it is necessary to choose carefully the right pair of values $h$ and $h_p$.

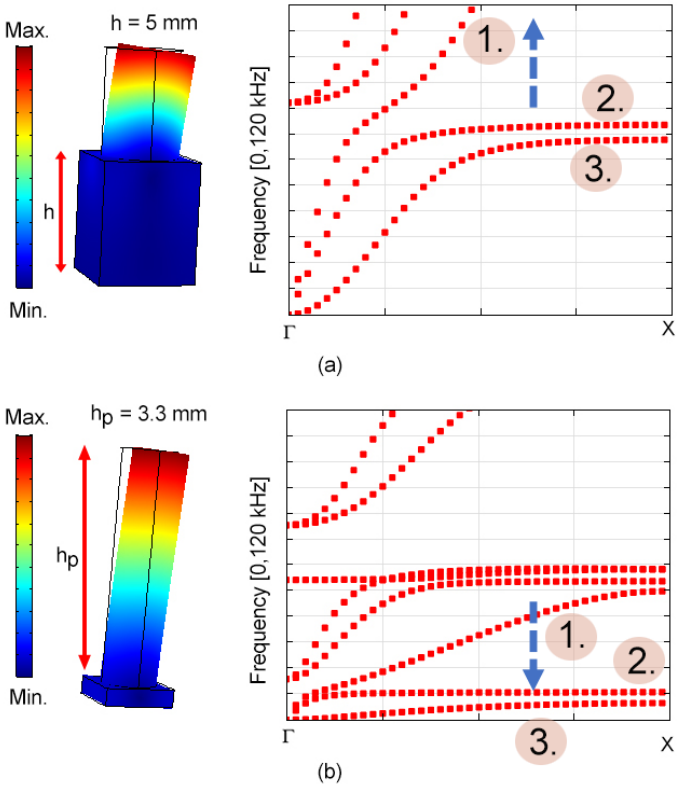


Figure 3.9: Dispersion curve for (a) slab thickness $h$=5mm and $h_p$ = 1.1 mm (b) for a slab height $h$ = 1 mm.

#### 3.6.1.1/ EFFECT OF PILLAR HEIGHT, $h_p$ AND SLAB THICKNESS, $h$ ON THE PROHIBITED BAND

In this section the aim is to study the geometric parameters that influence the opening of band gap. In order to highlight the relationships between the geometric parameters and the band gap opening, a "gap mapping" operation of sweeping the ranges of geometric parameters in relation to the frequency were simulated. In general, the gap mapping study is particularly useful to identify a specific geometric parameter for the widest band gap opening possible. With maximum band gap size, more waveguides channels with more frequency filtering capabilities can be inserted. The following procedure should be followed for the gap mapping studies :

- The geometric parameters are varied within a certain range of values and acts as a scaling factor for the geometric dimensions and the frequencies since both are related in one way to another.
- In all the stages, the lattice constant, $a$ (the periodicity of the pillars) is kept constant and is taken equal to 4 mm.
- The gap mapping operation is composed of four stages in which the modification of the geometric parameters is studied one by one. For example, in the first step, the pillar radius, $r$ and the slab thickness, $h$ was kept constant and only the height of pillar, $h_p$ was modified. In the second step, only $h$ was modified while $h_p$ and $r$ were kept constant; in the third step, parameters $h$, $h_p$ were kept as constant and only $r$ varies.

To illustrate this operation, Fig. 3.10 represents the gap maps of this first preliminary step represented by the variation of frequencies according to the $h_p$ while keeping slab thickness, $h$ and radius, $r$ constant. To study the effect of pillar height $h_p$, the relative dimension were varied between 0.4 mm and 6 mm while the wave vector $k$ varied in the direction $\Gamma X$. The first developing band gap was ignored; instead, the focus should be on the second since the widest development can be noted on the second band gap. The result shows the greater the height of the resonators, the more the forbidden bands move towards the low frequencies with a slight improvement in their width. This is explained by the fact that the increasing of resonators height increases their mass; the latter being responsible for the existence of prohibited bands at low frequencies, as several researchers have pointed out [70]. Even though the trend shows a consistent decreasing frequencies, the average band gap width is relatively similar with almost no noticeable increment for the band gap width (in particular between 4 mm to 5 mm). Thus, in this case the reasonable value to choose is equivalent to $h_p$=4.4 mm.

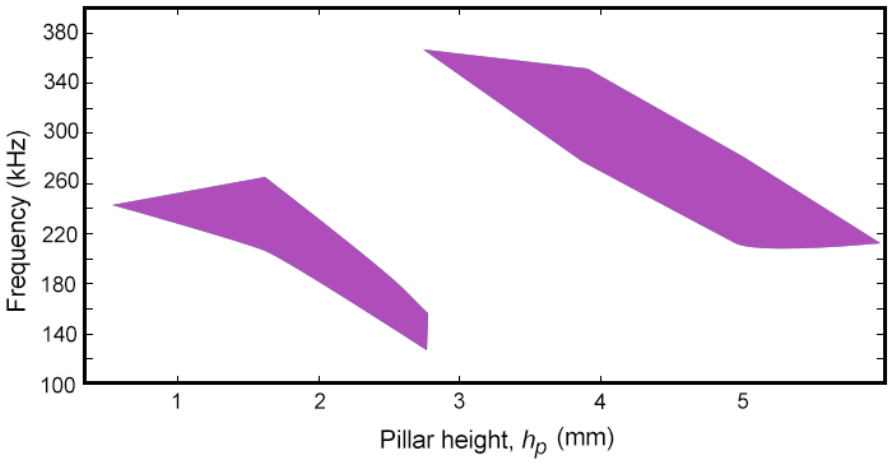


Figure 3.10: Evolution of the band gaps as a function pillar height, $h_p$

#### 3.6.1.2/ EFFECT OF SLAB THICKNESS ON THE PROHIBITED BAND

Referring to the gap mapping in the previous preliminary step, which determined the pillar height dimensions to obtain the forbidden bands, the purpose of this is to preserve the essential character of local resonance. Fig. 3.11 illustrates the effect of slab thickness, $h$ on the band gap opening. The result suggests a similar trend with pillar height gap mapping. With increasing slab thickness, the band gap frequency tends to decrease. The widest band gap can be obtained with 0.5 mm slab thickness. However, this is not recommended since during the fabrication process, the thin substrate will not be able to stand an additive manufacturing processing stage. The minimum suggestion for the slab thickness should be 1 mm.

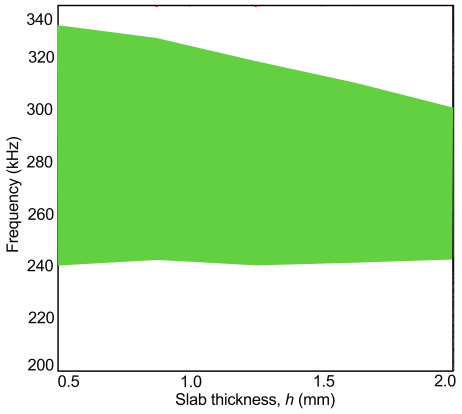


Figure 3.11: Evolution of the band gaps as a function slab thickness, $h$

#### 3.6.1.3/ EFFECT OF PILLAR RADIUS ON THE PROHIBITED BAND

Figure 3.12 illustrates the evolution of the band gap as a function of pillar radius. With the increase of radius, $r$ notices an increasing trend for band gap frequency, but at point $r$=2.5 mm the trend decreases with consistent band gap width. The band gap sizes reached its peaks and the maximum width within the ranges 2 mm to 2.5 mm. However, the radius, $r$ sweep beyond 2 mm should be ignored as this value is the threshold limit for the crystal lattice, $a$= 4 mm. Guided to find the widest possible band gap, observe at point $r$=1.6 where a good size of the band gap can be noted. At the end of the preliminary gap mapping operation, the following geometric parameters will be chosen: pillar height, $h_p$=1.1 mm, slab thickness, $h$=1 mm, radius of pillar, $r$=1.6 mm.

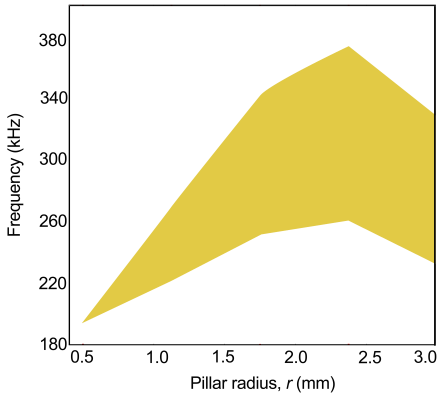


Figure 3.12: Evolution of the band gaps as a function pillar radius, $r$

### 3.6.2/ BAND STRUCTURE OF THE WAVEGUIDE

Previously, a complete band gap diagram based on perfect periodic structure was found between 272 to 347 kHz. The next step of study is to introduce the passing band inside the band gap region through a "*supercell*" model for frequency filtering. The technique has been used to study the waveguiding in both phononic and photonic crystal researches to simulate the waveguide dispersion diagram and its respective confinement. In the case of PnC domain, several relevant works of sigalas [3] and Abdelkrim et al., [7] can be referred. Fig. 3.13 shows a comparison between the waveguide $W_g$ = 1.2 mm with a flawless "*supercell*". It is noticed that the dispersion curve for waveguide supercell maintained a similar position and range of frequency band gap with the unit cell. Secondly, the presence of guided mode can be noticed in the vicinity of two frequencies scale which was caused by the linear defect introduced in the supercell structure. The first dispersion is a single uninterrupted guided mode between 300 to 325 kHz. Thirdly, the presence of two other intercepted localise mode were close to the upper limit of band gap region between frequency 340 to 375 kHz. The appearance of several dispersion branches, even in the

case of a single-mode $W_g$ guide, is explained by the periodic boundary conditions by the walls of the phononic waveguide. The interconnected dispersion however will not be the main concern since the best filtering exist on single uninterrupted mode between 300 to 325 kHz. The choice of single uninterrupted mode is important to avoid any interaction between the dispersion branches that can minimize the effectiveness of waveguiding and filtering purpose.

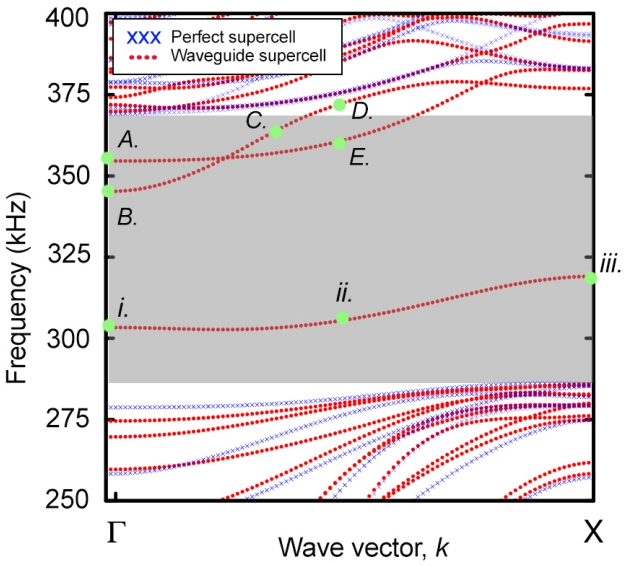


Figure 3.13: Dispersion curves of frequency against the wave vector, $k$. The points A-E and i-iii indicate the selected position of wave vector, $k$ and frequencies for the displacement profile studies

To study in more detail the nature of the guided mode of in Fig. 3.13, an analysis for the displacement fields distribution of waveguide supercell were simulated in Fig. 3.14. The displacement field vector $u = \sqrt{(U_x)^2 + \left(U_y\right)^2 + (U_z)^2}$ were calculated at points (a)-(e) in Fig. 3.14 for the criss-crossing guided mode and (i)-(iii) for single mode in Fig. 3.15. In the beginning, the discussion should focus on the localised mode close to the band gap upper boundary as marked with points (a)-(e). By analyzing the distribution of the mode displacement field in Fig. 3.14, notice a wave confinement that corresponds to the linear spacing introduced in the perfect crystal structure. The elastic energy is clearly confined within the defect area with energy leakage into the resonators next to to the guide. It is noticed that the further away the localised mode from the band gap limit, the degree of wave confinement will be increased accordingly. For instance the comparison between displacement A-B and C-D where the better wave entrapment for point B compared to A can be observed as a red displacement signifying better wave confinement.

Secondly, the degree of penetration for point A has to reach the second pillar rows adjacent to the guide channel compared to point B with only the first row of pillar affected.

The leakage is due to the eigenvalue and eigenmode of the wave propagating inside the waveguide region which is in coherence with neighboring pillar's eigenvalue. Two factors are important; (a) higher displacement spectrum intensity within the waveguide and (b) low degree of wave penetration to resonator area represent the better wave confinement for the point B compared to A due to its farther distance from the band gap upper limit. The farther the passing band from band gap boundaries, the less chances it has to interact with other dispersion branches that can compromise the degree of the wave confinement.

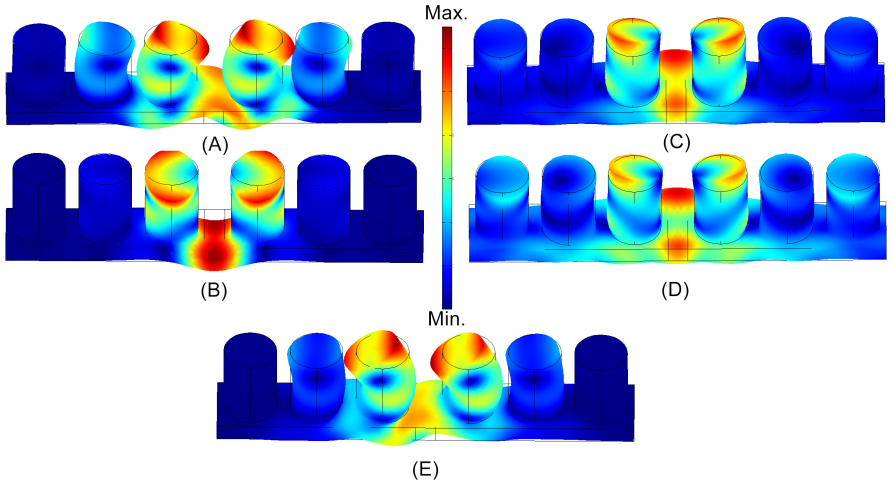


Figure 3.14: Displacement profile for the criss-crossing dispersion waveguides in Fig. 3.13 between 320-360 kHz at various wave vector, $k$ (a)$f_a$=337 kHz(b)$f_b$=327 kHz (c)$f_c$=348 kHz (d)$f_d$=352 kHz (e)$f_e$=340 kHz

Similar trend can be observed between points $c$ and $d$. Point $d$ has leakage that reaches the whole rows of supercell models. This is due to the fact point $d$ is located outside the prohibited band and have more close interaction with other dispersion branches. It shows the guided mode becomes less confined when moved away from the prohibited band. If the point move farther away from the latter, the confinement will disappears completely and the wave propagates throughout the "$supercell$". But as the point goes 'deeper' and further from the band gap limit, the leakage to the neigbhoring pillars are decreases as can be seen in the displacement field of point (c) and (e). To summarise, in any points of dispersive curve for the scenario of (a) criss-crossing branches and (b) branches close to band gap boundaries, it has the leakage phenomena that signifies the poor ability to trap the wave within the waveguide channel. For this reason, the main focus on the dispersion curve should have the following characteristics (a) Single and uninterrupted localised mode (b) fair distance from the band gap limit. Fortunately, as Fig. 3.13 suggests, such dispersion do exist in the range of frequencies between 275 to 305 kHz.

In Fig. 3.15, the disturbance of PnC crystal lattice effectively allows an incoming wave to be trapped in a guide region with a dimension less than the wavelength of the incident signal. In particular, the width of the guide, $W_g$ is equivalent to 1.2 mm, for a wavelength

of the signal of around 1.8 mm. Previously, Larabi et al., have demonstrated for the first time, the capability of a low frequency guidance to trap the incident wavelength is 10 times greater than the lattice parameter.

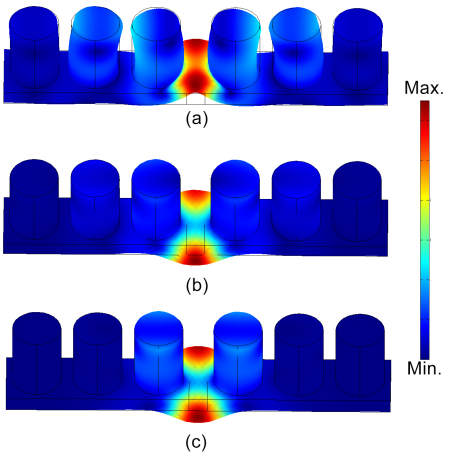


Figure 3.15: Displacement profile for the single dispersion waveguides in Fig. 3.13 between 275-310 kHz at various wave vector, $k$ (a)$f_i$=337 kHz(b)$f_{ii}$=327 kHz (iii)$f_c$=348 kHz

In order to highlight the vibratory nature of the guided mode and to complete the discussion, Fig. 3.16 shows the three components of the displacement field $U_x$, $U_y$ and $U_z$ for three points wave vector (i), (ii) and (iii). Such modal distribution can give better insight to check for the effective waveguide within the corridor as a function of the polarisation.

Fig. 3.16 illustrates the guided mode has a dominant field component $U_z$ with inconsistent and variation distribution of displacement field and are recorded for the components $U_x$ and $U_y$. The mode shows absolute wave confinement with almost no energy leakage in the neighboring pillars through out all points (i)-(iii). This shows the presence for the out of plane mode which corresponds to the asymmetric mode A0 of the Lamb waves. Another reason for this significance $U_z$ polarisation is due to the direction of pillar in the $U_z$ thus the better confinement in this direction within the region of waveguide. It should be noted, the confinement degree for the mode $U_x$ and $U_y$ are not consistent throughout the points. For instance, for point i and point ii, the displacement $U_x$ has better energy accumulation within the waveguide compared to $U_y$. But the mode has variation in terms of energy leakage depending on the position within the wave vector $\Gamma$X. For example, at point $\Gamma$ the wave entrapment shows a total wave confinement within the corridor, while at point ii the leakage can be noted affecting two rows of pillar and at point iii only one row of pillar is affected. Hence the side of $u_y$ it hence shows no energy confinement at all but disperse in pillars rows.

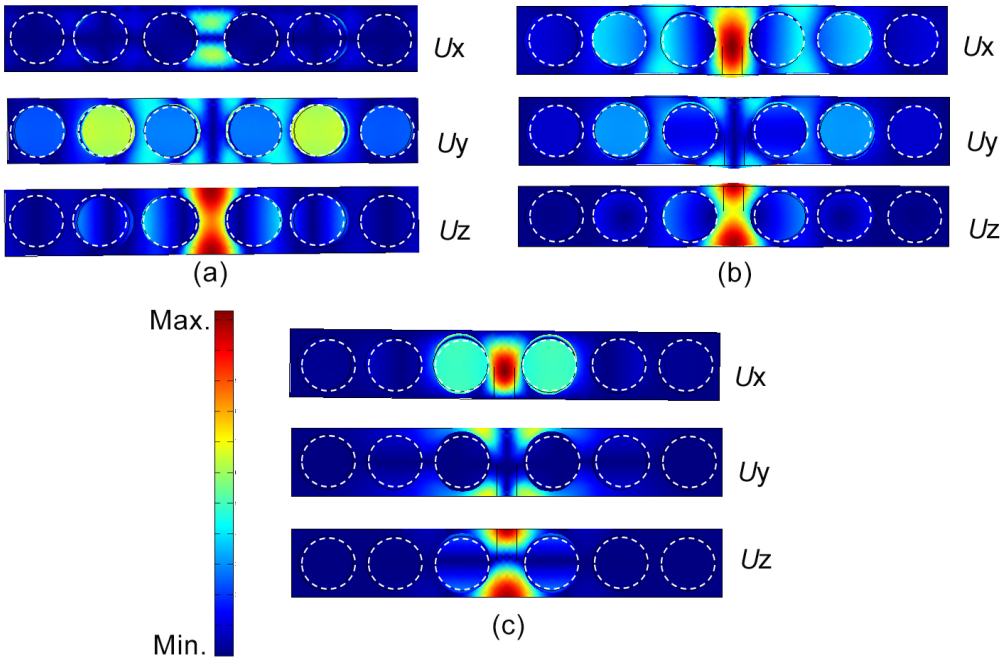


Figure 3.16: Components of the displacement field $U_x$, $U_y$ and $U_z$ for the three points (i), (ii) and (iii) in Fig. 3.13

Previously the defect introduced into perfect crystal can raise the possibility to confine the incident waves. Next, the behavior of dispersion curve as a function of waveguide's width for potential demultiplexing application were explored. The band calculations were performed for the following $W_g$ values: 0.88 mm (Blue curve), 1.2 mm (Black curve) and 1.52 mm (red curve) as shown in Fig. 3.17. The selection of these $W_g$ distances are due to their fair separation among the dispersion curve to limit their interaction for the best wave confinement purpose. With the filtering and demultiplexing in mind, the criss-crossing dispersion curve that is located in the upper limit of the band gap should be ignored and instead the single mode that can be seen clearly exists for each $W_g$ values should be the main focus.

One of the important behavior in Fig. 3.17 is the position and frequency of the localised mode directly depending on the $W_g$ opening. As the $W_g$ distance increased gradually, their dispersion curve slowly moves towards lower limit of the band gap. Both the single localised mode and the criss-crossing mode of each $W_g$ demonstrate the similar behavior. Due to the inverse relationship between the frequency, $f$ and mass, $m$, an increasing distance of waveguide (thus increasing in mass) results in lower frequency. In addition, the displacement distribution of the fault mode for a fixed value of the wave vector, $k$ was also presented. The objective is to explore the relationship of the waveguide size widening as a function of wave confinement.

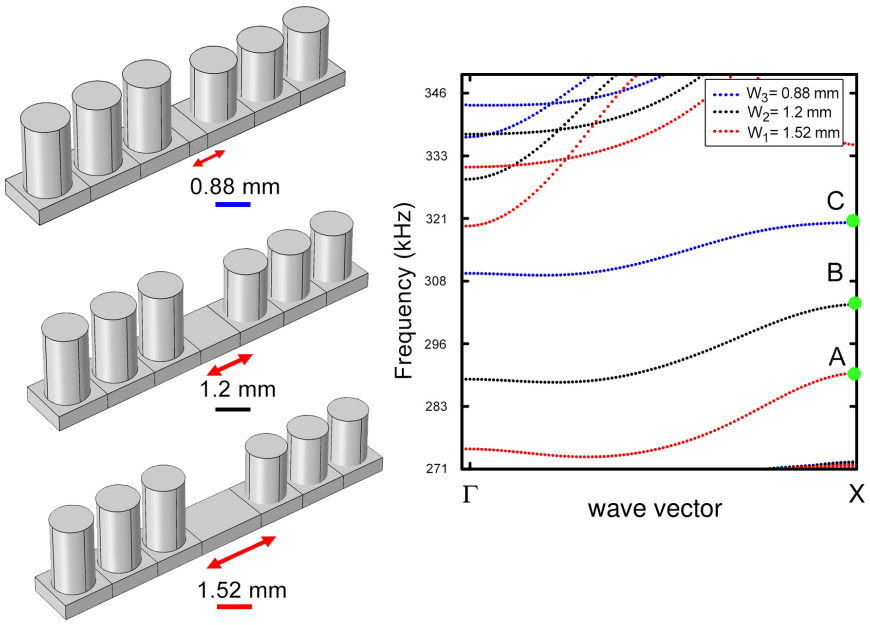


Figure 3.17: (Left) three selected waveguide *supercell* model, $W_g$=0.88 mm, 1.2 mm, 1.52 mm with their respective dispersion curve on right

Figure 3.18 shows the $U_z$ displacement mode A, B, C in Fig. 3.17 for each $W_g$= values: 0.88 mm, 1.2 mm and 1.52 mm. We note a significant wave confinement for each waveguide size. However, with increasing $W_g$ values, the degree of wave confinement is slightly decreased with negligible leakage into the neighboring pillars. In particular, the wave is perfectly confined for the smallest waveguide distance, $W_g$ = 0.88 mm with zero wave penetration into the rest of the structure. With $W_g$=1.52 mm, the leakage only affects the first pillar next to the waveguide channel leaving the second pillar unaffected. Nevertheless, with the small leakage, it doesn't tolerate with the good degree of wave confinement as we can observe a maximum displacement still trapped within the vicinity of the waveguide area.

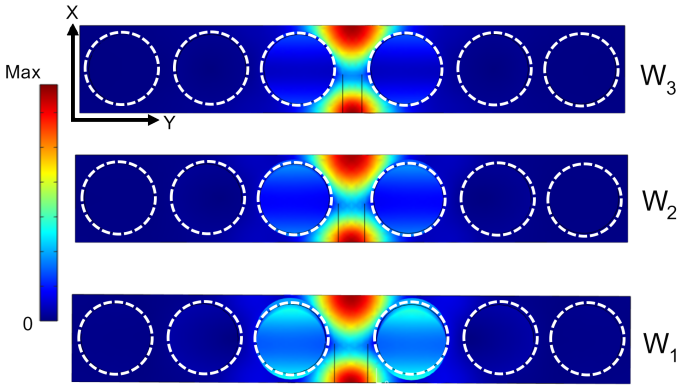


Figure 3.18: Displacement profile for $U_z$ direction at points $a$, $b$ and $c$ in Fig. 3.17

### 3.6.3/ TRANSMISSION COEFFICIENT VERSUS FREQUENCY

#### 3.6.3.1/ COMPLETE BAND GAP TRANSMISSION SPECTRUM

In this section the effect of different source detection on the transmission spectrum of the band gap were investigated. In normal practise the line detection has been used to measure the incoming wave. But what is the effect of other detection source to detect the incoming wave? This is the question that should be addressed. In the experimental stage consisting of multi-channel waveguides, the source of detection located at the end of filtering lines is not possible to measure the effect of the band gap due to the transmission of incoming waves within the waveguides channel. Thus, an alternative scanning area is necessary to be studied. Two alternative areas of scanning detection were chosen, (a) surface detection located at 7 pillars away from the excitation source (refer to blue region in Fig. 3.19) (b) scanning point detection located in the vicinity of perfect crystal structure as marked by red-dotted in Fig. 3.19. The transmission spectrum of these two scanning detections area with the line detection spectrum will be compared.

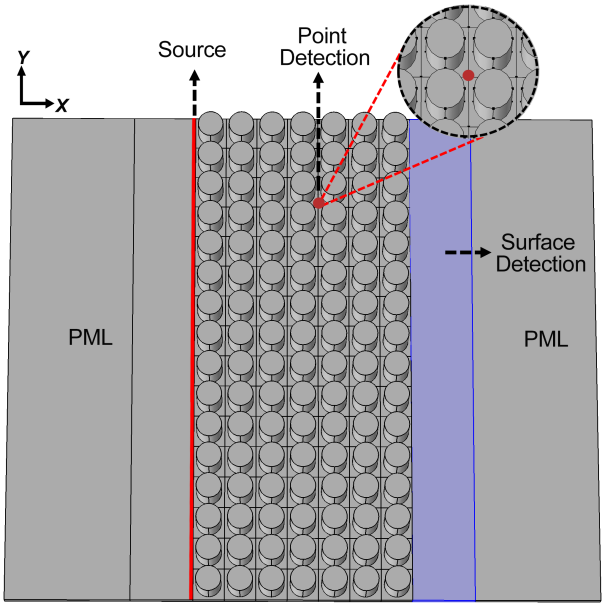


Figure 3.19: Detection source alternative for line detection at point detection (red-dotted marked) in the vicinity of phononic crystal struture and surface detection source as marked by blue region

Fig. 3.20 shows transmission spectrum comparison for the three detection sources for line (green), surface (blue) and point (red) detection source. The transmission curve in Fig. 3.20, confirms the presence of the gap as observed in dispersion curve. The three transmission shows a slight variation in term of attenuation transmission but shows similar frequency for band gap ranges. The most related and close transmission pattern

can be observed for green and blue line transmission which respectively represent line and surface detection. The results are understandable since both detection are located in the same position of seven pillars away from the incident wave. Thus, it's not difficult to understand how the result shows perfectly-matched transmission for both attenuation degree and range of frequency. The point detection as indicated by red lines, shows different degree of transmission and pattern due to its different nature of detection area. However, the variation is negligible because the band gap frequency are comparable with the rest of detection sources. In the experimental study, the point detection was chosen as comparison with the experimental result due to its position that is separated from the waveguide corridor.

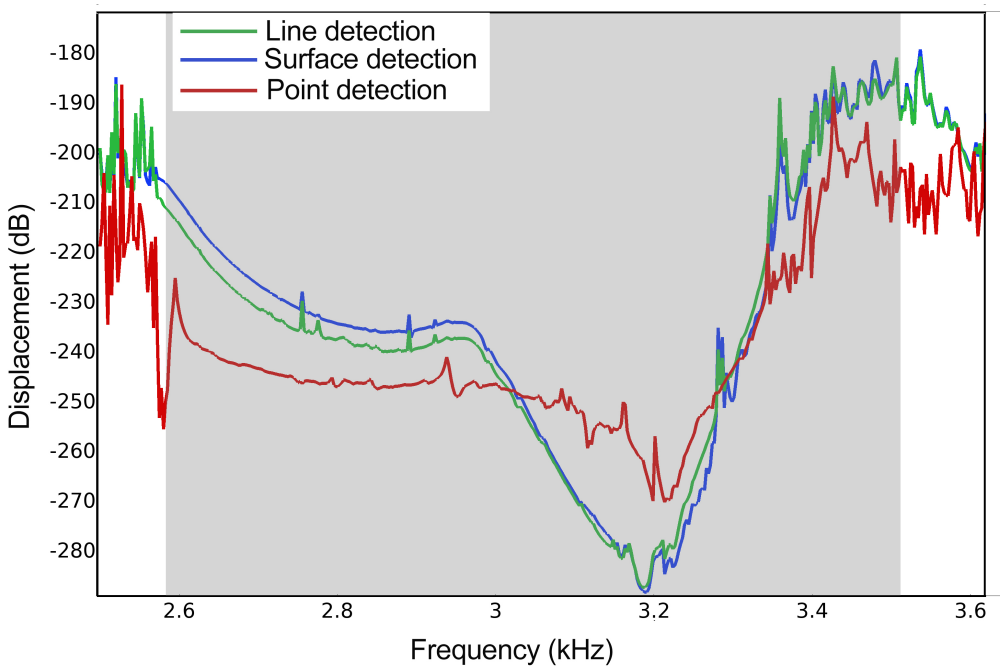


Figure 3.20: Transmission spectrum comparison between the line, point and surface source shows a good agreement for the band gap attenuation with respect to each other

### 3.6.3.2/ TRANSMISSION COEFFICIENT FOR SINGLE WAVEGUIDE

In this section the wave transmission with the PnC waveguide is illustrated in Fig. 3.21. The model is based on a unit cell which multiplies accordingly to consist of a row of seven cylinders of finite dimension along $U_x$, including the entry and exit space. The unit cells are composed of the cylindrical pillar deposited on the slab structures as illustrated in Fig. 3.2. In the case of guides, a super cell with a width of eight cells according to $U_y$ in order to decouple the interactions between several guides in later stages of study were considered. To avoid any wave reflection in the limit of the structure, the Perfectly Matched Layer (PML) in similar location as for the case of band gap calculation described in the

previous section were imposed on the model. A source of excitation was put in place at the entry of the guide waveform as a force applied along a line perpendicular to the guide (red line in Fig. 3.21). From this source, the wave can be generated before being completely absorbed by the PML domain. The transmission coefficient was obtained by recording the values of the displacement field at the level of the detection line.

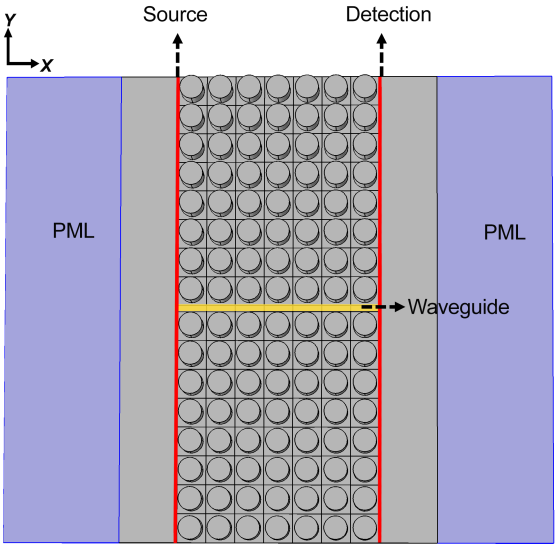


Figure 3.21: Finite waveguide model for $W_g$=1.2 mm equipped with source of excitation and detection to calculate the transmission coefficient

Figure 3.22 illustrates the results of the transmission coefficient for a waveguide, $W_g$=1.2 mm. Notice the transmission coefficient with a forbidden band gap on the frequency range 260-350 kHz as marked by the grey region. The result agrees perfectly with the previous numerical simulation as mentioned in band gap transmission (Fig. 3.20). In the vicinity of forbidden band gap, Fig. 3.21 records the appearance of local transmission between 300 to 320 kHz signifying the waveguide transmission due to structural defect. Indeed, no transmission of the elastic wave is recorded at the level of other ranges of frequencies except within the 300 to 320 kHz. The result shows the success of fault mode to incite non-attenuation of elastic wave within the specific ranges of frequencies signifying frequency filtering.

To appreciate the result further, the displacement diagram on several frequencies transmission as marked by the green circle in Fig.3.22 were examined in Fig. 3.23. The study is important to understand the behavior of elastic wave propagation within waveguide model. In general two important behaviors should be expected. Since the transmission graph illustrates two intrinsic transmitting and attenuation phenomena, a suppressed and transmitted waves displacement profile in the presence of particular frequencies should be observed.

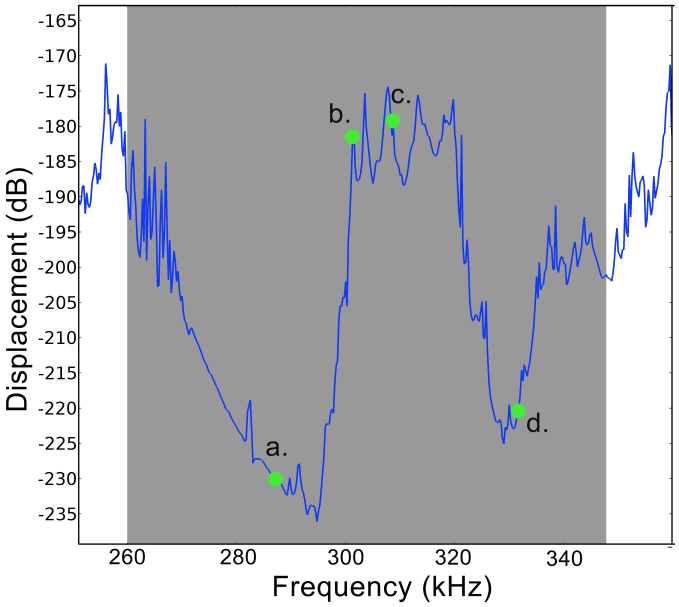


Figure 3.22: Transmission coefficient for the finite model waveguide, $W$=01.2 mm in Fig. 3.21. The transmission demonstrates the transmitted frequency equivalent to 300-320 kHz as predicted by the dispersion curve in Fig.3.8. Figure also shows several green marks to indicate the points for the displacement profile study

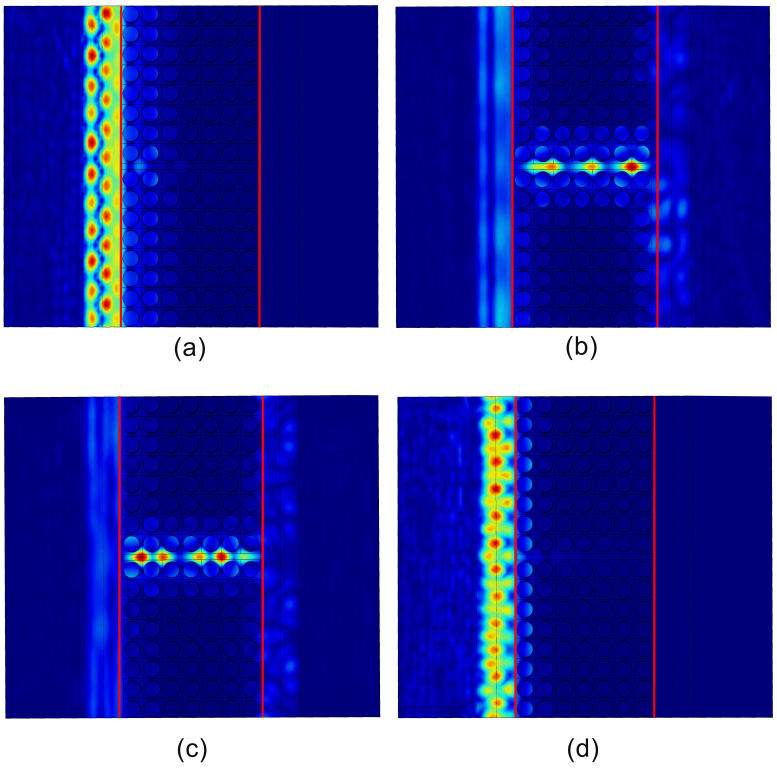


Figure 3.23: Displacement profile study for a green dotted frequency in Fig. 3.22 at frequency (a)287 kHz(b)303 kHz (c)312 kHz (d)333 kHz

Take for example in Fig. 3.23 (a) at frequency 287 kHz where the wave is totally blocked by the PnC boundaries eventhough with the presence of the opening channel that can open for possible wave transmission. On the other hand, as the transmitting frequencies reached within the waveguide ranges, the following phenomenas can be noticed (b) a wave is finally travelling along the defect channels. At the other transmitting frequencies (c) once again, the elastic wave is confined and guided along the similar guide but surely within the different frequencies. Beyond the transmitting frequencies, take for example point (d) the wave is blocked again from channelling through the structure.

#### 3.6.3.3/ TRANSMISSION COEFFICIENT FOR THREE-WAVEGUIDES CHANNELS

To calculate the transmission coefficient for the demultiplexing application, a building model consisting of three waveguides $W_1$, $W_2$, and $W_3$ which respectively represent waveguide 1.52 mm, 1.2 mm and 0.88 mm as shown in Fig. 3.24, was considered. To avoid any wave interaction among the waveguides' corridor, each waveguide was separated by 7 pillars in y-axis directions. A line source of excitation and detection similar to calculate the band gap transmission was used. The transmission ratio between the detection and excitation lines were calculated and the use of PML to absorb the incoming wave to avoid the wave reflection were used in two sections area i.e., in the excitation wave side and detection sides.

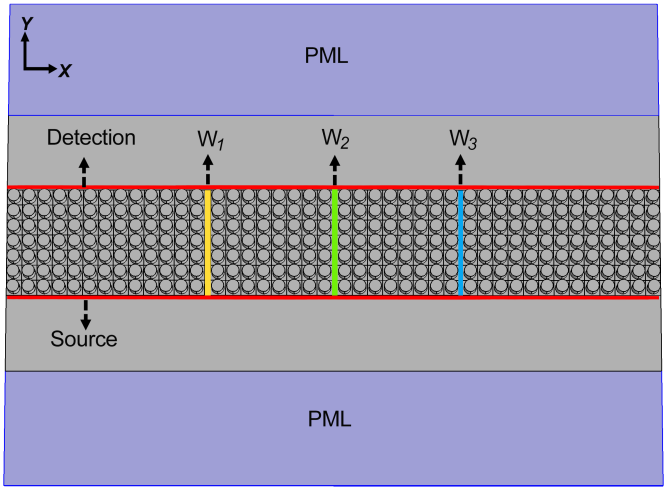


Figure 3.24: Finite demultiplexing system consists of three distinct waveguides corridor with $W_1$=1.52 mm, $W_2$=1.2 mm and $W_3$=0.88 mm.

Fig. 3.25 shows the transmission spectrum of the three channels waveguide which respectively marked with red for $W_1$, orange for $W_2$, and blue for $W_3$. The grey region indicates the area where the complete band gap exists. From this figure, notice that three distinct frequencies alternately increase and decrease in the band gap region. For

instance, the red transmission which represents the widest corridor size $W_1$=1.52 mm shows a transmission peak between 270 to 290 kHz. Beyond the frequency 290 kHz, the transmission can be noted to decrease and attenuate through the rest of the band gap frequency ranges. Meanwhile, as the $W_1$ transmission decreases at the frequency 290 kHz, another peak transmission that does not appear within range of 270 to 290 kHz rises signifying the transmission for the second waveguides corridor that belong to $W_2$. The $W_2$ can be seen as transmission between 285 to 305 kHz with no other transmission within these ranges except with slight criss-crossing frequency that belongs to $W_1$ equivalent to 285 to 290 kHz. Beyond the frequency 305 kHz the noticeable third transmission with blue line increases while the $W_2$ transmission decreases. The frequency transmission that belongs to third corridor $W_3$, falls in the frequency between 305 to 325 kHz. Similar wave filtering phenomena can be seen in the third case where there is no obvious transmission from other waveguides.

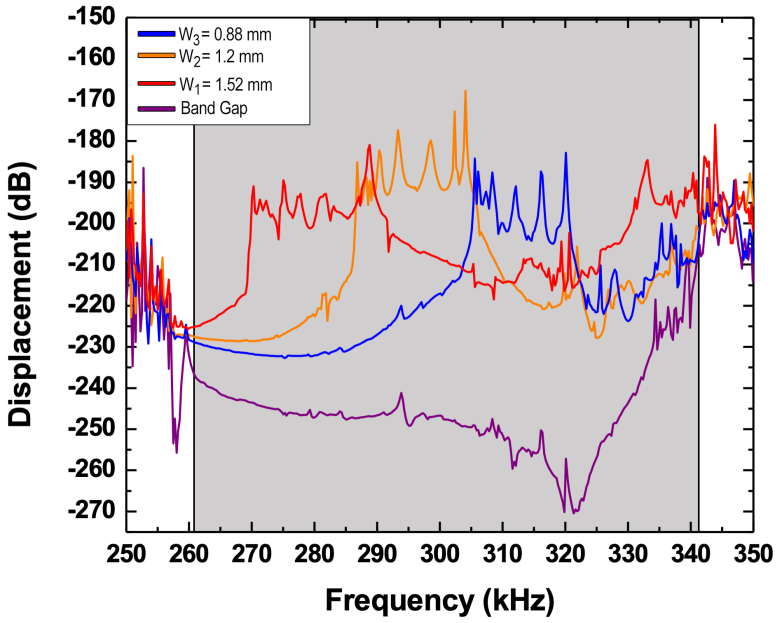


Figure 3.25: Transmission coefficient for system in Fig. 3.24 represent respectively the $W_1$=1.52 mm (red), $W_2$=1.2 mm (orange) and $W_3$=0.88 mm (blue). While the purple color shows the attenuation for the band gap region between 260 - 340 kHz

The rise and falls transmissions represent the filtering application in action. The ranges of frequencies to which the transmissions and attenuations were observed are according to the three waveguides sizes that have been carefully chosen in the previous discussion. In order to appreciate the filtering capabilities further, the displacement profile for the model in Fig. 3.24 was simulated. In this case, a monochromatic excitation source with single frequency that represents different waveguide frequencies ranges were considered. For instance in Fig. 3.26 when the frequency equivalent to 314 kHz that belongs to $W_1$, a single waveguide transmission can be observed with no other transmission in the rest of

the waveguides corridor. Similarly, at frequencies 288 kHz and 274 kHz that respectively belong to frequency $W_2$ and $W_3$ respectively, the transmission displacement is noticeable in the specific waveguide whilst no other channel transmission can be observed. The displacement result shows two important phenomena. The first phenomena is the system successfully represents the demultiplexing application in action, as have predicted earlier. Secondly, the number of pillars to which have been used in between the three waveguides corridor successfully separate the transmission for each waveguide from interacting with one another.

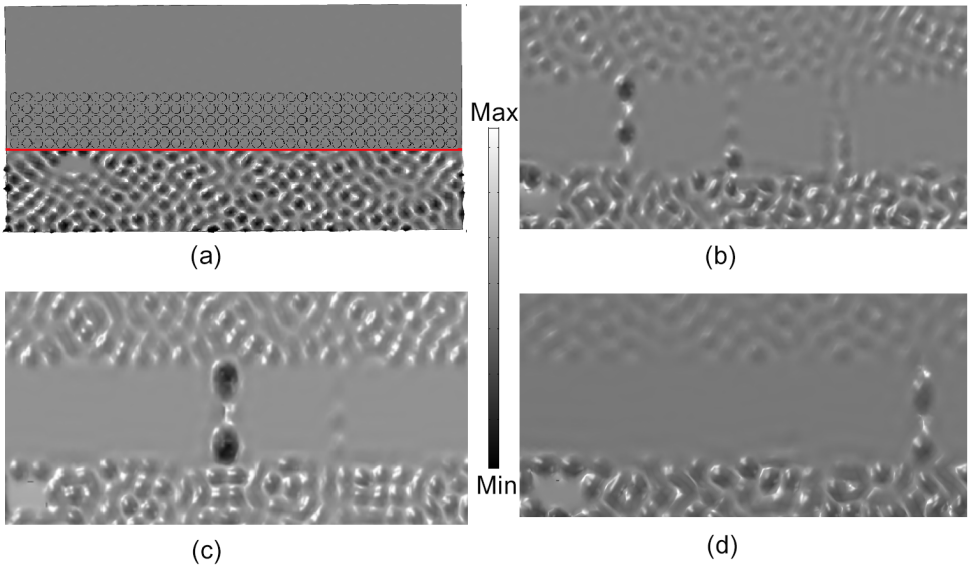


Figure 3.26: Displacement profile for demultiplexing system at (a) band gap frequency (b)$W_1$=314 kHz (c)$W_2$=288 kHz (d)$W_3$=274 kHz

## 3.7/ CONCLUSION

In this chapter, all the stages of simulation analysis are described through the basic modeling of a phononic crystal slab with a pillar resonator. A dispersion curve along the three directions of the irreducible Brillouin zone via unit cell structure and the frequency transmission spectrum via finite model structure were simulated for the band gap. The analysis between the dispersion and transmission curves shows a comparable existence and similar position of the forbidden band's frequency between 260 to 350 kHz. The frequencies region indicates an area where no propagation of elastic waves is allowed to pass through regardless of their polarisation. Due to the effect of periodic phononic crystal lattice, the effect of wave dispersive phenomena that leads to constructive and destructive interference, will then create the band gap region.

In order to create a localised mode inside the band gap, a defect must be introduced.

It is known that, through a Bloch-Floquet periodicity condition, a unit cells repeats itself infinitely to illustrate perfect crystals in predefined directions of wave vector, k. In such system defect can't be introduced and instead a supercell technique must be considered. Three waveguide parameters, $W_1$, $W_2$ and $W_3$, which correspond to three defect sizes, 1.52 mm, 1.2 mm and 0.88, were considered to filter three frequency ranges equal to 275-288, 288-303, 310-320 kHz. The localised mode can be shifted towards a higher or lower frequency according to the change of the defect distance due to the inverse relationship between mass and frequency. As observed in this chapter, the transmitting band has moved to a lower frequency area with a wider range of waveguide distance.

In order to explain the wave propagation phenomena in the structure, the displacement studies were also underlined. The results suggest that only unique ranges of frequencies can be received by each waveguide with an alternate propagation of wave was observed between three channels that depend on the incoming wave frequencies due to their inherent eigenvalue and own modes that respect the waveguide distance. Simulation studies thus confirmed the feasibility of the proposed model to produce a wide range of filtering demultiplexing as opposed to narrow transmission in previous researches.

# 4

# EXPERIMENTAL STUDY OF PHONONIC DEMULTIPLEXING

## 4.1/ INTRODUCTION

This chapter presents the experimental results based on simulation studies presented in chapter III. As to take the opportunity of the Fourth Industrial Revolution, 4th IR (the term coined by Klaus Schwab in the World Economic Forum, Davos in 2016), the fabrication method was based on the additive manufacturing (AM) technology. According to Eldem [71] the central tenet of 4th IR consists of among others internet of thing, autonomous robot, cyber security, and additive manufacturing. After 30 years of intensive research [72], AM has developed into a valid process for many production parts such as aeronautics and automotives but the usage of AM in the fabrication of phononic crystal structure is still limited and fall behind compared to other big industries. With this regards, the fabrication of phononic demultiplexing device in this chapter was based on AM technique.

The characterization of the device was done using a non-contact measuring instrument for surface vibrations based on Scanning Laser Doppler Vibrometer, SLDV. By sending a Laser on an oscillating surface, the SLDV measures the amplitude and the frequency of the surface vibrations based on the ”wavelength shift”. Then, the experiments from the Polytec SLDV equipment to characterize the surface cartography measurement and Femto-St Micro System Analyser, MSA equipment to measure the transmission coefficient were conducted. Details of experimental settings are described in detail in this chapter. Penultimately, the objective of this chapter is to verify the theoretical result as described in chapter III with the experimental result to demonstrate the feasibility of the demultiplexing device proposed by the dissertation.

## 4.2/ DEVELOPMENT OF STRUCTURE

### 4.2.1/ MATERIAL USED

To fabricate the PnC demultiplexing structures, the same aluminum alloy $AlSi_7Mg0_6$ (A357) for pillar and the substrate was used. Due to its rapid melting and solidification during direct metal printing, the material shows a good ductility and strength properties that popularly referred for industrial sectors like aeronautics and automotive [73]. The $AlSi_7Mg0_6$ combines the lower alloying elements of Silicon and equivalent proportion of Magnesium compared to $AlSi_{10}Mg$ that improves its electrical and thermal properties. The $AlSi_7Mg0_6$ was introduced as material in additive manufacturing technology in recent years along with $AlSi_{10}Mg$ alloy which was the primary material used in selective laser melting operation. The silicon content in both alloys made them a good implementation for laser melting that can stop hot cracking phenomena like intergranular or interdendritic cracking [74, 75]. The following tables 4.1 are chemical composition of $AlSi_7Mg0_6$ as provided by LPW Technology (LPW Technology Ltd, Runcorn, UK for laser powder bed fusion (LPBF) processing.

Table 4.1: Chemical composition of A357 [76]

| Alloy | Si | Mg | Zn | Ti | Cu | Fe | Mn | Al |
|---|---|---|---|---|---|---|---|---|
| A357 | 6.5–7.5 | 0.45–0.6 | <0.05 | 0.04–0.2 | <0.05 | <0.1 | <0.03 | Bal. |

Table 4.2: Optimized building parameters. [76]

| P(w) | v (mm/s) | $h_d$ (mm) | S (mm) |
|---|---|---|---|
| 195 | 1200 | 0.1 | 5 |

Aluminum (Al) alloys is the second most-used metal exceeded by steel only [77, 78] and due to their low density, Al alloys are one of the key materials in additive manufacturing (AM) technologies. According to Aversa et al., AM technology is the current fabrication technique with increasing number of publications per year [79]. However, despite its huge usage in the heavy industrial sector, none of the research has utilised the aluminium alloy for the PnC research. It is thus such an interesting opportunity to study its potential use as a subject of research in phononic crystal.

Since $AlSi_7Mg0_6$ is a new emerging material in AM, a few studies have been focused on the $AlSi_7Mg0_6$ samples produced via SLM method [80, 81]. In the context of AM process, the aluminium alloy is not a favorable material compared to their steels and Ti alloys counterparts. SLM process that used aluminum alloy is more difficult because of the high reflectivity (Aluminum can absorb just 7 per cent of the laser energy incident [82]). Thus, to resolve the high reflectivity issue, higher laser energies are needed. Interestingly, Si has a very high absorption rate (70 percent) and this could be a success factor in Al-

Si based alloys performance [82]. Beside these drawbacks, aluminum also has poor flowability, which may hinder the deposition of a thin layer powder that is vital to the SLM process. Two factors are directly related to the weak flow of aluminum powder: non-spherical shape and low density. The non-spherical shape of the powder is due to the atomisation process that developed the oxide island and these consequences cannot be prevented even under the inert environment [83]. Given the above difficulties, aluminum alloy under Selective Laser Melting can be achieved with success in the end product of the thesis demultiplexing model [57].

### 4.2.2/ Direct Metal Laser Sintering (DMLS) fabrication machine

The manufactured device was produced using ProX 300 machine by Thales (Fig.4.1) through Direct Metal Laser Sintering (DMLS). The machine has dimension 2,400 x 2,199 x 2,000 mm (94.5 x 86.6 x 94.5 in) and consisted of a building plate with dimensions of 250 mm x 250 mm x 330 mm (9.8 x 9.8 x 11.8 in). It utilized a 500 W Yb-fiber laser with a laser wavelength 1070 nm within a chamber filled with inert nitrogen or argon gas. The printer has axis resolution x=100 $\mu m$, y=100 $\mu m$, z=20 $\mu m$ and typical accuracy ± 0.1-0.2 $\%$ with ± 50 $\mu$ minimum.

Figure 4.1: DMLS process using PROX 300 machine

### 4.2.3/ Fabricated device

The final device of demultiplexing device is illustrated in Fig. 4.2 with 100 mm length, 172 mm width and 1 mm thickness. It was printed from AlSi7Mg06 aluminum alloy or A357 powder with a Poisson ratio of $\pi = 0.33$, a Young Modulus $E = 76.12GPa$ and a weight density of $\pi = 2670kgm^{-3}$ using the PROX 300 DMLS machine (Vide Supra).

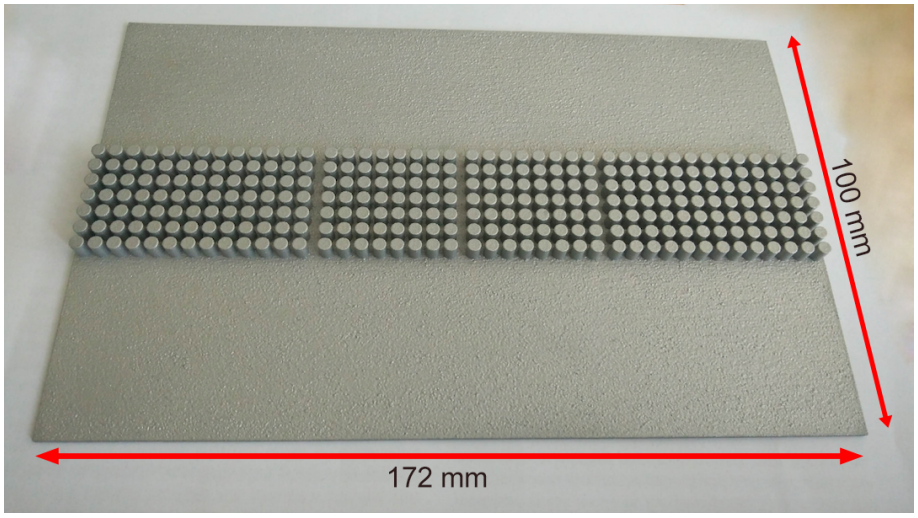


Figure 4.2: Fabricated demultiplexer device consists of 3 waveguides $W_1$=1.52 mm, $W_2$=1.22 mm, and $W_3$=0.88 mm

The demultiplexing consists of three linear waveguides channels, $W_d$ equivalent to $W_1$=1.52 mm, $W_2$=1.22 mm, and $W_3$=0.88 mm. Each of these linear waveguides is distanced by 8 rows of pillars to prevent any cross-talking between the waveguide axes. The unit cell parameter such as radius of pillar, $r_p$, height of pillar, $h_p$ are maintained according to simulation parameters as described in the previous section of the thesis.

Since all powder bed fusion machines need supporting structures during the printing process, the model would suffer from residual stress and distortion. The minimum slab thickness was recommended as 1 mm (which was taken into consideration during the simulation phase) to maintain the slab flatness and avoid any curving issues. Because of the construction nature of the process from melting metal to preheating temperatures (the preheating temperature of aluminum alloys is commonly within the range of 50-200 °C [84]) the thermal residual stresses and deformations are the common consequence of DMLS process. The area to be scanned receive a higher input of energy and may cause the base plate to warp and even leading to the warping of the entire base. Hence, the base plate must have sufficient thickness to prevent these situations. The thickness of the base plate clearly influences the distribution of residual stresses as shown by [85]. Therefore, a thick base plate, as opposed to a thin base plate, can avoid deformation due to component removal. The thermal deformations that occur after the model is removed from the base plate can be partially prevented by heat treatment with stress relief. But, the cracking or warping during the treatment are absolutely irreversible. Fig. 4.3 illustrates the warping plate as the thickness is equivalent to 0.4 mm and table 4.3 illustrates the discrepancies between the parameters of simulated and fabricated device in Fig. 4.2.

Figure 4.3: Warping issue due to thin plate that deformed because of residual stresses

Table 4.3: Discrepancies comparison between initial simulated and fabricated device

| Parameter dimension (mm) | | |
|---|---|---|
| Parameter | Initial simulation | fabricated device |
| Lattice, $a$ | 4.00 | 3.98 |
| Pillar height, $h_p$ | 4.40 | 4.40 |
| radius of pillar, $h_p$ | 1.60 | 1.55 |
| Slab thickness, $h$ | 1.00 | 1.00 |
| Waveguide, $W_1$ | 0.88 | 0.97 |
| Waveguide, $W_2$ | 1.20 | 1.28 |
| Waveguide, $W_3$ | 1.52 | 1.55 |

## 4.3/ EXPERIMENTAL PROCEDURE

### 4.3.1/ ELASTIC WAVE GENERATION AND DETECTION

Before measuring the propagation of elastic waves for the demultiplexing device, it is necessary to decide how to generate the elastic waves. The method of elastic wave generation in this thesis was based on the mechanical excitation by piezoelectric ceramic. The piezoelectric ceramics, PZ27 from the company Ferroperm num. 27303, made of PZT (Titanate-Lead Zirconate), was chosen for its good piezoelectric properties. This PZT patch has a dimension of 15 x 8 x 1 $mm^3$ and serves as a vibration source with frequency of up to 2 MHz. The patch was then glued to the bases using a silver glue to allow an electrical contacts between the piezocreamic to slab aluminium alloy substrate. The excitation was carried out by applying a potential difference of 7 V across the ceramic to produce a mechanical excitation source with a frequency ranges between 0.1 to 0.4 MHz. A similar approach can be found from other studies such as Miniaci et al.(2018), Coffy et al.(2017), and Baboly et al (2016). [34, 86, 87]

Several techniques can be used to detect the propagation of an elastic wave on the surface of a solid. Basically there are two methods of wave detection : direct contact via

piezoceramic or non-contact method via laser beam projection on the vibrating surface. Contact methods include the bonding of a piezoelectric transducer [34, 88] or the use of interdigitated combs [89–91]. The limitations of the contact techniques however occur in mass loading problem where the presence of accelerometer for instance will disturb the natural frequencies of measured device [64]. Due to the frequency shift, this provokes it to relevant uncertainties and inaccuracies on the resonance frequencies ascertainment. The resonance frequency shift due to mass loading can be described as following:

$$\Delta f = f_0 - f_n \Rightarrow \frac{\Delta f}{f_0} = 1 - \sqrt{\frac{m}{m + \Delta m}} \tag{4.1}$$

where $\Delta m$ is the mass loading, $f_0$ is the resonance frequency before the addition of mass loading, $f_n$ is the resonance frequency after the addition of mass loading and $\Delta f$ is the frequency shift. For a simple case, the issue of mass loading can be corrected by adding the mass equivalent to the mass of accelerometer to any DOF. However, in reality, it's unpractical to estimate the mass loading effect and should be treated as purely unreliable [64].

Meanwhile, contactless detection is based on the laser beams, whereby the incident beam properties will be modified by the vibration mode on the plate surface due to the passage of the elastic wave. Thus, the non-contact nature of this measurement technique can avoid this unwanted effect. Depending on the structural dynamics, the consideration can be made for laser-doppler vibrometry for out-of-plane vibration or stroboscopic video microscopy for in plane dynamic. In this thesis, the laser doppler vibrometry by optical interferometry [92–94], which is sensitive to the out-of-plane displacement was used.

### 4.3.2/ MSA-500 EXPERIMENTAL SETUP FOR TRANSMISSION MEASUREMENT

The MSA is equipped with a generator that allows for excitations with an arbitrary waveform and different patterns of excitation. In addition to the internal generator, the MSA-500 can be used with an external excitation source in case of pulse waveform or with an amplifier to increase the amplitude supply. In the current measurement setup, no external amplifier or wave generator were used in addition to the polytec-built-in internal generator. The source of wave excitation was generated by an internal generator alone by using Polytec software control. Under the acquisition setting, the white noise waveform with the amplitude equivalent to 7 V to excite the plate in a frequency range from 0.1 to 0.4 MHz was used. The sampling frequency is set to be equal to 400 kHz. In order to measure the sample in the test surface vibration, first it is necessary to determine the scan grid either manually or automatically. In the current setup, the scan grid 5 x 5 and 7 x 9 points, to respectively measure the band gap and waveguide transmission coefficient

were manually defined. The distance between two adjacent points are equivalent to 0.42 mm. The vibrometer then automatically moves to every point on the scanning grid and measures the response. The LDV was carried out in frequency domains, and the output laser acquisition is the Fast Fourier Transform (FFT) for the out-of plane displacement of every scanning point grid ($x_{1j}$, $x_{2j}$, $f$). The couple $x_{1j}$, $x_{2j}$ defines the scanning points and $j$=1,.....$N^2$, $f$ represent the frequency range of excitation as mentioned earlier. For each scanning point, the frequency swept from 0.1 to 0.4 MHz with FFT lines equal to 6400 were set with 128 repetition. The sampling time (the time for one complete frequency swept) was equal to 16 ms and the resolution (or frequency increment) was equivalent to 62.5 Hz. With a frequency swept between 0.1 to 0.4 MHz, the correct frequencies of interest can be chosen when the scan is complete, and the shape animation can be performed in both 2-D and 3-D display modes. In this thesis, frequency of interest was between 250 to 370 kHz where the appearance of band gap region can be found around the vicinity. Fig. 4.4(a) illustrates the setup of device measurement using MSA-500. In order to deduce the transmission coefficient, the out-of-plane waves excitation was done by applying force perpendicular to the plate surface by using PZT ceramics (vide supra). The PZT plate was positioned in front of the perfect periodic stub close to the device side limit-refer Fig. 4.4(b).

On the detection setting, the plate was placed perpendicular to the laser beam source by the 75 mm distant from the scanning eye of MSA head. The laser pointer will scan the plate surface area equivalent to 1.6 x1.6 $mm^2$ or 5 x 5 (in case of BnG measurement) spatial scanning points on the free surface between the perfect pillar structure. The laser scanned 4 different areas on the free surface within 4 different perfect crystal regions and their responses were registered.

Fig. 4.5 illustrates the 4 scanning surfaces marked with 4 differences colors (green, pink, red and black) to indicate the scanning region. Note that, no pillars were scanned on this stage. Only the free surface between the 4 pillars (as indicated by 4 colors) within the vicinity of perfect crystal were scanned and their respective plate's out-of-plane displacement field was registered. The signal excites the plate in a range of between 0.1 to 0.4 MHz and the measurements are displayed as Reduced Displacement (RD) by Equation :

$$RD = 20Log\left(\frac{1}{N_L}\sum\nolimits_{n\in L}\frac{|u_{n,z}(f)|}{1nm}\right) \tag{4.2}$$

Where N is the number of measurements taken during an integration time of 3.2 ms. The dBn index indicates that the quantity $u$ is displayed in a normalized dB scale with respect to one displacement nanometer (nm).

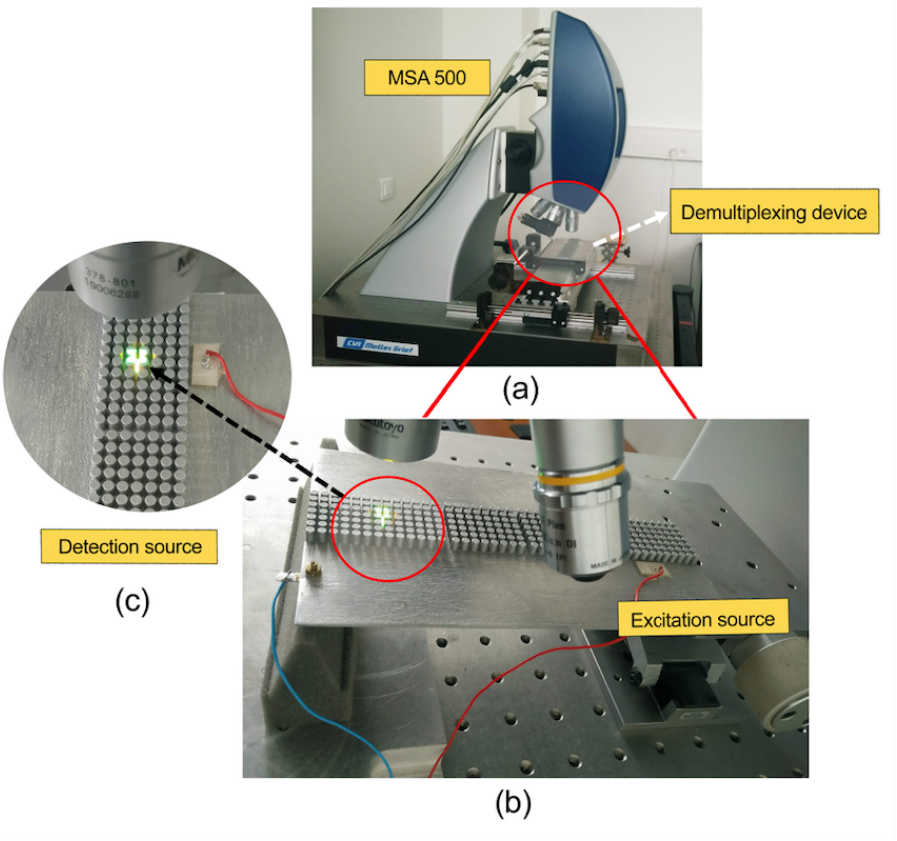


Figure 4.4: (a)Device setup using MSA-500 (b)laser beam was perpendicularly positioned to measure the surface vibration of device (c)the scanning detection area in the perfect crystal structure of the device

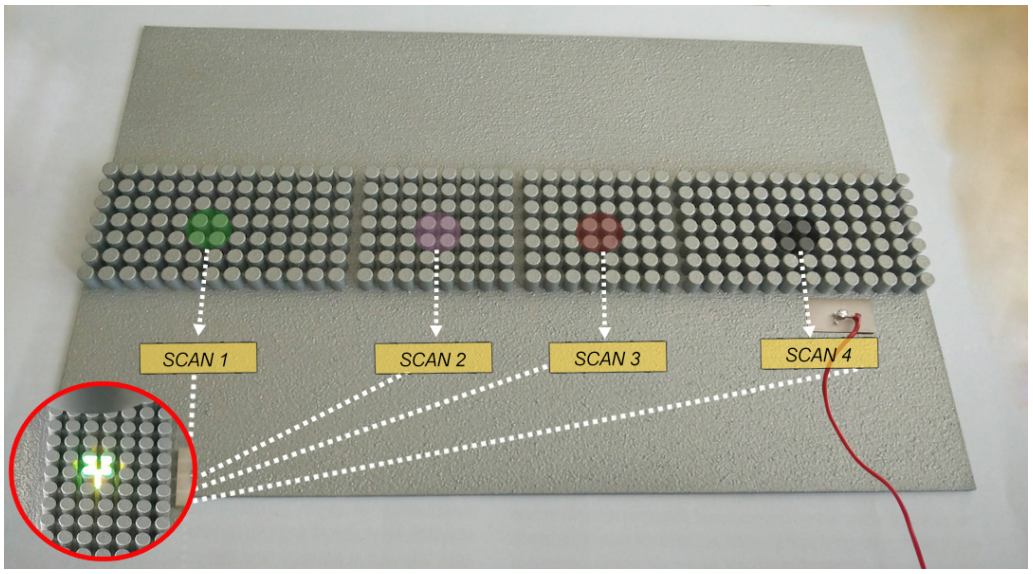


Figure 4.5: Three distinct color, green, pink, red and black marked the region where the laser beam were pointed on the plate's surface to measure the band gap transmission coefficient of the perfect crystals

In order to avoid any surface interactions, two procedures were considered. The first is to suspend the fabricated device by using nylon strings that are attached at every four corners of the device as shown in Fig. 4.6(a). Similar approaches can be found for instance by Baboly et al., when the device was suspended by the nylon strings to experimentally demonstrate the transmission of acoustic waveguiding in $90^0$ bends[34]. The method can also be used to position the device in vertical manner to do LDV measurement as can be found in other reports by Billon [95]. In short, this approaches not only can isolate the device from surrounding background but also gives more freedom to position the device in specific configuration to meet with particular measurement need. The second method is by using the prism foam underneath the fabricated device to ensure the acoustic isolation from the background as shown in Fig. 4.6(b). The latter was in fact very straight forward and for this reason the isolation method was adopted using Fig. 4.6(b) due to its simple and easy approach. Similar use can be found in other reports by [96].

In summary, the measurement to deduce the transmission coeeficient has the following setup :

- The device on its prism foam support
- A 3D scanning vibrometer (no filter) with its acquisition and excitation system to excite the piezoelectric patch at 7 Volt, frequency swept 0.1 to 0.4 Mhz. 5x5 scanning points for band gap transmission coefficient and 7x9 points for waveguides transmission were manually defined.
- A piezoelectric patch (Titanate-Lead Zirconate by Ferroperm) with dimension 15 x 8 x 1 $mm^3$ was connected to MSA excitation system.

With this setup, all the performance criteria, as mentioned above, was met.

### 4.3.3/ PSV-500 EXPERIMENTAL SETUP FOR SURFACE CARTOGRAPHY MEASUREMENT

Depending on the range of frequency, there are several types of PSV-500 vibrometer head A, B, H, M and HV that can detect the frequency up to 25 MHz. In this case, the measurement was used a single head PSV-500-3D-HV directed perpendicularly to the device surface area. A similar methods for wave excitation by using piezoelectric (PZT) transducer was fixed in order to generate elastic waves. The PZT patch was excited by using the internal vibrometer generator and controlled by the Polytec software. Two prism foams were positioned underneath the device to isolate from any surface interaction. In contrast to MSA, the surface cartography measurement was made on the free surface at

the back side of the device with no pillars or waveguides structures. The scanning covers a surface area 113 × 56.8 mm or proportionate to 97 × 49 points spatial grid (as marked in red region in Figure 4.7). Note that, the PSV-500 can have up to 512 × 512 scan point to have a high resolution spatial scanning with FFT lines up to 819,200.

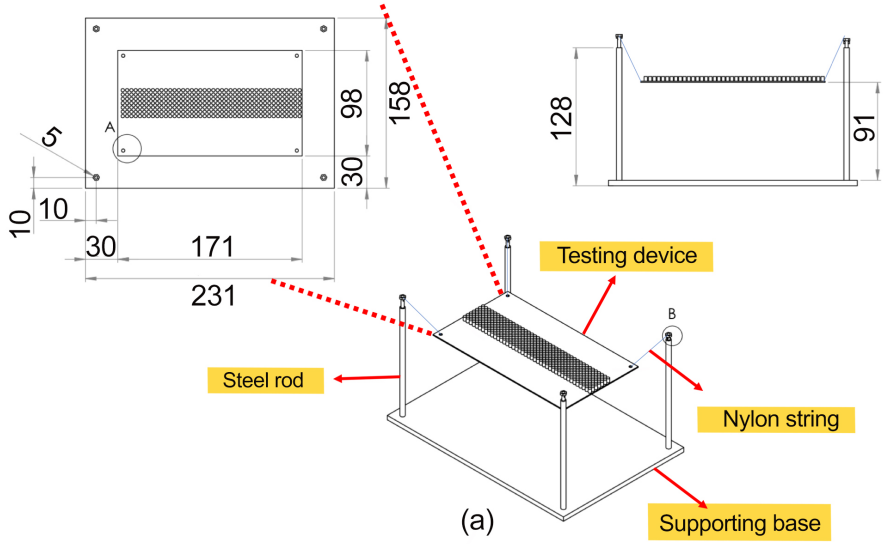


(a)

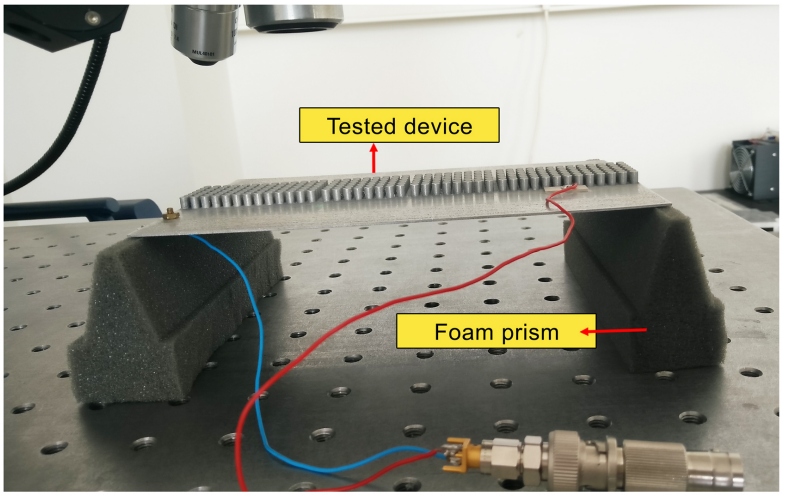


(b)

Figure 4.6: Method to separate demultiplexing device from environment (a)device hanged at four corners using the nylon string (b)foam prism to prevent surface contact between MSA-500 table and device surface.

In order to make the spatial vibration measurement, the following procedure was considered. First, define the geometry and generate the meshing area. The setting can be set up at the data acquisition or system generator as shown in Fig. 4.8(a). Later, the whole defined geometry will be automatically scanned by the laser beam according to defined spatial grid points that was defined earlier in the first step. At every point, the time and frequency response can be shown in real time during the scanning. After the automatic

scan, the final stage of visualization for 3D animation to display operation deflection shape (ODS) can be made. By using the ODS, a comparison can be made with FEM deflection shape to verify the simulation.

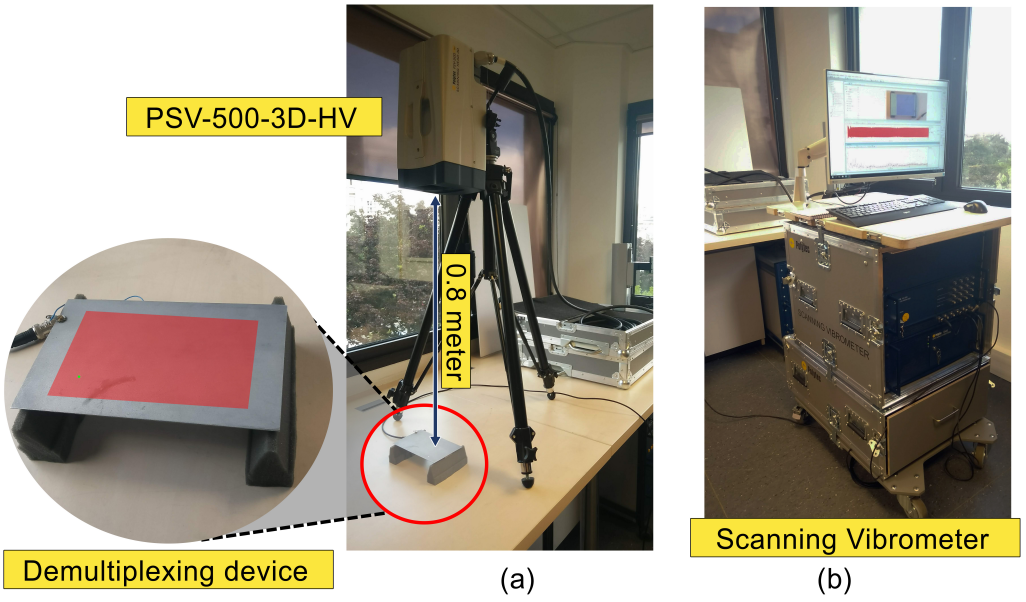


Figure 4.7: (a)Measuring setup for surface cartography measurement using PSV-500 (b)source of wave generation using standard PSV-500 scanning vibrometer

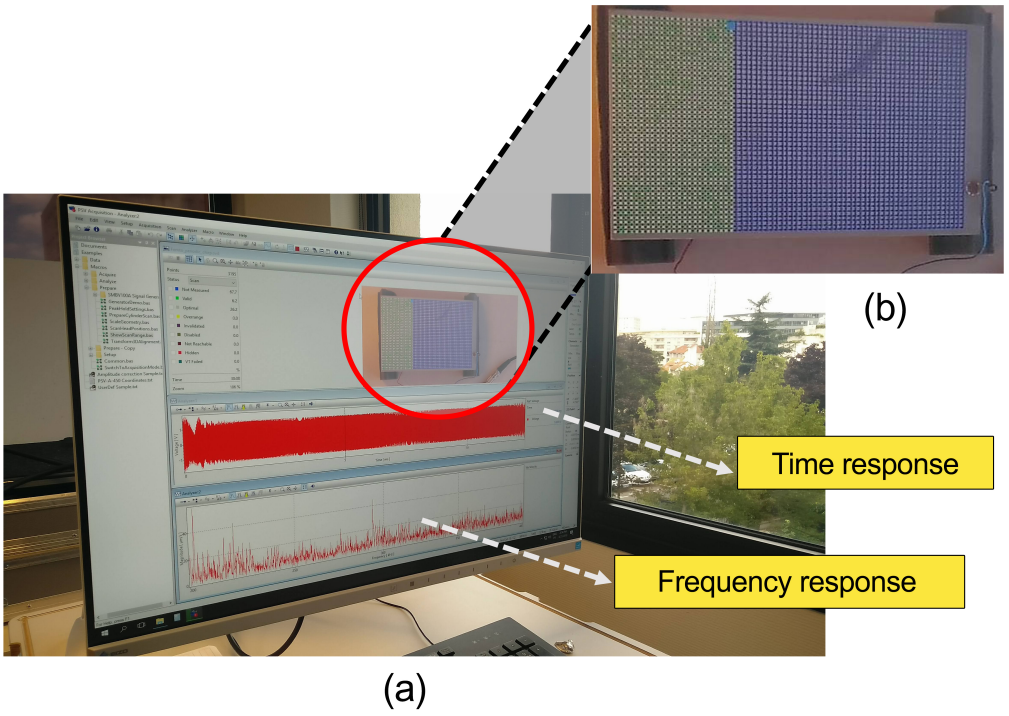


Figure 4.8: (a)Polytec software interface to control the geometry and meshing area of tested device (b)Zoomed of tested device under meshing stage

## 4.4/ RESULTS AND DISCUSSION

### 4.4.1/ BAND GAP TRANSMISSION COEFFICIENT SPECTRA

Fig. 4.9 illustrates the transmission coefficient result for the experimental setup as shown in Fig. 4.5 to measure the band gap of demultiplexing structure. From the point of view of transmission measurement, graph in Fig. 4.9 shows the elastics wave undergoing a very marked attenuation between 260 to 350 kHz with approximately 5 orders of attenuation magnitude which are noted for all 4 scanning areas between the attenuated band gap frequency.

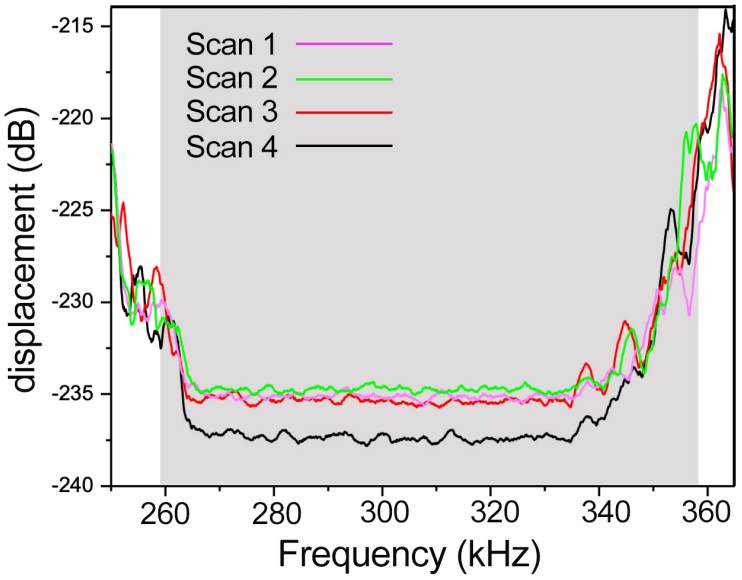


Figure 4.9: The comparison between band gap experimental transmission coefficient for Scan 1-4 at Fig. 4.5.

The experimental measurements are in very good agreement with the theoretical study drawn from the band diagram presented in Chapter 3 where the presence of a stop band between 260 to 350 kHz can be clearly seen. The origin of the attenuation is due to the destructive interference, probably linked to the periodicity of the structure. The average attenuation dip for the majority scanning points are on -235 dB except the scanning point 4 (black lines) which shows little enhance attenuation approximately -237 dB compared to the rest of scanning area. Thus, the scanning point 4 as to compare the experimental result with the simulation result was used. An excellent correlation between experimental (red line) and simulation (black line) findings in Fig. 4.10 shows a marked dip in the frequency range between 262 kHz and 347 kHz suggesting the presence of a band gap area as expected by the dispersion curve. Since the measurement only accesses the

out-of-plane modes through SLDV measurements, the focus should concern only on the out-of-plane band gap. This gap as shown in the grey region extends from 260 kHz to 350 kHz. The disparity between the simulation and the experimental values are due to the manufacturing conditions that vary slightly with original simulation parameters, thus leading to a small discrepancy between the simulated curve and experimental finding.

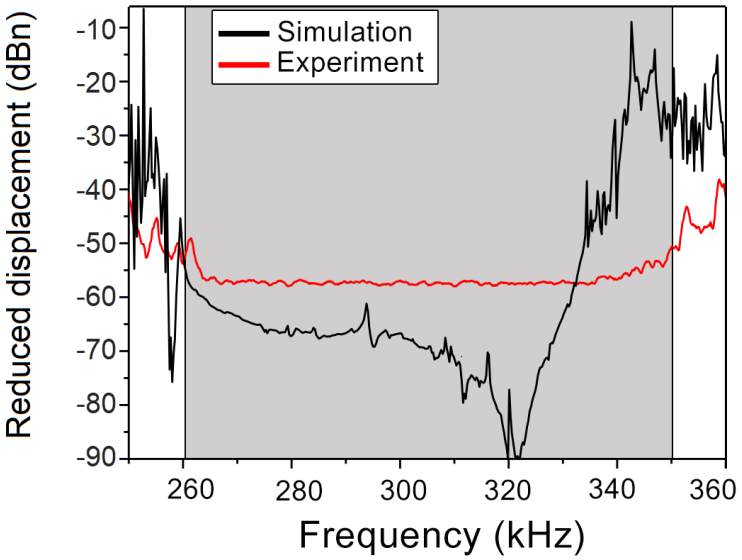


Figure 4.10: Comparison between simulated (black line) and experimental (red lines) transmission coefficient of the band gap

In order to understand the nature of the experimental band gap result, the catography displacement study to illustrate the wave blocking phenomena of the band gap frequency was conducted. As noted in top Fig. 4.11, the sending of a wave within the frequencies of band gap, $f$ = 265 kHz, results in a complete reflection of incoming waves in the phononic crystals boundaries as marked by the red line. The consequence of this omnidirectionality is confirmed by computational simulation of a single harmonic source that vibrates at the same frequency as shown in the bottom of Fig. 4.11.

### 4.4.2/ DEMULTIPLEXING TRANSMISSION COEFFICIENT SPECTRA

To experimentally verify the feasibility of three line-defect waveguides as a filter, an experimental measurement using a similar setup as described in the previous section to experimentally measure the transmission coefficient were conducted. The MSA-500 laser interferometer was centered at the end of each waveguide line. The scanning area was composed of a $4 \times 4\ mm^2$ square surface divided into 16 nodes. An average of the 16 nodes for the out-of-plane displacement was measured and recorded for each frequency, of the waveguide.

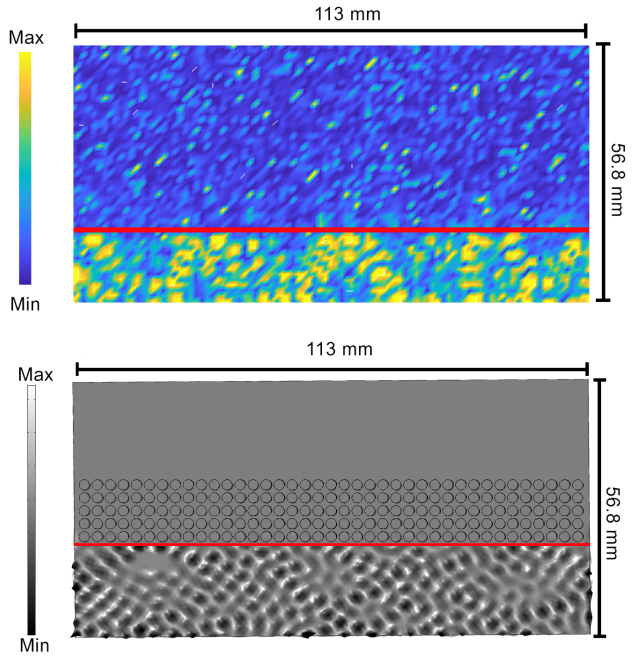


Figure 4.11: Experimental (top) and theoretical (bottom) for the displacement profile to illustrate the band gap phenomena at frequency, $f$=265 kHz

The experimental coefficient of transmission in Fig. 4.12 shows three ranges of frequencies transmission within the band gap, as predicted. The device acts as a filter in three different frequencies ranges: $f_{W1}$ = 274 - 287 kHz(red curve), $f_{W2}$ = 285 - 300 kHz (orange curve), and $f_{W3}$ = 301 - 315 kHz (blue curve).

For example, the transmission amplitude of W2 declines instantly at frequency f = 302 kHz (orange curve) when at the same time a significant transmission peak occurs at frequency f = 305 kHz which represents defects of the W3 channel (blue curve). By contrast, the W3 and W2 bands have a common criss-crossing narrow band extending from 280 to 287 kHz. The experimental transmission in top figure 4.12 has similar visible transmission of peaks and falls comparable to the simulated results. The existence of a complete transmission in one channel per time while keeping zero transmission on two other channels allows the selection of a given frequency for the filtering and demultiplexing application. The location and the transmission's maximum width are subjected to the waveguide distance parameters of the proposed phononic device that should be carefully chosen. The result shows, for each waveguide line compose of specific ranges of eigenvalue frequencies that allow them to specifically filter the incoming elastic waves with respective wavelength ranges. Regardless of the input wavelength coming to the input channel, the waveguide can only accept a narrow ranges of frequencies that belong to their natural eigenvalue.

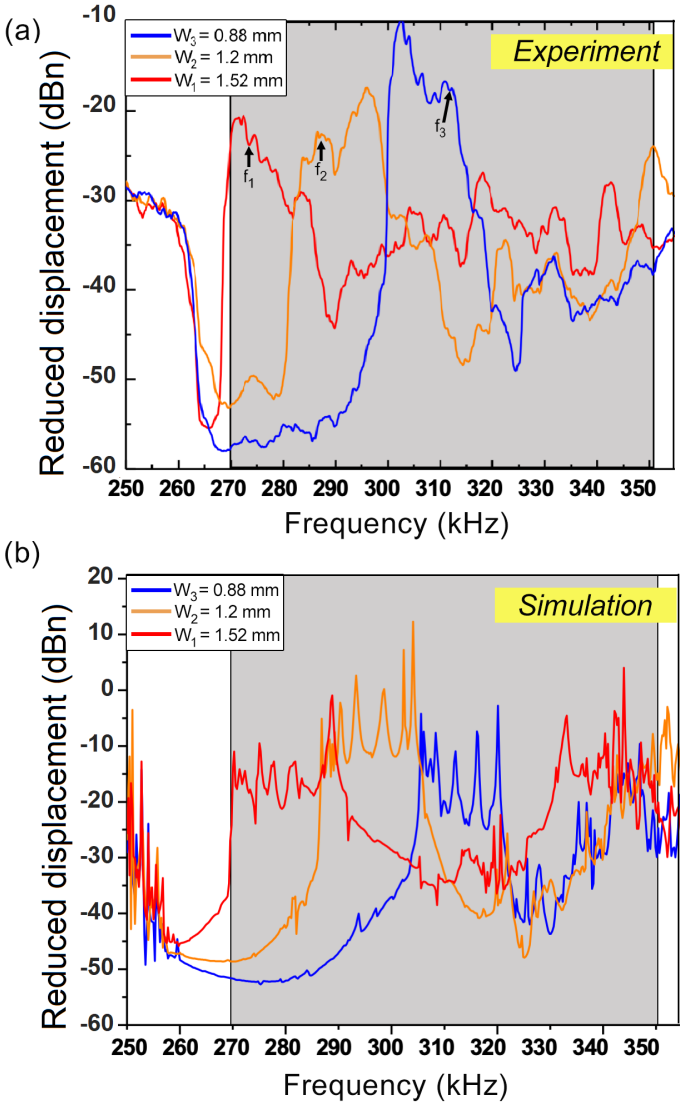


Figure 4.12: (a)Experimental transmission for three waveguides $W_1$=1.52 mm, $W_2$=1.22 mm, $W_3$=0.88 mm (b) simulated transmission for comparison with experimental

For each waveguide lines, there exists different threshold frequencies of entrance and exit that leads to the peak and dip of frequencies transmission. Within a frequency swept of the band gaps from 250 kHz to 400 kHz, there exists three separation filtering that corresponds to specific eigenvalue that belongs to a particular waveguide distance. These behaviors are consistent towards all three-difference channels, as can be noted in Fig. 4.12. The displacement characterization of the three waveguide structures were done by similar means as surface cartography measurement for the band gap. A displacement field measurement based on scanning laser Doppler vibrometer (SLDV) was performed to display the separation of the Lamb wave through the filter system. Fig. 4.13 shows the theoretical and experimental data for the out-of-plane displacement of the wave propagating through the demultiplexing system. In particular, each waveguide

entrance is supplied with a frequency swept from 250 kHz to 400 kHz to test its response.

The influence of the width of the guide has also been evaluated by the production and characterization of each waveguide. For instance, Fig. 4.13a indicates the waveguides with 275 kHz frequency filtering frequencies and the incident waves that are routed solely on one waveguide belonging to $W_3$ channels. The channels $W_2$ and $W_1$, which have filtering frequencies $f_{W2}$ = 288 - 303 kHz and $f_{W1}$ = 275 - 288 kHz respectively, show a significant wave attenuation over a wide range of frequencies. Likewise, both experiments and simulations in Fig. 4.13 (b) and (c) reveal a similar profile of selectivity. In Fig. 4.13b, the arriving waves were completely attenuated with $f_2$ = 288.4 kHz except for $W_2$ in the middle band. The same filtering phenomenon was observed for the W1 channel at frequency $f_3$ = 314 kHz as shown in Figure 4.13c. Thus, the cartography measurements in Fig. 4.13 have supported and confirmed the filtering behavior as observed in Fig. 4.12. For each intrinsic eigenvalues that represents particular waveguide, similar eigenmodes can be observed for the case of displacement study.

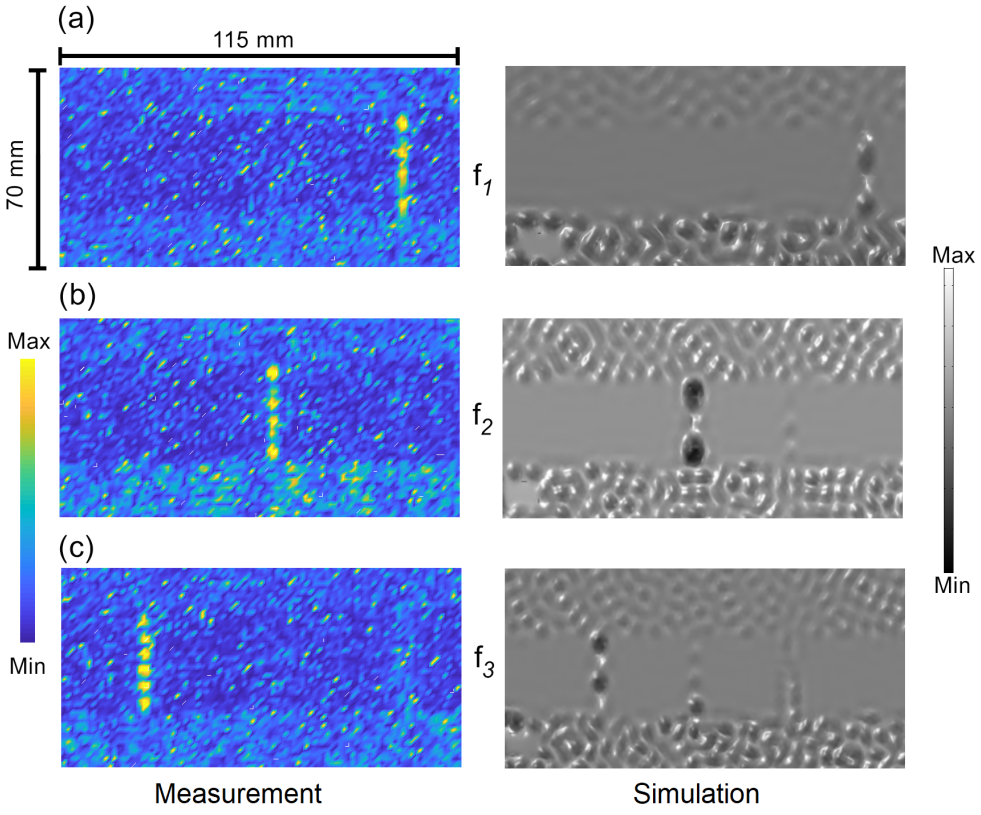


Figure 4.13: Experimental (on left) and theoretical (on right) displacement distribution for demultiplexer consists of three waveguides channels illustrate the filtering capability of system to distinguish three ranges of frequencies according to their respective channel

## 4.5/ CONCLUSION

Chapter four presents the thesis demultiplexing system which was manufactured using the 3D printing technology. The 3D printed approach is the most relevant technique of fabrication in the thesis because of the dimension of the demultiplexing system in macro scale and the operating frequency in kHz ranges. Compared to the simulated model, the final manufacturing has good dimensional tolerance, which implies the good precision of the manufacturing machine and the good choice of manufacturing method. The Micro System Analyzer (MSA), MSA-500 was used to calculate the experimental analysis to measure the transmission coefficient for both the band gap and waveguides. Measurement results showed that both simulation and experiments demonstrate similar location and size of the band gap and waveguide transmission frequencies. The response of the demultiplexing system to filter very specific frequency ranges were observed as agreed in simulation stages in three frequency transmission ranges at 274-287, 285-300 and 301-315 kHz. The displacement profile was performed using the scanning laser Doppler vibrometer (SLDV). The propagation of wave on the structure followed exactly the permitted or prohibited frequency as simulated. The wave was observed to transmit in one out of three channels per time according to their “designed” frequencies which suggests the confirmed behavior of thesis demultiplexing for wide frequencies filtering functions.

# 5

# CONCLUSION

In Chapter One, the thesis highlighted the problem statement and the objectives of current phononic crystal demultiplexing research. The limitation on the previous methods based on thermal and liquid altering was criticized due to its inconsistent nature that can be influenced by the environmental swings. In term of filtering, all approaches produced a consistent narrow-pass band transmission to filter the frequency and none of the studies have showed both theoretically and experimentally the wide and continuous filtering as aim in the current dissertation. The second chapter gives a general overview on phononic and photonic history and their inherent similarity in term of research approaches and theories. Several important concepts such as the crystal lattice geometry that resulted from the band gap phenomena was also mentioned. The chapter also discussed in more detail about the previous method of phononic crystal demultiplexing and summaries on their drawbacks were discussed. The inherent narrow pass-band transmission in previous approaches was the major source of filtering drawback of previous filtering approaches that limit their function. The lack of fabrication and experimental work were also the other limitation. In addition, it discussed about the numerical and measurement aspects used in the current thesis. The fundamental aspects on simulation methods based on finite element to study various important phenomena of PnC and the experimental method such as the wave generation and detection method were discussed, too.

In the third chapter, result on the computational analysis of the unit cell structure using the Finite Element Method was presented. Specifically, with the undisturbed and periodically repetition of unit cell, two sources of band gaps were observed. The first consists of two partial band gaps that only can block the wave propagation in one irreducible Brillouin zone direction. The second band gap was a complete band gap between 272 to 347 kHz that can hinder wave propagation in all Brillouin zone directions regardless of their polarisations. The periodical structure of unit cell that incites the dispersive phenomena of incoming wave caused a constructive and destructive interference for the band gap formation. The presence of guided modes within the band gap was later introduced by using the supercell technique to enable the phononic defect inside the perfect crystal

structure. With carefully tuning of the waveguide distance, the localised mode can be shifted towards a higher or lower frequency according to the adjustment of defect gap. Specifically, with wider distance of waveguide size, the transmitting band shifted towards the lower region of frequencies due to the inverse relation between mass and frequency. Three distinct waveguide parameters, W1, W2 and W3 that were respectively equivalent to three defect sizes, 1.52 mm, 1.2 mm and 0.88 were considered to filter three ranges of frequencies equivalent to 275-288, 288-303, 310-320 kHz. The displacement studies were also highlighted to understand the propagation phenomena in the structure. Results suggested that, each waveguide can only receive specific ranges of frequencies. An alternate propagation of waves was observed between three channels that depended on the incoming wave frequencies due to their inherent eigenvalue and eigenmodes for each waveguide lines.

Chapter four discussed about fabrication method to realize the simulated structure in chapter 2. To appreciate the currently trending 3D printed technology, the device was fabricated by using Sintering Laser Method (SLM) based on the aluminium alloy. Due to the dimension of the demultiplexing device in macro or mm size and with the frequencies filtering in kHz ranges, the 3D printed method is the most favorable method. The final result has good tolerance of dimensions compared to simulated model which suggests the good precision of fabrication machine and the good choice of fabrication method. The experimental study to measure the transmission coefficient for both the band gap and waveguides were also measured using the Micro System Analyzer (MSA), MSA-500 that was available in Femto-St Laboratory. Experimental finding demonstrated that, the position and size of the band gap were similar with simulation studies at the earlier stage. Three ranges of frequencies transmission and dip were observed at 274-287, 285-300 and 301-315 kHz suggested the efficiency and sensitivity of demultiplexing device to filter very specific frequencies ranges. The displacement profile by using scanning laser Doppler vibrometer (SLDV) was conducted in Polytec Paris. The propagation of wave on the structure followed exactly the allowed or prohibited frequency as simulated. The wave was observed to transmit in one out of three channels per time according to their “designed” frequencies. Consequently, the experiment result has successfully validated the simulated finding for the filtering and demultiplexing application.

In conclusion, the studies have showed the ability to filter wide ranges of frequencies as oppose to narrow-pass band in previous studies. The wider frequencies transmission allow for wider capability and offer more freedom of selectivity in term of filtering ability. The demultiplexing also ensures a consistent behavior of filtering throughout the change of surrounding since the very approaches considered in the thesis was not based on thermal influence or the properties of liquid that can barely maintain their pristine states under the surrounding changes. Finally, the following objectives have been accomplished in the thesis to solve the problem statement in the current PnC demultiplexing research :

- Simulation works on several transmission to filter wide and ranges kHz frequencies filtering.
- Fabrication works on demultiplexing device.
- Experimental studies on frequencies transmissions and their respective cartography displacement measurement
- Comparison between simulation and experiment to verify the method of demultiplexing considered in current thesis to produce wide ranges of frequencies of demultiplexing device.

## 5.1/ PERSPECTIVES AND RECOMMENDATION

In most applications associated with chemical, biological and biomedical the handling of liquids is an important aspect. A variety of different liquid handling have been applied to various fluid processing scenarios including microdroplets, hydrodynamics, pneumatic valves, electrical, acoustics and magnetics. Adding to the list, the findings obtained from this study may be useful for the future multiple droplet manipulation applications. Several manipulations can be introduced through a droplet division of demultiplexing system that involve transporting or releasing the droplet according to particular filtering frequencies. Particularly, the advantage of the slab based structure enables the manipulation to be conducted at the back side of the slab interfaced with a free phononic crystal structure. This can provide a platform for the droplet manipulation to have transmission success while preserving its pristine droplet state because any unnecessary contact with the PnC structure can be avoided. Furthermore, manipulation of waveguide channels into several configurations directions can be another interesting study to have more system design flexibility on controlling the direction of droplet movement. The concept can be further explored to find other band gap frequency ranges below than 10 Hz for the microfluidic applications. Within this ranges of frequencies, the waveguide can be introduced for filtering and sorting the micro droplet.

# BIBLIOGRAPHY


**[1]** LAUDE, V. **Phononic crystals: artificial crystals for sonic, acoustic, and elastic waves**, vol. 26. Walter de Gruyter GmbH & Co KG, 2015.

**[2]** SIGALAS, M. **Elastic wave band gaps and defect states in two-dimensional composites**. *The Journal of the Acoustical Society of America 101*, 3 (1997), 1256–1261.

**[3]** SIGALAS, M. **Defect states of acoustic waves in a two-dimensional lattice of solid cylinders**. *Journal of Applied Physics 84*, 6 (1998), 3026–3030.

**[4]** TORRES, M., DE ESPINOSA, F. M., GARCIA-PABLOS, D., AND GARCIA, N. **Sonic band gaps in finite elastic media: surface states and localization phenomena in linear and point defects**. *Physical Review Letters 82*, 15 (1999), 3054.

**[5]** KHELIF, A., DJAFARI-ROUHANI, B., VASSEUR, J., AND DEYMIER, P. A. **Transmission and dispersion relations of perfect and defect-containing waveguide structures in phononic band gap materials**. *Physical Review B 68*, 2 (2003), 024302.

**[6]** WU, L.-Y., CHEN, L.-W., AND LIU, C.-M. **Acoustic pressure in cavity of variously sized two-dimensional sonic crystals with various filling fractions**. *Physics Letters A 373*, 12-13 (2009), 1189–1195.

**[7]** KHELIF, A., WILM, M., LAUDE, V., BALLANDRAS, S., AND DJAFARI-ROUHANI, B. **Guided elastic waves along a rod defect of a two-dimensional phononic crystal**. *Physical Review E 69*, 6 (2004), 067601.

**[8]** WU, T.-T., HUANG, Z.-G., AND LIN, S. **Surface and bulk acoustic waves in two-dimensional phononic crystal consisting of materials with general anisotropy**. *Physical review B 69*, 9 (2004), 094301.

**[9]** CHARLES, C., BONELLO, B., AND GANOT, F. **Propagation of guided elastic waves in 2d phononic crystals**. *Ultrasonics 44* (2006), e1209–e1213.

**[10]** ACHAOUI, Y., KHELIF, A., BENCHABANE, S., AND LAUDE, V. **Polarization state and level repulsion in two-dimensional phononic crystals and waveguides in the presence of material anisotropy**. *Journal of Physics D: Applied Physics 43*, 18 (2010), 185401.

**[11]** NAGATY, A., MEHANEY, A., AND ALY, A. H. **Influence of temperature on the properties of one-dimensional piezoelectric phononic crystals**. *Chinese Physics B 27*, 9 (2018), 094301.

**[12]** JOANNOPOULOS, J. D., JOHNSON, S. G., WINN, J. N., AND MEADE, R. D. **Photonic cristal book. molding the flow of light**, 2007.

**[13]** RAYLEIGH, L. **Xvii. on the maintenance of vibrations by forces of double frequency, and on the propagation of waves through a medium endowed with a periodic structure**. *The London, Edinburgh, and Dublin Philosophical Magazine and Journal of Science 24*, 147 (1887), 145–159.

**[14]** YABLONOVITCH, E. **Photonic band-gap structures**. *JOSA B 10*, 2 (1993), 283–295.

**[15]** ELKARAMANY, E. M., HAMEED, M. F. O., AND OBAYYA, S. **Fundamentals of photonic crystals**. In *Computational Photonic Sensors*. Springer, 2019, pp. 29–52.

**[16]** YABLONOVITCH, E. **Inhibited spontaneous emission in solid-state physics and electronics**. *Physical review letters 58*, 20 (1987), 2059.

**[17]** JOHN, S. **Strong localization of photons in certain disordered dielectric superlattices**. *Physical review letters 58*, 23 (1987), 2486.

**[18]** TAMURA, S., HURLEY, D., AND WOLFE, J. **Acoustic-phonon propagation in superlattices**. *Physical Review B 38*, 2 (1988), 1427.

**[19]** KUSHWAHA, M. S., HALEVI, P., MARTINEZ, G., DOBRZYNSKI, L., AND DJAFARI-ROUHANI, B. **Theory of acoustic band structure of periodic elastic composites**. *Physical Review B 49*, 4 (1994), 2313.

**[20]** SIGALAS, M., KUSHWAHA, M. S., ECONOMOU, E. N., KAFESAKI, M., PSAROBAS, I. E., AND STEURER, W. **Classical vibrational modes in phononic lattices: theory and experiment**. *Zeitschrift für Kristallographie-Crystalline Materials 220*, 9-10 (2005), 765–809.

**[21]** FRAZIER, M. J. **Dissipative wave propagation in phononic crystals and metamaterials: Models and analysis**.

**[22]** SIGALAS, M., AND ECONOMOU, E. N. **Band structure of elastic waves in two dimensional systems**. *Solid state communications 86*, 3 (1993), 141–143.

**[23]** CROËNNE, C., LEE, E., HU, H., AND PAGE, J. **Band gaps in phononic crystals: Generation mechanisms and interaction effects**. *AIP Advances 1*, 4 (2011), 041401.

**[24]** WU, T.-T., HUANG, Z.-G., TSAI, T.-C., AND WU, T.-C. **Evidence of complete band gap and resonances in a plate with periodic stubbed surface**. *Applied Physics Letters 93*, 11 (2008), 111902.

**[25]** YI, G., AND YOUN, B. D. **A comprehensive survey on topology optimization of phononic crystals**. *Structural and Multidisciplinary Optimization 54*, 5 (2016), 1315–1344.

**[26]** KITTEL, C., AND OTHERS. **Introduction to solid state physics**, vol. 8. Wiley New York, 1976.

**[27]** ADDOUCHE, M., AL-LETHAWE, M. A., ELAYOUCH, A., AND KHELIF, A. **Subwavelength waveguiding of surface phonons in pillars-based phononic crystal**. *AIP Advances 4*, 12 (2014), 124303.

**[28]** TALEB, F., AND DARBARI, S. **Tunable locally resonant surface-acoustic-waveguiding behavior by acoustoelectric interaction in zn o-based phononic crystal**. *Physical Review Applied 11*, 2 (2019), 024030.

**[29]** WANG, X.-P., JIANG, P., CHEN, T.-N., AND ZHU, J. **Tuning characteristic of band gap and waveguide in a multi-stub locally resonant phononic crystal plate**. *AIP Advances 5*, 10 (2015), 107141.

**[30]** GHASEMI BABOLY, M., REINKE, C. M., GRIFFIN, B. A., EL-KADY, I., AND LESEMAN, Z. **Acoustic waveguiding in a silicon carbide phononic crystals at microwave frequencies**. *Applied Physics Letters 112*, 10 (2018), 103504.

**[31]** SAFAVI-NAEINI, A. H., AND PAINTER, O. **Design of optomechanical cavities and waveguides on a simultaneous bandgap phononic-photonic crystal slab**. *Optics express 18*, 14 (2010), 14926–14943.

**[32]** POURABOLGHASEM, R., DEHGHANNASIRI, R., EFTEKHAR, A. A., AND ADIBI, A. **Waveguiding effect in the gigahertz frequency range in pillar-based phononic-crystal slabs**. *Physical Review Applied 9*, 1 (2018), 014013.

**[33]** ZHAO, J., YUAN, W., BOYKO, O., BONELLO, B., ZHANG, X., PAN, Y., AND ZHONG, Z. **Experimental evidence of quadrupolar whispering-gallery modes in phononic crystal based waveguides**. *AIP Advances 9*, 8 (2019), 085032.

**[34]** GHASEMI BABOLY, M., RAZA, A., BRADY, J., REINKE, C., LESEMAN, Z. C., AND EL-KADY, I. **Demonstration of acoustic waveguiding and tight bending in phononic crystals**. *Applied Physics Letters 109*, 18 (2016), 183504.

**[35]** HU, R., WU, J., YANG, Y., WANG, X., JIA, H., DENG, K., HE, Z., AND ZHAO, H. **Tunable composite waveguide based on piezoelectric phononic crystal**. *AIP Advances 9*, 4 (2019), 045120.

**[36]** ROSTAMI-DOGOLSARA, B., MORAVVEJ-FARSHI, M. K., AND NAZARI, F. **Designing phononic crystal based tunable four-channel acoustic demultiplexer**. *Journal of Molecular Liquids 281* (2019), 100–107.

**[37]** JIN, Y., FERNEZ, N., PENNEC, Y., BONELLO, B., MOISEYENKO, R. P., HÉMON, S., PAN, Y., AND DJAFARI-ROUHANI, B. **Tunable waveguide and cavity in a phononic crystal plate by controlling whispering-gallery modes in hollow pillars**. *Physical Review B 93*, 5 (2016), 054109.

**[38]** JIN, Y., PENNEC, Y., PAN, Y., AND DJAFARI-ROUHANI, B. **Phononic crystal plate with hollow pillars actively controlled by fluid filling**. *Crystals 6*, 6 (2016), 64.

**[39]** ZHAO, J., YUAN, W., BONELLO, B., DJAFARI-ROUHANI, B., PAN, Y., AND ZHONG, Z. **Rainbow guiding of the lowest-order antisymmetric lamb mode in phononic crystal plate**. *Science China Technological Sciences 62*, 3 (2019), 458–463.

**[40]** ZHU, J., CHEN, Y., ZHU, X., GARCIA-VIDAL, F., YIN, X., ZHANG, W., AND ZHANG, X. **Acoustic rainbow trapping sci**, 2013.

**[41]** COLOMBI, A., AGEEVA, V., SMITH, R. J., CLARE, A., PATEL, R., CLARK, M., COLQUITT, D., ROUX, P., GUENNEAU, S., AND CRASTER, R. V. **Enhanced sensing and conversion of ultrasonic rayleigh waves by elastic metasurfaces**. *Scientific reports 7*, 1 (2017), 6750.

**[42]** ZHOU, C., YUAN, B., CHENG, Y., AND LIU, X. **Precise rainbow trapping for low-frequency acoustic waves with micro mie resonance-based structures**. *Applied Physics Letters 108*, 6 (2016), 063501.

**[43]** NI, X., WU, Y., CHEN, Z.-G., ZHENG, L.-Y., XU, Y.-L., NAYAR, P., LIU, X.-P., LU, M.-H., AND CHEN, Y.-F. **Acoustic rainbow trapping by coiling up space**. *Scientific reports 4* (2014), 7038.

**[44]** BEN-ALI, Y., KHALED, A., BRIA, D., AND OTHERS. **Y-shaped branch structure using asymmetric resonators for phononic demultiplexing**. *Materials Today: Proceedings* (2020).

**[45]** LI, G.-H., WANG, Y.-Z., AND WANG, Y.-S. **Active control on switchable waveguide of elastic wave metamaterials with the 3d printing technology**. *Scientific reports 9*, 1 (2019), 1–8.

**[46]** WANG, Y.-F., WANG, T.-T., LIU, J.-P., WANG, Y.-S., AND LAUDE, V. **Guiding and splitting lamb waves in coupled-resonator elastic waveguides**. *Composite Structures 206* (2018), 588–593.

**[47]** KHELIF, A., AOUBIZA, B., MOHAMMADI, S., ADIBI, A., AND LAUDE, V. **Complete band gaps in two-dimensional phononic crystal slabs**. *Physical Review E 74*, 4 (2006), 046610.

**[48]** PENNEC, Y., DJAFARI-ROUHANI, B., LARABI, H., VASSEUR, J., AND HLADKY-HENNION, A. **Low-frequency gaps in a phononic crystal constituted of cylindrical dots deposited on a thin homogeneous plate**. *Physical Review B 78*, 10 (2008), 104105.

**[49]** HSU, J.-C., AND WU, T.-T. **Efficient formulation for band-structure calculations of two-dimensional phononic-crystal plates**. *Physical review B 74*, 14 (2006), 144303.

**[50]** LAURETI, S., AKANJI, O., DAVIS, L., LEIGH, S., HUTCHINS, D., AND RICCI, M. **Design and characterization of 3d-printed phononic crystals for sub-mhz ultrasound manipulation**. In *2015 IEEE International Ultrasonics Symposium (IUS)* (2015), IEEE, pp. 1–4.

**[51]** LUCKLUM, F., AND VELLEKOOP, M. **Rapid prototyping of 3d phononic crystals using high-resolution stereolithography fabrication**. *Procedia engineering 120* (2015), 1095–1098.

**[52]** WARMUTH, F., WORMSER, M., AND KÖRNER, C. **Single phase 3d phononic band gap material**. *Scientific reports 7*, 1 (2017), 1–7.

**[53]** D'ALESSANDRO, L., BELLONI, E., ARDITO, R., CORIGLIANO, A., AND BRAGHIN, F. **Modeling and experimental verification of an ultra-wide bandgap in 3d phononic crystal**. *Applied Physics Letters 109*, 22 (2016), 221907.

**[54]** WORMSER, M., WARMUTH, F., AND KÖRNER, C. **Evolution of full phononic band gaps in periodic cellular structures**. *Applied Physics A 123*, 10 (2017), 661.

**[55]** WORMSER, M., WEIN, F., STINGL, M., AND KÖRNER, C. **Design and additive manufacturing of 3d phononic band gap structures based on gradient based optimization**. *Materials 10*, 10 (2017), 1125.

**[56]** TOL, S., DEGERTEKIN, F., AND ERTURK, A. **3d-printed phononic crystal lens for elastic wave focusing and energy harvesting**. *Additive Manufacturing 29* (2019), 100780.

**[57]** SERCOMBE, T., AND LI, X. **Selective laser melting of aluminium and aluminium metal matrix composites**. *Materials Technology 31*, 2 (2016), 77–85.

**[58]** ABOULKHAIR, N. T., EVERITT, N. M., MASKERY, I., ASHCROFT, I., AND TUCK, C. **Selective laser melting of aluminum alloys**. *MRS Bulletin 42*, 4 (2017), 311–319.

**[59]** LI, X. P., JI, G., CHEN, Z., ADDAD, A., WU, Y., WANG, H., VLEUGELS, J., VAN HUMBEECK, J., AND KRUTH, J.-P. **Selective laser melting of nano-tib2 decorated alsi10mg alloy with high fracture strength and ductility**. *Acta Materialia 129* (2017), 183–193.

**[60]** DAS, S. **Physical aspects of process control in selective laser sintering of metals**. *Advanced Engineering Materials 5*, 10 (2003), 701–711.

**[61]** OLAKANMI, E. **Selective laser sintering/melting (sls/slm) of pure al, al–mg, and al–si powders: Effect of processing conditions and powder properties**. *Journal of Materials Processing Technology 213*, 8 (2013), 1387–1405.

**[62]** WEINGARTEN, C., BUCHBINDER, D., PIRCH, N., MEINERS, W., WISSENBACH, K., AND POPRAWE, R. **Formation and reduction of hydrogen porosity during selective laser melting of alsi10mg**. *Journal of Materials Processing Technology 221* (2015), 112–120.

**[63]** LUCKLUM, F., AND VELLEKOOP, M. J. **Design and fabrication challenges for millimeter-scale three-dimensional phononic crystals**. *Crystals 7*, 11 (2017), 348.

**[64]** CASTELLINI, P., MARTARELLI, M., AND TOMASINI, E. **Laser doppler vibrometry: Development of advanced solutions answering to technology's needs**. *Mechanical systems and signal processing 20*, 6 (2006), 1265–1285.

**[65]** FU, Y., GUO, M., AND PHUA, P. B. **Multipoint laser doppler vibrometry with single detector: principles, implementations, and signal analyses**. *Applied optics 50*, 10 (2011), 1280–1288.

**[66]** KHELIF, A., CHOUJAA, A., BENCHABANE, S., DJAFARI-ROUHANI, B., AND LAUDE, V. **Guiding and bending of acoustic waves in highly confined phononic crystal waveguides**. *Applied physics letters 84*, 22 (2004), 4400–4402.

**[67]** WU, T.-C., WU, T.-T., AND HSU, J.-C. **Waveguiding and frequency selection of lamb waves in a plate with a periodic stubbed surface**. *Physical Review B 79*, 10 (2009), 104306.

**[68]** BERENGER, J.-P. **A perfectly matched layer for the absorption of electromagnetic waves**. *Journal of computational physics 114*, 2 (1994), 185–200.

**[69]** SÁNCHEZ-DEHESA, J., AND KROKHIN, A. **Introduction to acoustics of phononic crystals. homogenization at low frequencies**. In *Phononic Crystals*. Springer, 2016, pp. 1–21.

**[70]** POURABOLGHASEM, R., KHELIF, A., MOHAMMADI, S., EFTEKHAR, A. A., AND ADIBI, A. **Physics of band-gap formation and its evolution in the pillar-based phononic crystal structures**. *Journal of Applied Physics 116*, 1 (2014), 013514.

**[71]** ELDEM, M. O. **Endüstri 4.0**. *TMMOB EMO Ankara Şubesi Haber Bülteni 3*, 2 (2017).

**[72]** HUANG, S. H., LIU, P., MOKASDAR, A., AND HOU, L. **Additive manufacturing and its societal impact: a literature review**. *The International Journal of Advanced Manufacturing Technology 67*, 5-8 (2013), 1191–1203.

**[73]** NANDY, J., SARANGI, H., AND SAHOO, S. **A review on direct metal laser sintering: Process features and microstructure modeling**. *Lasers in Manufacturing and Materials Processing 6*, 3 (2019), 280–316.

**[74]** MAUDUIT, A., PILLOT, S., AND FRASCATI, F. **Application study of alsi10mg alloy by selective laser melting: physical and mechanical properties, microstructure, heat treatments and manufacturing of aluminium metallic matrix composite (mmc)**. *Metallurgical research & technology 112*, 6 (2015), 605.

**[75]** MAUDUIT, A., PILLOT, S., AND GRANSAC, H. **Study of the suitability of aluminum alloys for additive manufacturing by laser powder bed fusion**. *Sci. Bull 79* (2017), 219–238.

**[76]** AVERSA, A., LORUSSO, M., TREVISAN, F., AMBROSIO, E. P., CALIGNANO, F., MANFREDI, D., BIAMINO, S., FINO, P., LOMBARDI, M., AND PAVESE, M. **Effect of process and post-process conditions on the mechanical properties of an a357 alloy produced via laser powder bed fusion**. *Metals 7*, 2 (2017), 68.

**[77]** POLMEAR, I. **Metallurgy of the light metals**. *Light Alloys, third ed., Edward Arnold, London* (1995).

**[78]** MONDOLFO, L. F. **Aluminum alloys: structure and properties**. Elsevier, 2013.

**[79]** AVERSA, A., MARCHESE, G., SABOORI, A., BASSINI, E., MANFREDI, D., BIAMINO, S., UGUES, D., FINO, P., AND LOMBARDI, M. **New aluminum alloys specifically designed for laser powder bed fusion: A review**. *Materials 12*, 7 (2019), 1007.

**[80]** RAO, H., GIET, S., YANG, K., WU, X., AND DAVIES, C. H. **The influence of processing parameters on aluminium alloy a357 manufactured by selective laser melting**. *Materials & Design 109* (2016), 334–346.

**[81]** TREVISAN, F., CALIGNANO, F., LORUSSO, M., PAKKANEN, J., AMBROSIO, E. P., LOMBARDI, M., PAVESE, M., MANFREDI, D., AND FINO, P. **Effects of heat treatments on a357 alloy produced by selective laser melting**. In *European Congress*

*and Exhibition on Powder Metallurgy. European PM Conference Proceedings* (2016), The European Powder Metallurgy Association, pp. 1–6.

**[82]** LIDE, D. R. **CRC handbook of chemistry and physics: a ready-reference book of chemical and physical data**. CRC press, 1995.

**[83]** OZBILEN, A., UNAL, A., AND SHEPPARD, T. **Influence of oxygen on morphology and oxide content of gas atomised aluminium powders**. *Physical Chemistry of Powder Metals–Production and Processing, The Minerals, Metals and Materials Society* (1989).

**[84]** ZHANG, J., SONG, B., WEI, Q., BOURELL, D., AND SHI, Y. **A review of selective laser melting of aluminum alloys: Processing, microstructure, property and developing trends**. *Journal of Materials Science & Technology 35*, 2 (2019), 270–284.

**[85]** MERCELIS, P., AND KRUTH, J.-P. **Residual stresses in selective laser sintering and selective laser melting**. *Rapid prototyping journal* (2006).

**[86]** MINIACI, M., MAZZOTTI, M., RADZIEŃSKI, M., KHERRAZ, N., KUDELA, P., OSTACHOWICZ, W., MORVAN, B., BOSIA, F., AND PUGNO, N. M. **Experimental observation of a large low-frequency band gap in a polymer waveguide**. *Frontiers in Materials 5* (2018), 8.

**[87]** COFFY, E., EUPHRASIE, S., ADDOUCHE, M., VAIRAC, P., AND KHELIF, A. **Evidence of a broadband gap in a phononic crystal strip**. *Ultrasonics 78* (2017), 51–56.

**[88]** MINIACI, M., MARZANI, A., TESTONI, N., AND DE MARCHI, L. **Complete band gaps in a polyvinyl chloride (pvc) phononic plate with cross-like holes: numerical design and experimental verification**. *Ultrasonics 56* (2015), 251–259.

**[89]** WU, T.-T., WU, L.-C., AND HUANG, Z.-G. **Frequency band-gap measurement of two-dimensional air/silicon phononic crystals using layered slanted finger interdigital transducers**. *Journal of Applied Physics 97*, 9 (2005), 094916.

**[90]** BENCHABANE, S., KHELIF, A., RAUCH, J.-Y., ROBERT, L., AND LAUDE, V. **Evidence for complete surface wave band gap in a piezoelectric phononic crystal**. *Physical Review E 73*, 6 (2006), 065601.

**[91]** HEMON, S., AKJOUJ, A., SOLTANI, A., PENNEC, Y., EL HASSOUANI, Y., TALBI, A., MORTET, V., AND DJAFARI-ROUHANI, B. **Hypersonic band gap in an aln-tin bilayer phononic crystal slab**. *Applied Physics Letters 104*, 6 (2014), 063101.

**[92]** OUDICH, M., SENESI, M., ASSOUAR, M. B., RUZENNE, M., SUN, J.-H., VINCENT, B., HOU, Z., AND WU, T.-T. **Experimental evidence of locally resonant sonic**

**band gap in two-dimensional phononic stubbed plates**. *Physical Review B 84*, 16 (2011), 165136.

**[93]** STASZEWSKI, W., LEE, B., MALLET, L., AND SCARPA, F. **Structural health monitoring using scanning laser vibrometry: I. lamb wave sensing**. *Smart Materials and Structures 13*, 2 (2004), 251.

**[94]** MICHAELS, T. E., MICHAELS, J. E., AND RUZZENE, M. **Frequency–wavenumber domain analysis of guided wavefields**. *Ultrasonics 51*, 4 (2011), 452–466.

**[95]** BILLON, K., OUISSE, M., SADOULET-REBOUL, E., COLLET, M., BUTAUD, P., CHEVALLIER, G., AND KHELIF, A. **Design and experimental validation of a temperature-driven adaptive phononic crystal slab**. *Smart Materials and Structures 28*, 3 (2019), 035007.

**[96]** KHALES, H., HASSEIN-BEY, A., AND KHELIF, A. **Evidence of ultrasonic band gap in aluminum phononic crystal beam**. *Journal of Vibration and Acoustics 135*, 4 (2013).

# List of Figures

# List of Tables

Document generated with LaTeX and:
the LaTeX style for PhD Thesis created by S. Galland — https://github.com/gallandarakhneorg/tex-templates
the tex-upmethodology package suite — http://www.arakhne.org/tex-upmethodology/

école doctorale **sciences pour l'ingénieur et microtechniques**

**Title:** Experimental observation of elastic wave demultiplexer in phononic slab waveguides

**Keywords:** phononic, waveguide, démultiplexage

**Abstract:**

In the field of phononic crystal demultiplexer, many similar works have been focusing on the various theoretical aspects and delimited by the narrow-pass band frequency. We proposed a demultiplexing system consists of three distinct linear waveguides fabricated via Direct Metal Laser Sintering (DMLS). We respectively, provide both theoretical and experimental analysis to study the behavior of wave propagation within the device by using finite element method (FEM), Laser Doppler vibrometer (SLDV) and Micro System Analyser (MSA). The results shows the device successfully demonstrated the multi filtering capabilities to channel the incident wave exclusively according to their respective waveguide thus suggesting the demultiplexing capabilities of the proposed design.

**Titre :** Observation expérimentale d'un démultiplexeur à ondes élastiques dans des guides phononiques

**Mots-clés :** phononique, guides d'ondes, démultiplexeur

**Résumé :**

Dans phononique démultiplexage, De nombreux travaux proposés dans la littérature se sont concentrés sur les différents aspects théoriques et délimités par la fréquence à bande passante étroite. L'objectif de ce travail de thèse est d'étudier aussi bien théoriquement qu'expérimentalement un système de démultiplexage d'ondes élastiques constitué de trois guides d'ondes linéaires distincts pour l'application de démultiplexage fréquentielle. La technologie de fabrication additive via la technologie de frittage laser direct en métal (DMLS), a été utilisée pour fabriquer un échantillon à l'aide de l'imprimante 3D. Expérimentalement, les spectres de coefficient de transmission et une mesure de topographie de surface ont été mesurés à l'aide de Micro System Analyzer (MSA) avec un vibromètre laser Doppler (SLDV). Le résultat montre des ondes incidentes acheminées dans un guide d'ondes qui appartient à un canal avec une atténuation d'onde claire démontrée avec succès dans les deux autres canaux ce qui suggère les capacités de démultiplexage de la conception proposée.

Université Bourgogne Franche-Comté
32, avenue de l'Observatoire
25000 Besançon, France